# AN NMR RELAXOMETRY STUDY OF SLOW MOLECULAR DYNAMIC PROCESSES IN LIQUID CRYSTALS

A Thesis Submitted to the University of Hyderabad for the award of the Degree of

Doctor of Philosophy

in Physics

by

RAJESWARI MULAKALAPALLI


School of Physics
University of Hyderabad
P.O. Central University
Hyderabad - 500 046
Andhra Pradesh, India.

June 2011

*To*

*My Parents and Family*

# DECLARATION

I, Rajeswari Mulakalapalli, hereby declare that this thesis entitled "**An NMR relaxometry study of slow molecular dynamic processes in liquid crystals**" submitted by me under the guidance and supervision of Prof. V. S. S. Sastry is a bonafide research work. I also declare that it has not been submitted previously in part or in full to this University or any other University or Institution for the award of any degree or diploma.

(Rajeswari M)
Reg. No. 05PHPH03.

Date:
Place: Hyderabad

# CERTIFICATE

This is to certify that the thesis entitled "**An NMR relaxometry study of slow molecular dynamic processes in liquid crystals**" submitted by **Rajeswari Mulakalapalli** bearing Reg. No. 05PHPH03 in fulfillment of the requirements for the award of Doctor of Philosophy in Physics is a bonafide work carried out by her under my supervision and guidance.

The thesis has not been submitted previously in part or in full to this or any other University or Institution for the award of any degree or diploma.

Prof. V. S. S. Sastry
Thesis Supervisor.

Dean,
School of Physics,
University of Hyderabad.

# Acknowledgements

First and foremost I would like to thank my Lord and Savior Jesus Christ for helping me to know him as my personal Savior and giving me an opportunity to do my Ph.D.

I am indebted to my supervisor Prof. V. S. S. Sastry for his guiding wisdom throughout my Ph.D. This thesis is an extension of his hard work and dedication to this field of physics. Without his help it would not have been possible for me to finish this work. Sir, I am very thankful for the teaching and suggestions you made regarding physics and about life.

I am thankful to Prof. K. Venu for his initial guidance and interest in my work. I am very grateful to Dr. Surajit Dhara for his help in carrying out the experiments and providing me the facilities in his laboratory.

I thank the Dean, School of Physics, for the facilities provided during the course of my work. I also express my thanks to former Deans and other faculty members and the non-teaching staff of the School of Physics.

I thank Prof. R. Dabrowski for kindly providing the samples and for a successful collaboration during my work.

My sincere thanks to my senior Dr. M. Trivikram Rao for his help in carrying out my experiments, in useful discussions on the theory of NMR, his patience in clearing my curious doubts and for providing a friendly environment in the laboratory. I thank Ramudu and Sudheendran for helping me with vacuum measurements.

My special thanks to Mr. Anjan Prasad for his suggestions at various stages of my work and for his help in putting this thesis in TEX format.

My hearty thanks go to my friend Ramakrishna for his help and encouragement during my studies from early times of my Bachelors degree to date. It is my great pleasure to express my thanks to our research group Prof. K. P. N. Murthy, Dr. Sai Preeti, Dr. Jayasri, Kamala Latha, Regina Jose, Arun Kumar, Sankaraiah, Sathyanarayana, Siva, Suman Kalyan, Ananthaih, Shwetha, Vijay, Annapoorna, Madhuri and Sridhar for their helpful discussions and cheerful moments during my stay in the campus.

I thank Saritha, Poorna and Deepika for their help during the proof reading of my thesis and Sathya and Ananth for helping me in drawing the figures in my thesis.

I would like to thank my friends Sudha Nirmala, Tarak kumar, Sowjanya, Saritha, Udita, Padma, Tejal, Jhansi, Dhana, Bindu, Phani Sri, Syamala, Vijay, Raji, Shiva, Rajeswari and Sridevi who always kept up cheerful atmosphere, and made my life much more enjoyable during my stay in the campus. I would also like to express my thanks to my prayer group members in the hostel and my Church members at Gopannapally. My hearty thanks go to Mr. and Mrs. Isaac for their encouragement in hard times.

I thank the University of Hyderabad and University Grants Commission (UGC)-CAS for providing me the financial support during my stay, and Department of Science and Technology (DST) for providing me the financial support to attend an international conference.

I am indebted to all my family members for their love and support throughout my life.

Rajeswari

# Preface

Molecular processes in complex fluids like liquid crystals differ qualitatively among the various intermediate thermodynamic phases, and reflect subtle changes in the molecular dynamic organization arising from differing characteristic length and time scales in the medium. Details of such competing scales are valuable in understanding the criteria for stability of different phases, and in appreciating the interplay of relevant physical variables in the system *via* control parameter dependent couplings. Thus, experiments extracting such information on these processes are important, and techniques employing differing microscopic probes have specific figures of merit, depending on their selective coupling to the medium. Magnetic relaxation experiments, employing nuclear as well as electron spin probes, have been very effective in this regard, owing to the monitoring of the molecular dynamics by the concerned microscopic probes under resonant conditions. In this context, the technique of measuring nuclear spin-lattice relaxation rates over a wide frequency range, typically from $10^3$ to $10^8$ Hz (referred to as NMR relaxometry in contemporary literature), in conjunction with their temperature dependence, is now recognized for its uniqueness in mapping directly the spectral densities of different molecular processes, with the time widow of the probe residing precisely in the region of interest to complex fluids like liquid crystals. The instrumentation to carry out such experiments itself is novel, - requiring fast magnetic field-switching during the experiment so as to convert an initial thermally equilibrated spin system into an appropriately prepared non-equilibrium spin system evolving in the presence of very low (chosen) magnetic fields. This technique is referred to as field cycling NMR (FCNMR) relaxometry. The resulting dispersion profiles of nuclear spin-lattice relaxation rates provide a challenging task of quantitatively inferring about the time-fluctuations of different spin-couplings connecting the spin sub-system to thermal bath, through suitable stochastic modeling of the underlying molecular processes. It is with this perspective that the work presented in this thesis was taken up.

The thesis reports on the experimental observations through this methodology, on two types of liquid crystal (LC) systems: $^1H$ and $^{19}F$ FCNMR measurements on singly fluorinated tolanes and $^1H$ measurements on two liquid crystal systems embedded in a nano-porous medium formed by aerosil matrix. The first study is aimed at comparing and contrasting the $^1H$ and $^{19}F$ spin-lattice relaxation rate dispersion profiles to infer on the quantitatively different dynamic environments that these nuclei seem to probe due to their fortuitously different relaxation mechanisms. The second study on confined systems is directed to observing subtle changes in the molecular processes near the porous surfaces, inducing slow components in the reorientational correlations. The thesis presents these results in several chapters.

This thesis comprises of seven Chapters, of which the first Chapter very briefly explains the various types of liquid crystal systems, their physical properties and the effect of confinement on their properties. The second Chapter provides details of nuclear magnetic relaxation theory and molecular dynamic models relevant to the bulk and confined liquid crystal systems. The third Chapter recounts briefly the principle of FCNMR relaxometry, pulse sequences specific to spin relaxation measurements in conjunction with simultaneous magnetic field switching to effect field cycling process, and technical details of the instruments used in the investigations. The fourth Chapter deals with spin-lattice relaxation rate measurements in two singly fluorinated liquid crystals employing two nuclei ($^1H$ and $^{19}F$) located on the same LC molecule, bringing out significant deviations in the spectral densities experienced by the two probes. The next two Chapters provide details of surface-induced slow dynamic processes in two LC systems, realized by embedding them in nano-porous medium. The last chapter summarizes the conclusions of the work reported in this thesis.

Experimental findings on two fluorinated tolanes are reported in the fourth Chapter. Here, we attempt to interpret qualitatively different spin-lattice relaxation dispersions of two very similar nuclei with close gyromag-

netic ratios ($\gamma_H \approx \gamma_F$, within 6 %) in the isotropic phase of two liquid crystals: 4′-butoxy-3′-fluoro-4-isothiocyantotolane (4OFTOL) and 4′-butoxy-3-fluoro-4-isothiocyantotolane (4OTOLFo). These LC systems have a large number protons ($^1H$) residing on the molecule and a lone member ($^{19}F$) attached to its aromatic core. The latter has limited access to the lattice *via* the usual dipolar interaction terms due to the dissimilar $\gamma$'s (unlike spins) in the high frequency region of the experiment (*i.e.*, the so-called weak-coupling limit), and hence its observed significant coupling to lattice modes as well as its discernible dispersion calls for a mechanism which depends on a specific interaction unique to this species, *viz.*, the relatively strong spin-rotation. This mechanism however samples time correlations of molecular angular momentum components rather than reorientations (which couple to the dipolar terms). Thus the chosen systems are in a fortuitous circumstance of sampling two types of correlations of the dynamic processes of the system, and the present work is concerned with the interpretation of the experimental data recognizing this distinction. The FCNMR experiment also allows an effective contact of the fluorine system with protons (despite their differing $\gamma$'s) at low enough frequencies. In this regime, called the strong-coupling limit, the hetero-nuclear coupling acquires an effective homo-nuclear component due to overlap of the resonance lines, and the spin-lattice relaxation of the fluorine is now aided by this coupling, proportional to the degree of overlap. Due to the inherent effective coupling among protons over the entire region (in the sense of wide NMR experiment) the onset of this additional mechanism is not detectable from proton data. The differing temperature dependences of the relaxation rates of the two nuclear systems clearly indicate the presence of two distinct slow underlying molecular processes, experienced by the same molecule but reported differently by the two participating probes. In that sense this is an interesting experiment which focuses on qualitatively different molecular mechanisms, owing to differing effective couplings to the thermal bath, of the participating nuclei. These observations thus essentially translate to mapping of spectral densities of the time correlation functions of distinct processes modulating different lattice-coupling mechanisms. Our analysis shows that the present FCNMR experiments provide evidence for

the presence of slowly relaxing local structures in a liquid crystal, alluded to earlier through detailed ESR measurements on spin probes dissolved in liquid crystals.

The fifth Chapter deals with the proton spin-lattice relaxation rate measurements in different mesophases of bulk 4′-otyloxy-4-cyanobiphenyl (8OCB) and 8OCB embedded in random porous network formed by the aerosil particles. We found a notable increase in the relaxation rates in the sub-MHz regime in all the mesophases. This observed significant increase is quantitatively explained in terms of an additional slow relaxation mechanism induced in LC system due to confinement, referred to as molecular reorientations mediated by translational displacements (RMTD). This is characterized by a power-law dispersion in the low frequency range between certain low and high frequency cutoff values. The analysis of the experimental data shows that the major increase in the relaxation rate in confined systems is due to this process. The low and high frequency cutoffs of the RMTD mechanism provide some insight into the kinetics of LC molecules reorienting at the surface. And, the exponent value of this mechanism indicates the relative importance of wavelength modes in different mesophases. The increased interaction strength of this mechanism in all the phases with increasing the concentration of aerosil particles shows that the fraction of molecules in the ordered layer has correspondingly increased.

We also carried out similar experiments to observe the effect of confinement on another nematic liquid crystal system, 4-propyl-4′-pentylazoxybenzene (PPA), having its dipole moment in the lateral direction. We prepared the confined samples of this liquid crystal under identical conditions as that of 8OCB, for purpose of comparison. The sixth Chapter reports on the effect of confinement on the molecular processes in PPA due to random network formed by the aerosil matrix at two concentrations in the isotropic and nematic phases. The relaxation rate shows an increase at low frequencies in both the phases upon such confinement. The primary mechanism for this en-

hancement also seems to be due to RMTD, even though there are qualitative differences. The cutoff frequencies and the power law behavior (arising from the RMTD mechanism) extracted from the data bring out the details of slow processes introduced in confined samples, apart from the slight modifications of other known processes at molecular level (like reorientations). The effect of similar confinement on the dynamic organization in the two liquid crystals (8OCB and PPA) are compared, with specific interest in the slow molecular dynamics accounted by the FCNMR technique.

The NMR relaxometry technique used in our investigations, especially at very low frequencies, provides a unique opportunity to sample directly the ultra slow processes that occur in liquid crystal systems. The two types of examples taken for our study provide differing underlying slow process. In the first case (of tolanes) we exploited the sensitivity of the fluorine nuclei to effectively relax *via* spin-rotation interaction thereby inferring directly on time correlations of molecular angular momentum components. We find that these processes are relatively very slow, pointing to the presence of slowly relaxing local torques as experienced by the resonant probe. The fact that the protons residing on the same molecule are relaxed *via* molecular reorientations, and hence are essentially insensitive to the slow torques in the system, provides an interesting contrast, evidencing the power of this technique. In confined samples (second case), it is due to the onset of slow dynamics induced by the surface interactions of the liquid crystal molecules, and made prominent by the effect of severe confinement, that the proton probe itself is able to monitor and report on these subtle long time correlations in the reorientational dynamics of the molecules, *via* FCNMR measurements. We present our conclusions of this work in the last Chapter.

# Contents

# List of Figures

# List of Tables

# 1

# Introduction to Liquid Crystal Physics

## 1.1 Introduction

Liquid crystals are a class of materials that form intermediate anisotropic phases between a solid and an isotropic liquid. A liquid crystal may flow like a liquid, but have the molecules in the liquid arranged and/or oriented in a crystal-like way. The essential characteristic is the presence of orientational order of the non-spherical molecules, while in addition positional order of the centers of mass is either absent or reduced. The constituent molecules have an anisotropic shape being rod-like, disc-like or even banana-shaped. The orientational order of the molecules in a liquid crystal medium is characterized by specifying its director, which is a headless unit vector pointing to the average direction of alignment of the anisotropic molecules (say, rod like). The intermediate phases of the liquid crystals exhibit several curious anisotropic physical properties such as refractive indices, dielectric constants, diamagnetic susceptibility and flow properties like viscosity etc. Many lucid accounts of these are available [1–8].

Study of molecular processes is very important in understanding the dynamics of the system. Many experimental techniques have been used to study the dynamics of liquid crystals depending on the time scale of their occurrence and dynamics of interest [7]. Magnetic resonance and relaxometric studies

have been shown to be powerful for studying both the structure and dynamics of liquid crystals [9–14]. In magnetic resonance methods the dynamics can be probed by nuclei or electron spin probes and due to the resonant nature of the probe, one can focus the experiment at a chosen time window. In NMR relaxometric studies, the relaxation rates measured over a broad frequency as a function of temperature cover the dynamic range from fast motions to ultra slow processes which occur in the mesophases or in confined liquid crystal systems. In general, the complex dynamics of liquid crystals is a combination of both collective and non-collective motions which fall in the time scales of $10^{-1}$ - $10^{-11}$ sec. With the recent development of a convenient method, termed as Field Cycling relaxometry, it is possible to probe dynamics in these time scales. The present work is concerned with the measurement of nuclear spin-lattice relaxation rates over such a typical frequency range at different temperatures in bulk and confined liquid crystals. With this objective this chapter gives an introduction to types of liquid crystals, a brief review of their physical properties, a short account on phase transitions in liquid crystals, and a discussion on effects of confinement. Relevant concepts are further developed and discussed in detail in latter chapters.

## 1.2 Classification of liquid crystals

In general liquid crystals can be classified as two types: (1) Thermotropic and (2) Lyotropic. In thermotropic liquid crystals the transitions between different phases are driven by temperature. Depending on the shape anisotropy of molecules thermotropic liquid crystals are further classified into: 1. Calamitic liquid crystals made up of rod-like molecules; 2. Discotic liquid crystals made of disc-like molecules; 3. Banana liquid crystals made of bent-core molecules. Lyotropic liquid crystals are made up of two or more components. They are formed in mixtures of amphiphilic molecules and a polar solvent like water. Amphiphiles tend to aggregate so that the polar groups occupy the interface towards solvent. Small aggregates with dimensions comparable to the molecular length are often spherical in shape and

exist in micellar solutions. The formation of infinitely extended aggregates or lamellas is characteristic for the most common lyotropic liquid crystalline phases.

The work reported in this thesis deals with thermotropic liquid crystals comprising of molecules with their shapes approximated to rod-like structures. The details of these liquid crystal systems are given below.

## 1.3 Classification of thermotropic liquid crytals

Thermotropic liquid crystals made of rod-like molecules are typically classified into three types, based on the symmetry of the medium: Nematics, Cholestrics, and Smectics.

### 1.3.1 Nematics

The simplest among all the mesophases of a liquid crystal is the nematic phase. Here the molecules have a long range orientational order but no translational order. Usually, nematic liquid crystals made of rod-like molecules exhibit uniaxial cylindrical symmetry. On an average the long axes of the molecules are oriented along a particular direction called the director denoted by $\hat{n}$ as shown in Figure 1.1. The director $\hat{n}$ is a dimensionless apolar unit vector *i.e.*, $\hat{n}$ and - $\hat{n}$ are physically equivalent [1]. Even when the molecules are made of highly polar end groups the medium is still apolar as the molecules orient such that there is no net polarization in the medium. The orientational order in the nematic phase is given by an order parameter $S$ as

$$S = \langle P_2(cos\theta)\rangle = \frac{1}{2}\langle 3cos^2\theta - 1\rangle. \tag{1.1}$$

Here $\theta$ is the angle between the long axis of each molecule makes with the director, and the angular brackets indicate ensemble average in thermal

equilibrium.

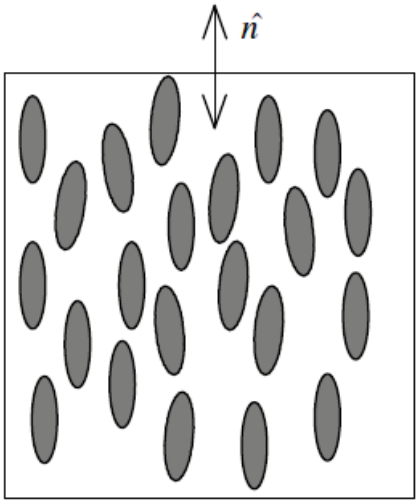


Figure 1.1: Schematic representation of molecular arrangement in a nematic liquid crystal, where $\hat{n}$ represents the director.

### 1.3.2 Cholestrics

The cholestric phase is a kind of nematic type liquid crystal, normally found when its molecules are optically active. The director $\hat{n}$ is no longer uniformly oriented in space, but precesses in a helical fashion along the $z$-axis as shown in Figure 1.2. As $\hat{n}$ is physically equivalent to - $\hat{n}$, the periodicity of medium along helix axis is $P/2$, where $P$ represents the pitch of the medium.

### 1.3.3 Smectics

In the smectic phase, the orientational order is supplemented with an additional long-range positional order along chosen direction, leading to the formation of layered structures. The molecular centers of mass are, on the average, arranged in equi-distant planes. Additional symmetry properties are

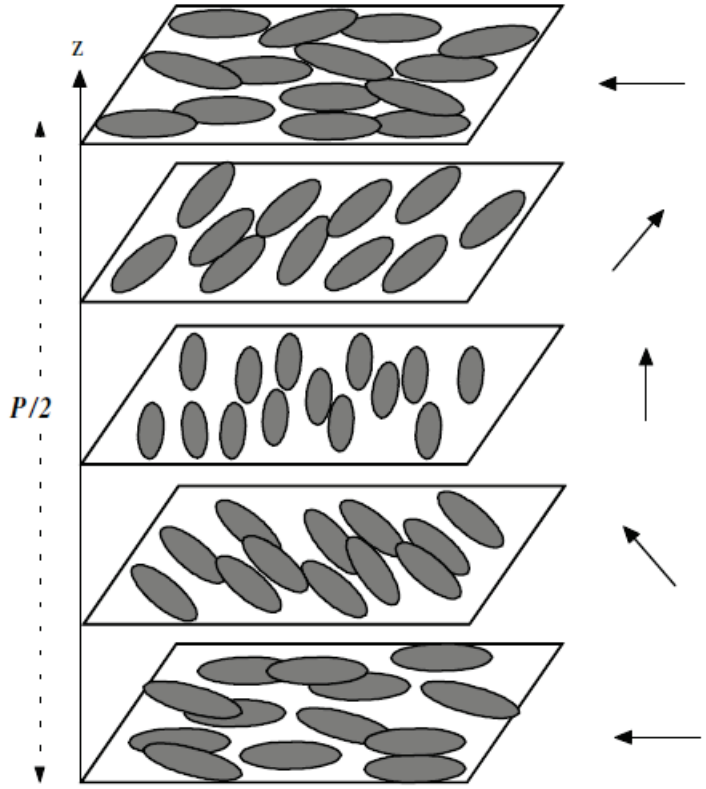


Figure 1.2: Schematic representation of molecular arrangement in the cholesteric phase. The arrows indicate the orientation of director $\hat{n}$.

used to distinguish different types of the smectic phase, labeled by the subscripts A to I. In $S_A$ phase the molecules are arranged in layered structures, with the layer thickness typically close to the molecular length or double that length. Inside each layer, the centers of gravity show no long-range order and each layer is thus a two-dimensional liquid. In $S_B$ phase the molecular centers in each layer are hexagonal close packed. In $S_C$ phase the long axes of the molecules in the layer are tilted with respect to the layer normal and this phase is optically biaxial. The schematic diagram of the more common $S_A$ and $S_C$ phases is shown in Figure 1.3.

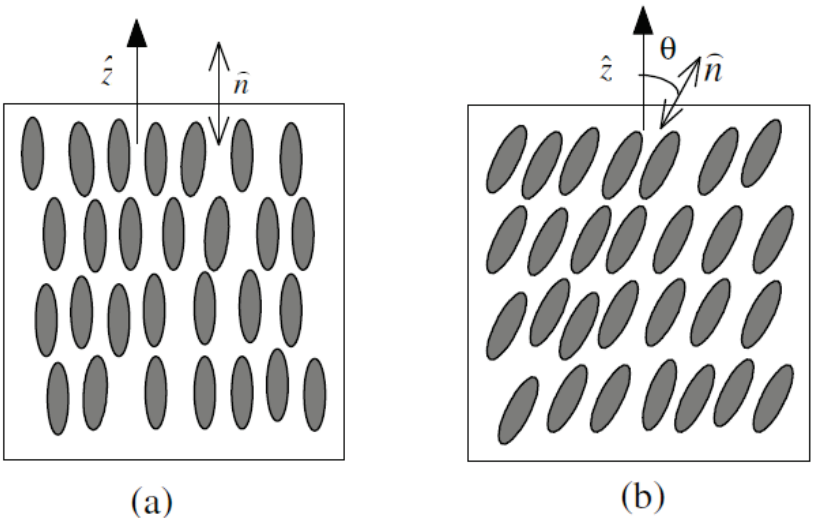


Figure 1.3: Schematic representation of molecular arrangement in (a) $S_A$ and (b) $S_C$ phases.

A brief review of the effect of molecular anisotropy on different physical properties is presented below.

## 1.4 Anisotropic physical properties

The orientational order present in liquid crystalline materials gives rise to an anisotropy in various physical properties. Examples are magnetic susceptibility, refractive index, dielectric constants etc. The anisotropy in the physical properties is essential for a number of applications in liquid crystals [15]. The physical behavior of liquid crystals can be distinguished into scalar and non-scalar properties. Typical scalar properties are the orientational order parameter $S$ and parameters associated with the thermodynamic transition behavior (transition temperatures and transition enthalpies). Important non-scalar properties are the dielectric, diamagnetic, optical, elastic and viscous coefficients. Here we present a very brief account of certain physical properties relevant to our studies.

### 1.4.1 Order parameter

The order parameter gives a measure of the distribution of the rod-like molecules about the director. In view of the apolar nature of the director $\hat{n}$ the orientational order parameter characterizing the nematic phase cannot be a vector. Thus, the relevant order parameter is a second rank traceless symmetric tensor and is given by

$$Q_{ij} = S\left(n_i n_j - \frac{\delta_{ij}}{3}\right), \quad where \quad i,\, j = X, Y, Z. \tag{1.2}$$

Here $S$ is the magnitude of the orientational order parameter, given by equation 1.1.

The order parameter is directly related to certain experimentally measurable quantities for example, the diamagnetic susceptibility, dielectric constant and refractive indices etc. Nuclear magnetic resonance (NMR) is one of the elegant methodologies to provide information about the orientational order, and it can be achieved in different ways. The orientational order can be inferred by considering (1) the coupling between nuclear dipole moments, (2) the coupling between a nuclear dipole and a nuclear quadrupole moment, and (3) the chemical shift. Taking the first method, say for illustration, the characteristic NMR spectrum of nuclei like protons residing on the molecules comprising a perfectly isotropic fluid would consist of narrow lines where both inter- and intra-molecular dipole-dipole interactions completely averaged to zero. This is due to rapid translational diffusion as well as to the fast isotropic rotational tumbling of the molecules. In the nematic phase the intermolecular dipolar interactions average to zero and the spectra still consist of narrow lines. However additional line splitting occurs in this liquid crystalline phase due to the presence of orientational order, breaking of rotational symmetry and residual intra-molecular dipolar interactions persist when compared with the isotropic phase. Consequently, NMR spectrum of the protons in the nematic phase splits for example into a doublet, the spa-

cing being a measure of the order parameter to be estimated. One can see that the spacing $\Delta\nu$ is related to $S$ [3] as:

$$\Delta\nu = CS$$

Here $C$ is a constant dependent on the gyromagnetic ratio of the nuclei and their mutual distance. The splitting is temperature dependent, reflecting the onset and growth of orientational order of the medium as the system is cooled from isotropic to, say, a nematic phase. Any sudden jumps in $S$ during a cooling process, arising from the nature of the phase transition involved, are duly reflected in the details of the NMR spectrum.

### 1.4.2 Magnetic susceptibility

Like most organic substances liquid crystals are usually diamagnetic. The diamagnetism exhibited by these systems is the result of additive contributions of the magnetic properties of the single molecular components. The diamagnetic properties of uniaxial mesophases can be described by the two susceptibilities $\chi_{\parallel}$ and $\chi_{\perp}$, which are the resulting susceptibilities when the magnetic field is applied parallel and perpendicular to the director, respectively. The magnitude of anisotropy in the diamagnetic susceptibility is defined as

$$\Delta\chi = \chi_{\parallel} - \chi_{\perp}.$$

The diamagnetic anisotropy of all liquid crystals having an aromatic ring system has been found to be positive and of the order of magnitude $10^{-7}$ (SI units). The magnitude is found to decrease with every benzene ring which is substituted by a cyclohexane or cyclohexane derivative ring. A negative anisotropy is observed in purely cycloaliphatic liquid crystals. The diamagnetic anisotropy can be used as an order parameter to describe the degree of orientational order of a mesophase.

### 1.4.3 Viscosity

The viscosity of any material is a collective property resulting from the interaction of the molecules with one another. The nematic liquid crystal flow like an ordinary Newtonian liquid but the viscosity is not isotropic because of the presence of orientational order in the mesophases. For a complete description of viscosity of a nematic liquid crystal, five viscosity coefficients are needed [16]. Among these five, three of them are shear viscosities and the other two take director rotation or coupling between the director and the flow pattern into account. The three shear viscosity coefficients are referred to as Miesowicz coefficients [17]. These three coefficients are measured experimentally by placing the liquid crystal between two flat plates and measuring the force necessary to move one plate past the other at a certain velocity. Three different situations can be realized depending on the orientation of the director between the plates and flow direction.

$\eta_1$: the director is perpendicular to the flow pattern and parallel to the velocity gradient (Fig. 1.4a).

$\eta_2$: the director is parallel to the flow pattern and perpendicular to the velocity gradient (Fig. 1.4b).

$\eta_3$: the director is perpendicular to the flow pattern and perpendicular to the velocity gradient (Fig. 1.4c).

In addition to the coefficients $\eta_1$ and $\eta_2$ which are antisymmetric with regard to the flow direction and the velocity gradient, a symmetric viscosity coefficient $\eta_{12}$ is also possible. This refers to the case when director is suspended at an angle of $45^0$ with both the flow pattern and the velocity gradient.

Additional viscosity coefficient $\gamma_1$ known as rotational viscosity comes

into play when a rotation of the molecule around an axis perpendicular to the director takes place. This coefficient is very important when the reorientation of the director in an electric or magnetic field is discussed, for example in determining the on and off times of display devices. In liquid crystal display (LCD) the switching time $\tau$ is approximately proportional to $\gamma_1 d^2$ with $d$ representing the cell spacing. The value of $\gamma_1$ for technically important nematic materials is found to be in the range 0.02 poise to about 0.5 poise.

For most practical purposes an appropriate average value of $\eta$ is adequate. As a rule, the longer and stiffer the molecule the greater is the average value of $\eta$. It has a high value for esters and a relatively low value for the biphenyls and an even lower value for the phenyl cyclohexanes [19] and cyclohexyl or cyclohexanes [20]. The value decreases rapidly with increase in temperature.

### 1.4.4 Elasticity

In a non-uniformly oriented nematic the orientation of director varies continuously in space. There are three fundamental types of distortions in a nematic liquid crystal and any deformation can be written as a combination of these three. They are: Splay, Twist, and Bend.

The free energy density associated with a distorted nematic, referring the uniformly aligned sample as the ground state, may be approximated as a quadratic function of curvature strains in which the analogues of elastic moduli appear as elastic coefficients. The deformation free energy density is expressed as [1]

$$F = \frac{1}{2}\left[K_1(\nabla.\,\hat{n})^2 + K_2(\hat{n}.\,\nabla\times\hat{n})^2 + K_3(\hat{n}\times\nabla\times\hat{n})^2\right].$$

where $K_1$, $K_2$, and $K_3$ are the splay, twist and bend elastic constants respectively (also called as Franks elastic constants [21]) and the schematic representation of these deformations are shown in Figure 1.5. For normal

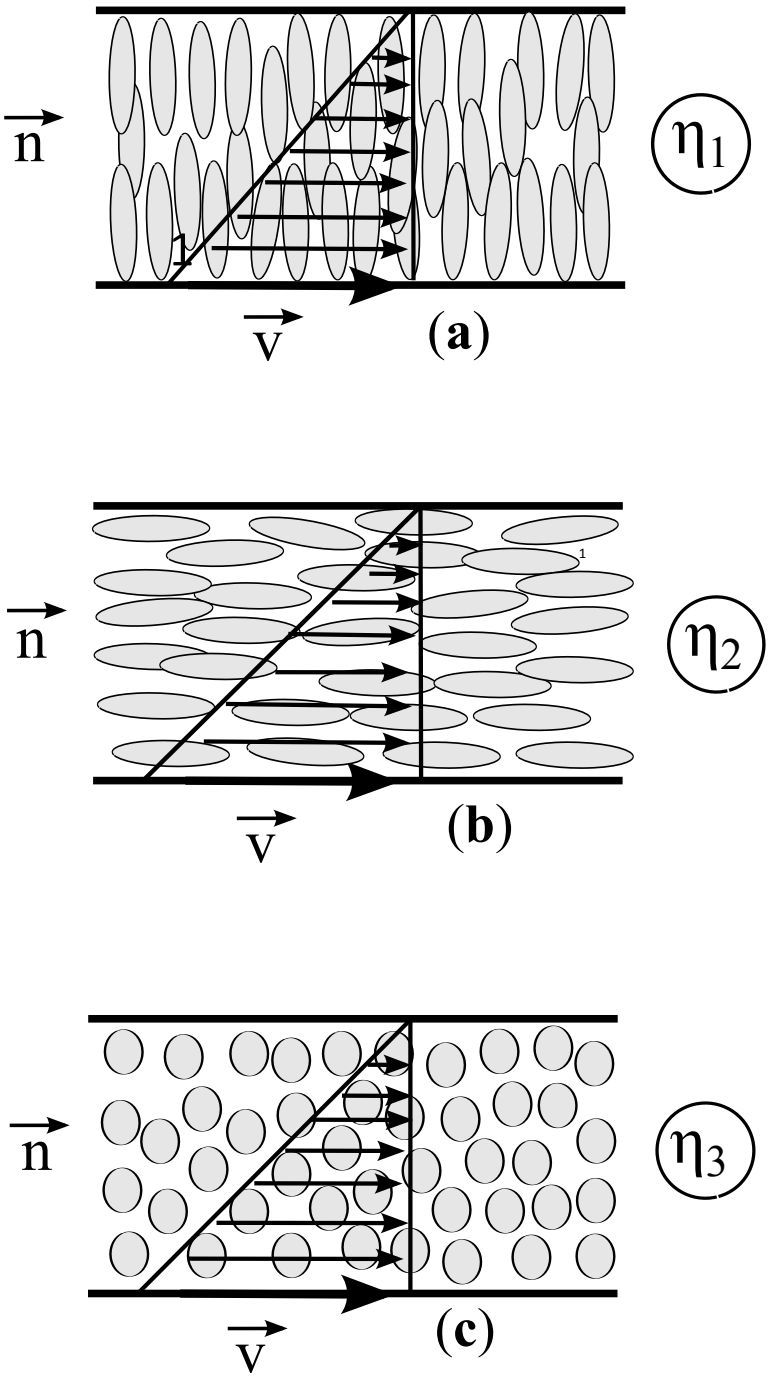


Figure 1.4: The three Miesowicz viscosity coefficients [18].

nematics, the value is around $10^{-7}$ dynes and $K_3 > K_1 > K_2$. The elastic constants are strongly temperature dependent and these deformation energies are considerably smaller than the average thermal energy. For this reason relatively small external forces (boundary forces, electric or magnetic fields, material flow, temperature gradients) can deform nematic liquid crystals. In the neighborhood of the phase transition $N \rightarrow S_A$, because of a pre-transitional smectic order, a strong divergence of $K_3$ and $K_2$ is observed [22], whereas $K_1$ changes continuously. The elastic free energy in the Smectic A phase is expressed as

$$F = \frac{1}{2}\left[K_1(\nabla .\, \hat{n})^2 + \frac{1}{2}B\left(\frac{\partial u}{\partial z}\right)^2\right]$$

where $B$ is the bulk or compressional elastic constant. In the vicinity of the transition $N \rightarrow S_C$ all elastic constants diverge. Also, the length of the alkyl chain influences the elastic properties of the nematic phase [15].

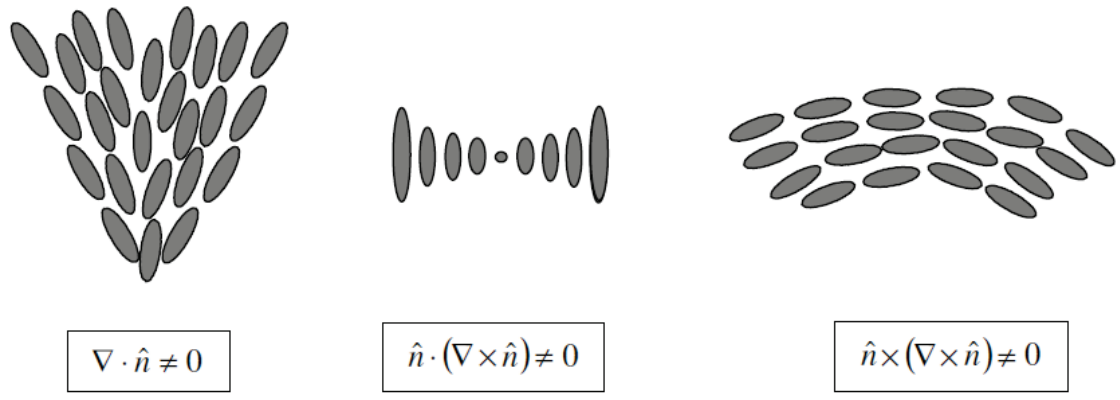


Figure 1.5: The three basic elastic deformations of the director in a nematic liquid crystal.

## 1.5 Phase transitions

The two extreme forms of condensed matter are liquids where the average structure is invariant under arbitrary rotations and translations, and crystalline solids with average structures that are invariant only with respect to certain discrete lattice translations and point group operations comprising the space group. The liquid state has short-range order but no long-range order and has the highest possible symmetry. The crystalline solid state has long-range positional and rotational order and has much lower symmetry than the liquid state. Between these two extremes there are systems that exhibit short-range correlations in some directions and long-range order in others, and have thus symmetries intermediate between those of liquids and solids. One set of such intermediate ordered materials are referred to as liquid crystals (the other set being plastic crystals), and these systems show a rich variety of continuous or weakly first-order phase transitions. More interestingly, these materials exhibit a very rich and exciting phenomena like ordering with various symmetries, anisotropic scaling behaviors, coupled order-parameters (mode coupling), multicritical points, wide critical domains, defect mediated transitions, manifestation of low dimensionality, and multiply re-entrant topologies, to name a few. Thus, besides their well-known technical applications in optics and electronic displays, liquid crystals, from the point of view of basic science, provide a very convenient realizable physical system to understand and manipulate these interesting facets [5].

Phase transitions are characterized by abrupt changes, discontinuities, and strong fluctuations in physical properties coupled to the transition. In liquid crystals, transition between different phases corresponds to the breaking of certain symmetry of the medium. On physical grounds the phase transition involves a transformation from an ordered (lower symmetry) phase to a relatively disordered (higher symmetry) phase (or vice versa) as the transition temperature is crossed. The basic reason for the excitement and continued interest in liquid crystal phase transitions is that with the discovery of every

new physical system with its characteristic phase behavior, present understanding of the phenomena of phase transition is revisited, thus enriching its appreciation. Since the mesophases transitions are either weakly discontinuous or continuous, they are expected to display behavior associated with critical points, including strong fluctuations and diverging susceptibility.

One of the most significant messages from the fascinating theoretical treatments in this context is that in the vicinity of such a transition the microscopic details of the system become increasingly unimportant in describing the details of the transition. Instead, the range of interactions, the physical dimension of the system, and symmetry of the order parameter determine the behavior of the system when it is very close to the transition. These transitions among different mesophases involve broken continuous symmetries in real space, while their interactions on a molecular scale are still short range. In general terms, fluctuations have thus long been recognized to be crucial in mediating such phase transitions. Relatively little is known about fluctuation phenomena (critical phenomena) at a first-order transition, such as isotropic-nematic transitions, as compared to fluctuation-controlled second-order phase transitions. The critical phenomena in liquid crystals is further enriched due to a wide variety of symmetries of the different phases, and in particular because of couplings of the different order parameters. These features may look to be complicating theoretical considerations and restrict the application of existing established analytical tools, but they have the potential to initiate fresh debate on possible advances in this direction. Another salient feature of mesogenic materials is that they have generic long-range correlation even far from critical points, or hydrodynamic instabilities [23, 24], that they could make it difficult to access critical regimes before being finessed by a first-order phase transition [25].

The phase transition in liquid crystals from one phase to another phase is not necessarily sharp but its discernible effects stretch over a certain range. The isotropic-nematic liquid transitions tend to be smaller than about 0.6 -

0.8K, whereas crystalline, smectic or smectic-isotropic liquid transitions are generally much wider. All I-N transitions are observed to be (weak) first order, and due to the involvement of the small latent heat and volume changes across the transition, it shows a nearly second order nature, permitting a description in terms of suitably modified Landau theory [26]. Unlike pure first order transitions, liquid crystals at I-N transition show significant pretransitional effects near the transition temperature. In this range, short range nematic order is encountered in the isotropic liquid and quasi cirtical order parameter fluctuations exist in the nematic liquid crystalline phase. The orientational order parameter changes discontinuously at $T_{NI}$ from zero to a finite value. Above $T_{NI}$, the orientations of the molecules are correlated spatially over finite distances and this can be measured as the coherence length $\xi$. If the nematic order is long lived in comparison to the NMR time scales ($1/\omega_0$), then spin-lattice relaxation measurements (which, as we will note in the next chapter, probe different molecular dynamic processes in the medium) can sense the onset of cooperative director fluctuations. Just below $T_{NI}$, large fluctuations in the magnitude of the order parameter can also contribute to the effective coupling of the spin subsystem to the thermal bath. These have been very lucid expositions of the specific effects on nuclear magnetic resonance and relaxation due to the characteristic features of liquid crystals [9, 10], and the present dissertation draws generally various useful concepts and formulations from these sources.

Among the different attempts to explain phase transitions in these systems, one of the simplest and widely applied approaches is the phenomenological theory of Landau and de Gennes [1, 26–31] in which the Helmholtz free energy is expressed in powers of order parameters and its gradients. This theory captures characteristic features of the phase transition surprisingly well, though it lacks the quantitative predicting power about the phase diagram. The other theoretical approach is concerned with mean field theories developed by several authors [25]. The first such treatment is due to Onsager [32], where the origin of nematic ordering is ascribed to the anisotropic shape

of molecules, invoking repulsive interactions. The Maier-Saupe (MS) theory [33, 34] and its modifications, as well as extensions [1–3, 35–38], attribute the formation of the ordered phase to the anisotropic attractive interactions. In reality, of course, both of these mechanisms exist and are operative. Thus, in the van der Waals type theories both anisotropic hard-core repulsions and angle dependent attractions are explicitly included [39–41]. Another interesting type of molecular theory is developed by Singh [42] and others [[25] and references there in]. These are based on the density functional approach which facilitates writing exact expressions for thermodynamic functions and one-particle distribution functions in terms of direct correlation functions. The major difficulty with such treatments is associated with the evaluation of direct correlation functions which obviously requires a precise knowledge of the inter-molecular interactions. At this time, only approximate methods are known for this purpose.

At the N-$S_A$ transition the continuous translational symmetry of the nematic phases is spontaneously broken by the appearance of one-dimensional density wave in the $S_A$ phase. Close to the transition the onset of quasi-smectic features in the nematic phase may lead to a dramatic change in certain properties such as elastic coefficients, transport properties, cholesteric pitch, etc. Original theories due to McMillan [43] and de Gennes [44] suggested that the N-$S_A$ transition could be first or second order depending on the degree of coupling between the two relevant order parameters, and the order of the transition could change depending on the specific choice of sample and experimental conditions. The salient features of the N-$S_A$ transition are documented well by several authors [45, 46].

## 1.6 Effect of confinement

Liquid crystalline materials confined to different geometries attracted considerable attention due to their novel electro-optic properties and their rich

physical phenomena. Independent of the methods used to constrain the liquid crystals, these systems have one underlying common theme: a symmetry-breaking, non-planar confinement imposed by the surrounding matrix. In addition, confined liquid crystals differ from macroscopic bulk systems because of their large surface-to-volume ratio. Their composite nature profoundly affects the ordering of the liquid crystal molecules and their susceptibility to external fields, making them ideal for many uses, including electro-optic applications [47].

The confinement affects the transition temperatures and the physical properties of liquid crystalline materials. The random network induces order at the surface. The orientational order induced by the surface is large in the first layer of liquid crystal molecules next to the surface and it decays exponentially with decreasing distance from the surface [48]. The decay constant can be measured as a nematic correlation length as introduced by de Gennes [26]. In the case of strong confinement the transitions become continuous or sometimes they are smeared out. Different experimental techniques are used to study the effect under different confining environments, such as Anopores [49], Millipores [50, 51], Nucleopore [52], Aerogel [53], Controlled Pore Glass (CPG) [54–56], Aerosil [57–59] etc. Of all these porous matrices, aerosil particles are particularly interesting because the random disorder can be introduced into the system in a controlled manner. This thesis also includes a study on the effect of one such confining matrix on the dynamical properties in different phases of liquid crystal systems.

## References

[1] P. G. de Gennes and J. Prost, *Physics of Liquid Crystals*, second edition (1993).

[2] S. Chandrasekhar, *Liquid Crystals*, Cambridge University Press, second edition (1992).

[3] G. Vertogen and W. H. deJeu, *Thermotropic Liquid Crystals: Fundamentals*, Springer-Verlag (1988).

[4] P. J. Collings and M. Hird, *Introduction to Liquid Crystals Chemistry and Physics*, Taylor and Francis, London (1977).

[5] D. Demus, J. Goodby, G. W. Gray, H. W. Spiess, V. Vill, *Handbook of Liquid Crystals*, Wiley-VCH, Germany (1998).

[6] S. Martellucci and A. N. Chester, *Phase transitions in liquid crystals*, NATO ASI series, New York (1992).

[7] G. R. Luckhurst and C. A. Veracini, *The Molecular Dynamics in Liquid Crystals*, Kluver Academic Publishers, London (1994).

[8] Sri Singh, *Liquid crystals: Fundamentals*, World Scientific, Singapore (2002).

[9] R. Y. Dong, *Nuclear Magnetic Resonance of Liquid Crystals*, Springer - Verlag, New York (1997).

[10] R. Y. Dong, *Nuclear Magnetic Resonance spectroscopy of Liquid Crystals*, World Scientific, Singapore (2009).

[11] R. Y. Dong, Prog. Nucl. Magn. Reson. Spectrosc. **41**, 115 (2002).

[12] R. Y. Dong, Ann. Rep. on NMR Spectrosc. **53**, 68 (2004).

[13] R. Kimmich, E. Anoardo, Prog. Nucl. Magn. Reson. Spectrosc. **44**, 257 (2004).

[14] V. Domenici, M. Geppi, C. A. Veracini, Prog. Nucl. Magn. Reson. Spectrosc. **50**, 1 (2006).

[15] D. Coates, *Liquid crystals: applications and uses*, Vol.1. Ed. By Birendra Bahadur World Scientific publications (1990).

[16] F. M. Leslie, Arch. Ration. Mech. Anal. **28**, 265 (1968).

[17] M. Miesowicz, Nature **158**, 261 (1946).

[18] J. Jdazyn and G. Czechowski, J. Phys.: Condens. Matter **13**, 261 (2001).

[19] L. Pohl, R. Eidenschink, G. Krause, and D. Erdmann, Phys. Lett. A. **60**, 421 (1977).

[20] L. Pohl, R. Eidenschink, G. Krause, and D. Erdmann, Phys. Lett. A. **65**, 169 (1978).

[21] F. C. Frank, Disc. Faraday Soc. **59**, 958 (1958).

[22] L. Cheung, R. B. Mayer and H. Gruler Phys. Rev. Lett. **31**, 349 (1973).

[23] J. R. Dorfman, T. R. Kirkpatrick, J. V. Sengers, Ann. Phys. Chem. **45**, 213 (1994).

[24] G. R. Luckhurst, G. W. Gray (Eds.), *The Molecular Physics of Liquid Crystals*, Academic Press, New York (1979).

[25] S. Singh, Physics Reports **324**, 107 (2000).

[26] P. G. de Gennes, *The physics of liquid crystals, Clarendon*, Oxford (1974).

[27] L. D. Landau, Phys. Z Sowjefunion **11**, 26 (1937).

[28] L. D. Landau, and E. M. Lifshitz, *Statistical Physics*, Vol. 1, 3rd edition, Pergamon, Oxford (1980).

[29] P. G. de Gennes, Mol. Cryst. Liq. Cryst. **12**, 193 (1971).

[30] P. G. de Gennes, Solid State Comm. **10**, 753 (1972).

[31] T. E. Faber, Proc. Roy Soc. London Ser. A **375**, 579 (1982).

[32] L. Onsager, Ann. N.Y. Acad. Sci. **51**, 627 (1949).

[33] W. Maier, A. Saupe, Z. Naturforsch. **14a**, 882 (1959).

[34] W. Maier, A. Saupe, Z. Naturforsch. **15a**, 287 (1960).

[35] K. K. Kobayashi, F. Schneider, Mol. Cryst. Liq. Cryst. **13**, 137 (1971).

[36] R. B. Meyer, T. G. Lubensky, Phys. Rev. A **14**, 2307 (1976).

[37] (a) G. R. Luckhurst, *Molecular field theories of nematics*, in: G. R. Luckhurst, G. W. Gray (Eds.), *The Molecular Physics of Liquid Crystals*, Acad. Press, New York, p. 85, 1979 ; (b) G. R. Luckhurst, C. Zannoni, Nature **267**, 412 (1977).

[38] N. V.Madhusudana, *Theories of liquid crystals*, in: B. Bahadur (Ed.), *Liquid Crystals: Applications and Uses*, Vol. 1, World Scientific, Singapore, p. 37, 1990 (Chapter 2).

[39] (a) M. A. Cotter, *The Van der Waals approach to nematic liquid crystals*, in: G. R. Luckhurst, G. W. Gray (Eds.), *The Molecular Physics of Liquid Crystals*, Acad. Press, New York, p. 181, 1979 (Chapter 8); (b) M. A. Cotter, J. Chem. Phys. **66**, 1098 (1977).

[40] (a) S. Singh, K. Singh, Mol. Cryst. Liq. Cryst. **101**, 77 (1983); (b) K. Singh, S. Singh, Mol. Cryst. Liq. Cryst. **108**, 133 (1984); (c) S. Singh, T. K. Lahiri, K. Singh, Mol. Cryst. Liq. Cryst. **225**, 361 (1993).

[41] (a) P. J. Flory, R. Ronca, Mol. Cryst. Liq. Cryst. **54**, 311 (1979); (b) F. Dowell, Phys. Rev. A **28**, 1003 (1983); (c) F. Dowell, Phys. Rev. A **31**, 2464, 3214 (1985).

[42] Y. Singh, Phys. Rep. **207**, 351 (1991).

[43] W. L. McMillan, Phys. Rev. **4A**, 1238(1971). Phys. Rev. **23B**, 363(1971).

[44] P. G. de Gennes, Phys. Lett. **30A**, 454 (1969).

[45] M. A. Anisimov, *Critical Phenomena in Liquids and Liquid Crystals*, Gordon and Breach, New York (1991).

[46] W. H. De Jeu, NATO School on Phase Transitions in Liquid Crystals, Erice, Italy, May 1991.

[47] G. P. Crawford and S. Zumer, *Liquid crystals in complex geometries*, Taylor and Francis, London, (1996).

[48] P. Sheng, Phys. Rev. A **26**, 1610 (1982).

[49] G. S. Iannacchione and D.Finotello, Phys. Rev. Lett. **69**, 2094 (1992).

[50] SihaiQian, Germano S. Iannacchione, and Daniele Finotello, Phys. Rev. E **57**, 4305 (1998).

[51] D. Finotello, H. Zeng, B. Zalar, G. S. Iannacchione, Mol. Cryst. Liq. Cryst. **358**, 237 (2001).

[52] D. W. Allender, G. P. Crawford, and J. W. Doane, Phys. Rev. Lett **67**, 1442 (1991).

[53] Noel A. Clark, Tommaso Bellini, Rainer M. Malzbender, Britt N. Thomas, Aqron G.Rappaport, Chris D. Muzny, Dale W. Schaefer, and Larry Hrubesh, Phys. Rev. Lett. **71**, 3505 (1993).

[54] S. Kralj, A. Zidansek, G. Lahajnar, I. Musevic, S. Zumer, R. Blinc, and M. M. Pintar, Phys. Rev. E **53**, 3629 (1996).

[55] M. D. Dadmun and M. Muthukumar, J. Chem. Phys. **98**, 4850 (1993).

[56] M. Vilfan, T. Apih, P. J. Sebastiao, G. Lahajnar, and S. Zumer, Phys. Rev. E **76**, 051708 (2007).

[57] G. S. Iannacchione, C. W. Garland, J. T. Mang, T. P. Rieker, Phys. Rev. E **58**, 5966 (1998).

[58] A. Roshi, G. S. Iannacchione, P. S. Clegg, R. J. Birgeneau, Phys. Rev. E **69**, 031703 (2004).

[59] E. Anoardo, F. Grinberg, M. Vilfan, and R. Kimmich, Chem. Phys. **297**, 99 (2004).

# 2

# Theory

This chapter reviews theoretical framework of nuclear magnetic resonance (NMR), focusing on the nuclear spin-lattice relaxation mechanisms in liquid crystal systems. Section 2.1 introduces the basic concepts of nuclear magnetic resonance and Section 2.2 provides an insight into the mechanisms of the spin-lattice relaxation process, which is the main experimental tool for the studies reported in this thesis. The different interactions mediating the relaxation in differing physical systems are described in Section 2.3. Molecular dynamic models appropriate to describe the time modulations of these spin couplings in pure and confined liquid crystal systems are introduced in Section 2.4. A more detailed account of these topics presented in a general and broad perspective, is available in many excellent monographs (see for example, [1–6]).

## 2.1 Fundamental concepts of NMR

When a nucleus having a magnetic moment $\mu$ is kept in a magnetic field $B_0$, the interaction Hamiltonian is given by

$$H = -\vec{\mu}.\vec{B_0} \tag{2.1}$$

The magnetic moment $\vec{\mu}$ is related to the nuclear spin $I$ as $\mu = \gamma\hbar I$, where $\gamma$ is the gyromagnetic ratio associated with the specific nucleus. Taking the field $B_0$ to be along the laboratory $z$-direction, the interaction Hamiltonian is expressed as

$$H = -\gamma\hbar I_z.B_0 \tag{2.2}$$

The eigen values of this Hamiltonian are simple, being only the multiples $(\gamma\hbar B_0)$ of the eigen values of $I_z$. The allowed energies then are

$$E = -\gamma\hbar B_0 m_I \tag{2.3}$$

where $m_I = I$, $I$-1, ----, -$I$. This uniformly split multiplet structure with $(2I+1)$ energy levels, has an energy difference between consecutive levels given by

$$\Delta E = \gamma\hbar B_0 \tag{2.4}$$

as shown in Figure 2.1 for a spin-1/2 nucleus.

For convenience, the two Zeeman eigen states $|I, m\rangle$ of such nuclei $|\frac{1}{2}, \frac{1}{2}\rangle$ and $|\frac{1}{2}, -\frac{1}{2}\rangle$ are represented for convenience by symbols $|\alpha\rangle$ and $|\beta\rangle$, respectively. Due to the negative sign in equation (2.1), the spins with positive gyromagnetic ratios tend to align parallel with the applied field, representing the lowest Zeeman state, and those with negative values of $\gamma$ align antiparallel.

Transitions between these energy levels could be induced by applying an alternating magnetic field $B_1$ perpendicular to $B_0$ with a frequency $\omega_0$, such that

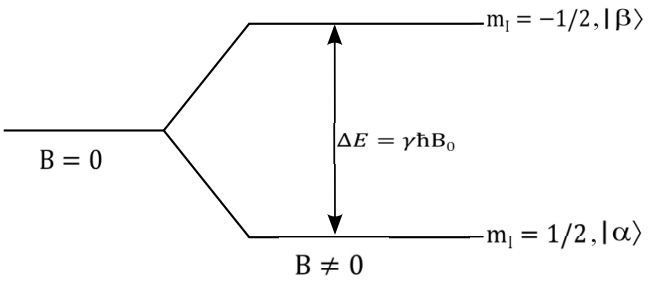


Figure 2.1: The Zeeman splitting of a spin-1/2 particle in a static magnetic field $B_0$. The $|\beta\rangle$ eigenstate is a higher energy state relative to $|\alpha\rangle$.

$$\hbar\omega_0 = \Delta E = \gamma\hbar B_0$$

$$\omega_0 = \gamma B_0. \tag{2.5}$$

The frequency $\omega_0$ is called the Larmor frequency of the nucleus. The relative spin populations of the two levels over an ensemble of spins in equilibrium will follow the Maxweell-Boltzmann distribution, giving rise to a finite bulk magnetization parallel to the applied field, $M_z = M_0$. Any deviations from this distribution, caused by external perturbations for example, are attenuated by the interactions of the spin system with other very many degrees of freedom (called bath or lattice), recovering the equilibrated state over certain characteristic time scales specific to the spin system in that local environment. The mechanism via which the Zeeman populations come to thermal equilibrium with their environment following a disturbance is hence called spin-lattice or longitudinal relaxation, characterized by a time constant $T_1$. The redistribution of energy within the spin system, if necessitated by the non-equilibrium perturbation, is characterized by another time constant $T_2$ referred to as spin-spin or transverse relaxation time.

## 2.2 Spin-lattice relaxation process

There are different approaches developed to explain the way molecular motions could cause spin-lattice relaxation drawing upon interesting physical concepts, *viz.*, quantum mechanical time-dependent perturbation theory [1, 7], concept of a spin temperature [8, 9], application of density matrix formalism [10, 11] etc. These have the common objective of expressing the macroscopic spin relaxation rates as a function of molecular model parameters with an explicit frequency dependence through spectral densities, reflecting the degree of time correlation among the time-modulating molecular processes. Thus the mechanism involves (random) time dependent perturbation of the spin-spin interactions due to various molecular dynamic processes, being identified as bath due to its inherently large heat capacity. Thus, the total Hamiltonian for a spin system is written as

$$H = H_0 + H_1(t). \tag{2.6}$$

Here $H_0$ is the time independent interaction with the applied Zeeman field and $H_1(t)$ is the interaction between nuclear spins, parametrically dependent on the space variables which impart time dependence due to molecular motions. The effect of microscopic motions at the molecular level is thus to make $H_1(t)$ to be time dependent, and in view of very many degrees of freedom involved the time dependence is assumed to be stochastic. The issue of estimating the contribution of a specific type of molecular process to the observed relaxation rate is then concerned with proposing an appropriate random process with physically tractable model parameters. A time dependent perturbation theory yields an expression for transition probability $P(m|m',t)$, connecting the eigenstates $|m\rangle$, $|m'\rangle$ of the Zeeman term, $H_0$, as [2]

$$P(m|m',t) = \frac{1}{\hbar^2}\int_{-\infty}^{+\infty} \langle m|H_1(t)|m'\rangle^2 \exp(-i\omega_{mm'}t)dt \tag{2.7}$$

$W_{mm'} = P(m|m', t)$ is the ensemble averaged transition probability related to the corresponding $T_1$ as

$$T_1 = \frac{1}{W_{mm'}}. \tag{2.8}$$

This ensemble average value $W_{mm'}$ is given by the Fourier transform of the connected time correlation function $G_{mm'}(\tau)$ as [1]

$$W_{mm'} = \frac{1}{\hbar^2} \int_{-\infty}^{+\infty} G_{mm'}(\tau) \exp(-i\omega_{mm'}t) d\tau \tag{2.9}$$

where

$$G_{mm'}(\tau) = \overline{\langle m|H_1(t)|m'\rangle \langle m|H_1(t+\tau)|m'\rangle}. \tag{2.10}$$

Here bar denotes the average over the ensemble of spins. The correlation function $G_{mm'}(\tau)$ quantifies the statistical correlation between the random values of the matrices of the fluctuating Hamiltonian $H_1(t)$ at times $t$ and $t+\tau$. Considering the fluctuations in $H_1(t)$ as stationary and Markovian in time, the correlation function can be further simplified, and be modeled for convenience as

$$G_{mm'}(\tau) = \langle |H_1(0)|^2 \rangle \exp\left(-\frac{\tau}{\tau_c}\right). \tag{2.11}$$

Here $\tau_c$ is the correlation time corresponding to the molecular motions modulating the spin interactions. The Fourier transform of the correlation function defining the spectral density $J_{mm'}(\omega)$, finally relates to the relaxation rate $R_1 = T_1^{-1}$ as (equations (2.8) to (2.11))

$$\frac{1}{T_1} \propto J_{mm'}(\omega). \tag{2.12}$$

The main theoretical problem now is to connect these spectral density

functions to the characteristics of the molecular motions of interest. For a given model of the molecular motion, it is in principle possible to assign an appropriate probability distribution and calculate correlation functions, so as to finally estimate the contribution to the spin relaxation rate via spectral density functions. On the other hand, experimental investigations of these molecular motions begin with measurements on spin relaxation rates primarily as a function of temperature and resonance frequency. Spectral density variations corresponding to the local field fluctuations, which best fit the experimental data over the range of experimental parameters, are then deduced. In order to connect these results to specific molecular models, as well as to account for all the details of the observable features, it is necessary to consider different magnetic interactions between spins in the system, as well as their sensitivity to different types of molecular motions.

In the presence of different molecular motions in the system, each mediating the relaxation process with its individual contribution to the spectral density function, it is customary to consider them to be statistically independent, and express the total relaxation rate as a sum of the individual relaxation rates, *i.e.*,

$$\frac{1}{T_1} = \sum_x \left(\frac{1}{T_1}\right)_x . \tag{2.13}$$

where $x$ denotes the type of mechanism under consideration. Thus in a typical spin system interacting with the bath, estimation of the total relaxation rate involves modelling the different molecular motions and computing the corresponding contributions from each of the mechanisms to the relaxation.

## 2.3 Nuclear magnetic interactions

Spin-lattice relaxation processes in NMR occur only if there are specific interactions involving the nuclear spins and its environment (called as lattice or bath) that can result in energy exchange. These interactions could be of two categories: 1. Magnetic interactions and 2. Electric interactions. There are five types of magnetic interactions of interest to NMR, namely Zeeman ($Z$), dipolar ($D$), J-coupling ($J$), chemical shift ($CS$) and spin-rotation ($SR$) interactions. In the case of nuclei lacking spherical symmetry (quadrupolar nuclei, $I > 1/2$), the coupling of the nuclear quadrupolar moment with the electric field gradient generated by the surrounding charge distribution can lead to an orientation dependent interaction, aiding the spin-lattice relaxation *via* electrostatic interaction. These interactions can also be classified differently depending on whether they are single spin interactions ($Z$, $CS$, $Q$ and $SR$) or pair-wise interactions ($D$ and $J$).

In view of the present work on spin-1/2 nuclei in the wide-line NMR regime, we find that nuclear dipole-dipole interaction and spin-rotation interaction are relevant for discussion, and we accordingly present below details of these interactions, their time modulations by dynamic processes appropriate to the liquid crystal systems under consideration, and finally analytical expressions for their contribution to the nuclear spin-lattice relaxation rates.

### 2.3.1 Dipole-Dipole interaction

The dipolar Hamiltonian between a pair of spins $I$ and $S$ involves second rank tensors is given by (with $L = 2$)

$$H_D = f_d \sum_{m=-2}^{2} A_2^m F_2^{-m} \tag{2.14}$$

where

$$f_d = \frac{\mu_0}{4\pi}\gamma_I\gamma_S\hbar^2. \tag{2.15}$$

Here $\gamma_I$ and $\gamma_S$ are the gyromagnetic ratios of the nuclei $I$ and $S$ respectively. $A_2^m$ and $F_2^{-m}$ represent the spin and spatial tensor components of the Hamiltonian respectively:

$$A^0 = I_z S_z - \left(\frac{1}{4}\right)[I_+ S_- + I_- S_+] \tag{2.16a}$$

$$A^{\mp 1} = -\left(\frac{3}{2}\right)[I_z S_\mp + I_\mp S_z] \tag{2.16b}$$

$$A^{\mp 2} = -\left(\frac{3}{4}\right) I_\mp S_\mp \tag{2.16c}$$

$$F^0 = r_{ij}^{-3}(1 - 3\cos^2\theta) \tag{2.16d}$$

$$F^{\mp 1} = r_{ij}^{-3}\sin\theta\,\cos\theta\,\exp(\pm i\phi) \tag{2.16e}$$

$$F^{\mp 2} = r_{ij}^{-3}\sin^2\theta\,\exp(\pm i\phi). \tag{2.16f}$$

Here $r_{ij}$ is the inter-nuclear distance, $\theta$ and $\phi$ are the polar and azimuthal angles. The operators $I_+(S_+)$ and $I_-(S_-)$ are raising and lowering operators respectively. If both nuclei are spin-$\frac{1}{2}$, then their Zeeman eigen states in the presence of the dipolar interaction have the form $|\alpha\beta\rangle$, forming a four-level system. The dipolar Hamiltonian components can cause transitions between these energy levels as shown in Figure 2.2.

The autocorrelation function is expressed as an ensemble average in terms of the spatial components of the dipolar interaction, $F^m$,

$$G^m(t) = \langle F^{m^*}(t) F^m(t+\tau)\rangle. \tag{2.17}$$

where $F^{m^*}(t)$ represents the complex conjugate of $F^m(t)$ . Consequently the spectral density function is given by

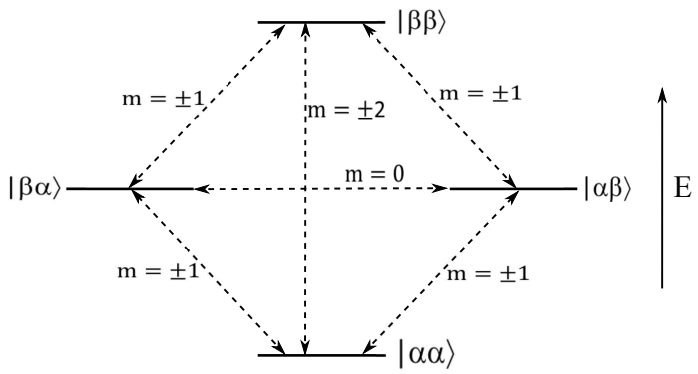


Figure 2.2: Zeeman energy levels of two coupled spin-1/2 nuclei. The number of energy quanta required to make each transition is represented by $m$.

$$J^m(\omega) = \int_{-\infty}^{\infty} G^m(t) e^{-i\omega\tau} d\tau. \tag{2.18}$$

**Like spins**:

Considering this energy level scheme for the two spin-1/2 nuclei, a set of coupled differential equations can be written to describe the evolution of the population of each eigen state, depending on the transition probabilities between the levels. Further assuming that both spins are of the same nuclear species, $\gamma_I = \gamma_S$, the polarization of an ensemble of such systems will be governed by [1]

$$\frac{d}{dt}\langle I_Z + I'_Z\rangle = -\frac{1}{T_1}\left\{\langle I_Z + I'_Z\rangle - \langle I_Z + I'_Z\rangle_0\right\} \tag{2.19}$$

with

$$\frac{1}{T_1} = \frac{3}{2}\gamma^4\hbar^2 I(I+1)\left\{J^{(1)}(\omega_I) + J^{(2)}(2\omega_I)\right\}. \tag{2.20}$$

**Unlike spins**:

In the case of hetero-nuclear spin-1/2 systems where $\gamma_I \neq \gamma_S$, the coupled equations for polarization of an ensemble of each spin system is to be written as [1]

$$\frac{d\langle I_Z\rangle}{dt} = -\frac{1}{T_1^{II}}(\langle I_Z\rangle - I_0) - \frac{1}{T_1^{IS}}(\langle S_Z\rangle - S_0) \tag{2.21}$$

$$\frac{d\langle S_Z\rangle}{dt} = -\frac{1}{T_1^{SI}}(\langle I_Z\rangle - I_0) - \frac{1}{T_1^{SS}}(\langle S_Z\rangle - S_0) \tag{2.22}$$

where

$$\begin{aligned}
\frac{1}{T_1^{II}} &= \gamma_I^2\gamma_S^2\hbar^2 S(S+1)\Big\{\frac{1}{12}J^{(0)}(\omega_I-\omega_S) + \frac{3}{2}J^{(1)}(\omega_I) \\
&+ \frac{3}{4}J^{(2)}(\omega_I+\omega_S)\Big\} && \text{(2.23a)} \\
\frac{1}{T_1^{IS}} &= \gamma_I^2\gamma_S^2\hbar^2 I(I+1)\left\{-\frac{1}{12}J^{(0)}(\omega_I-\omega_S) + \frac{3}{4}J^{(2)}(\omega_I+\omega_S)\right\} && \text{(2.23b)}
\end{aligned}$$

Similar equations for $T_1^{SS}$ and $T_1^{SI}$ are obtained by interchanging the indices $I$ and $S$.

### 2.3.2 Spin-rotation interaction

The spin-rotation interaction arises from magnetic fields generated at a nucleus by the motion of a molecular magnetic moment which arises from the fast rotation of the electronic distribution in a molecule. If the molecule rotated at an angular velocity $\omega$ we shall describe the rotation by an angular velocity index $J$ given by

$$I\omega = J\hbar \tag{2.24}$$

where $I$ is the moment of inertia of the molecule.

The spin-rotation interaction Hamiltonian for a nucleus with spin $S$ is given by [12, 13]

$$H_{SR} = -\hbar\, S.C.J. \tag{2.25}$$

Here $C$ is a dyadic or tensor quantity known as the spin-rotation interaction constant. The expression for spin-lattice relaxation time can in principle be derived by considering the different underlying molecular dynamic processes (*e.g.*, transient rotational model involving sharp jumps between different orientations, or Brownian rotational dynamics). However it was observed that on the much coarser observation time scale of spin-lattice relaxation, these microscopic details tend to be unimportant [13, 14], and the underlying molecular process could be accounted for satisfactorily by assigning a characteristic time ($\tau_{SR}$) associated with it. Thus the relaxation due to spin-rotation is given by [14]

$$\frac{1}{T_1} = \frac{2k_B T\hbar^2 (I_x + I_y + I_z)(C_{xx}^2 + C_{yy}^2 + C_{zz}^2)\tau_{SR}}{9(1 + \omega^2\tau_{SR}^2)}. \tag{2.26}$$

One simplifies this expression further by setting $I_x = I_y = I_z = I$ and $C_{xx} = C_{yy} = C_\perp$ and $C_{zz} = C_\parallel$.

$$\frac{1}{T_1} = \frac{2k_B T\hbar^2 I(2C_\perp^2 + C_\parallel^2)\tau_{SR}}{3(1 + \omega^2\tau_{SR}^2)}. \tag{2.27}$$

Here $C_\parallel$ and $C_\perp$ are the elements of the spin-rotation interaction tensor in the principal axes system along the symmetry axis and a direction perpendicular to it, respectively. $\tau_{SR}$ is the correlation time associated with the angular

momentum fluctuations of the molecule. $T$ is the absolute temperature and $k_B$ is the Boltzman constant. It was shown [13, 14] that for such a system molecule undergoing isotropic Brownian motion in liquid state, the correlation time $\tau_{SR}$, is closely related to the correlation time for the molecular reorientation, $\tau_R$, as

$$\tau_{SR}\,\tau_R = \frac{1}{6k_BT}. \tag{2.28}$$

provided $\tau_{SR} \ll \tau_R$. The correlation time $\tau_R$ is usually estimated from the dipolar contribution to the spin-lattice relaxation. The important distinction between spin-rotation interaction mechanism and the dipole-dipole interaction is that $\tau_{SR}$ becomes larger as the sample temperature increases whereas $\tau_R$ becomes smaller. Thus as the temperature increases, the relaxation rate due to dipole-dipole interaction decreases ($(T_1^D)^{-1} \propto \tau_R$), whereas the relaxation rate due to spin-rotation interaction increases ($(T_1^{SR})^{-1} \propto \tau_{SR}$).

## 2.4 Spin-lattice relaxation models in liquid crystals

Liquid crystals partake the nature of both solids and liquids. So, it is not obvious to take the formulations of spin relaxation theory designed for solids or for liquids to be entirely adequate to interpret the results of spin relaxation measurements in liquid crystals. The anisotropic nature of liquid crystals complicates the analysis of spin relaxation data in these systems. Several dynamic processes are recognized to cause spin relaxation in liquid crystals. Investigation of these dynamic processes in pure liquid crystals and liquid crystals confined to random porous network through NMR relaxometric measurements is the objective of this thesis. These processes may be individual molecular motions or collective dynamics. The individual motions of relevance include translational self-diffusion modulating inter-molecular interactions and reorientations about the molecular axes modulating the intra-

molecular interactions, and these are normally present in all mesophases. The collective motions occur in the mesophases of the liquid crystal as well as near a phase transition point due to critical dynamics. The latter include, for example, pre-transitional effects due to short-range nematic clusters that transiently form near isotropic-nematic transition ($T > T_{NI}$), nematic order parameter fluctuations just below isotropic-nematic transition ($T < T_{NI}$), order director fluctuations (in the mid-nematic phase), diffusion assisted director fluctuations, pretransitional effects due to cybotactic clusters near $N - S_A$ transition ($T > T_{NA}$), layer undulations in the $S_A$ phase (in the mid-smectic phase), slowly relaxing local structures (SRLS) present in different phases, and reorientations mediated by translational displacements (RMTD) due to the surface-fluid interactions in severely confined system. The first part of this section deals with individual motions and the latter discusses the details of collective motions.

## 2.4.1 Individual motions

### 2.4.1.1 Self-diffusion

Diffusion is molecular mass transport usually by thermally activated particle motions, and is a property of liquid crystals. Self-diffusion [15] or translational displacement of molecules is normally interpreted as a consequence of Brownian motions. The translational diffusion constants can be determined by several methods [16]. For example, field gradient NMR diffusometry is a direct technique used to study the self-diffusion (SD). The magnetic field is deliberately made inhomogeneous in a calibrated manner in the sample by the application of a gradient of the field and hence the nuclear spin precession frequency (Larmor frequency) changes in a well-defined way with the position of the spins in the sample, *i.e.* a frequency-space relation is generated by the application of pulse gradient of the magnetic field $B_0$. Diffusing spins, therefore, undergo Larmor frequency changes in time, caused by the diffusional motions of the molecules, to which they belong. The effect of

these frequency changes on the amplitude of the nuclear spin echo can be calculated and hence the diffusion coefficient can be obtained [1]. The measurement is a determination of the mean square displacement of the diffusing spins in the gradient field during a certain time interval. In contrast, the indirect NMR methods use relaxation time measurements (*e.g.*, $T_1, T_{1D}, T_{1\rho}$) to deduce information on the diffusional motions from their temperature and frequency dependences [17, 18].

The dipole-dipole interaction between protons on different molecules gets modulated as the molecules diffuse from one site to another, and has potential to lead to considerable contribution to the spectral densities at the appropriate Larmor frequency range. This is an important mechanism for spin-lattice relaxation in liquid crystals. Torrey [19] derived an expression for spin lattice relaxation rate $T_1^{-1}$ in an isotropic liquid using random-flights model [15]. In order to find the time correlation function of the spatial parts of the dipolar Hamiltonian, the probability function is derived from the random flights model, and using an approximate expression for the same, the diffusion coefficient $D$ was found to obey the relation,

$$D = \frac{\langle r^2 \rangle}{6\tau_D}. \qquad \boxed{2.29}$$

Here $\langle r^2 \rangle$ is the mean-square flight distance of the molecule and $\tau_D$ is the (average) time between each flight. But this expression for the diffusion coefficient is not sufficient to describe the diffusion process in liquid crystals because the ordering in these systems leads to anisotropy in the diffusion coefficients ($D$) (the diffusion coefficient along the director ($D_\parallel$) and that in the perpendicular direction ($D_\perp$) being different).

Zumer and Vilfan [20] extended Torreys theory for isotropic liquids to an anisotropic medium by taking into account the anisotropy of molecular diffusion, with an assumed cylindrical shape of the molecules, and the specific distribution of protons along the long molecular axis, to obtain the relaxation

rate for the self-diffusion. This is given by [20],

$$\frac{1}{T_1} = \frac{9}{8}\gamma^4\hbar^2\frac{n\tau}{d^3}Q\left[\omega\tau_D, \frac{\langle r_\perp^2\rangle}{a^2}, \frac{D_\parallel^0}{D_\perp^0}\right]. \tag{2.30}$$

Here $Q$ is a dimensionless and numerically obtainable function. $a$ is the diameter of the cylinder. And $D_\parallel^0$ and $D_\perp^0$ are the macroscopic self-diffusion constants of the perfectly aligned liquid-crystalline phase and are given by,

$$D_\perp^o = \frac{< r_\perp^2 >}{4\tau_\perp} \quad and \quad D_{||}^o = \frac{< r_{||}^2 >}{2\tau_{||}}. \tag{2.31}$$

The value of $\frac{D_\perp^0}{D_\parallel^0}$ is examined taking data from different experiments [21–23], and it was observed that it would not differ much for different nematic compounds. The anisotropic results in these nematic compounds were found to reduce to the familiar Torrey's equation [19] in the limit $\omega\tau_D < 0.3$, as

$$T_1^{-1}(\omega) = C - F\omega^{1/2}. \tag{2.32}$$

Here $C$ and $F$ are the constants related to the average diffusion coefficient $D$ as [24]

$$F = -4.88 \times 10^{-14} p(1+\delta)D^{-3/2} \tag{2.33}$$

and

$$C \propto D^{-1}.$$

In the frequency region of interest in the NMR experiment, spin relaxation rate can be shown to follow the Torrey's model in the isotropic phase but is lower by a scalar factor of 1.4 in the nematic and smectic-A phases [20, 25]. The $T_{1SD}^{-1}$ can essentially be written as

$$\frac{1}{T_{1SD}} = \frac{1}{1.4} T^{-1}_{1Torrey}. \tag{2.34}$$

In the limit $\omega\tau_D < 1$, the relaxation rate $T^{-1}_{1SD}$ can be written as (isotropic approximation) [20]

$$\frac{1}{T_{1SD}} = \frac{B}{\omega}(f(x) + f(\sqrt{2}x)) \tag{2.35}$$

where

$$f(x) = \frac{2}{x^2}\Bigg\{ v\left[1 - \frac{1}{(u^2+v^2)}\right] \quad + \quad \left[v\left(1 + \frac{1}{(u^2+v^2)}\right) + 2\right] e^{-2v} cos2u$$
$$+ \quad u\left[1 - \frac{1}{(u^2+v^2)}\right] e^{-2v} sin2u \Bigg\} \tag{2.36}$$

$$\begin{pmatrix} u \\ v \end{pmatrix} = \frac{(\omega a^2/2D)^{1/2}}{(4+\omega^2\tau_D^2)^{1/4}} \left\{ 1 \mp \frac{\omega\tau_D}{(4+\omega^2\tau_D^2)^{1/2}} \right\}^{1/2}$$

and

$$x = \left(\frac{\omega a^2}{D}\right)^{1/2}.$$

Here $D$ is the average diffusion coefficient with a correlation time $\tau_D$ given by $a^2/6D$ and $a$ is the closest distance of approach of two molecules (taken to be the diameter of the molecules, $\sim 5A^0$). In the limit, $\omega\tau_D \gg 1$, the relaxation rate reduces to the $T^{-1}_{1SD} \sim \omega^{-2}$ law.

#### 2.4.1.2 Reorientations

Liquid crystals having anisotropic molecular shape and with flexible groups undergo three types of rotational motions [26]: (a) fast reorientations around the long axis (b) reorientations about the short axes and (c) fast (isotropic) tumbling of the end chains.

The rotations (reorientations) around the long molecular axis are usually very fast and do not contribute significantly towards spin relaxation in nematic and high temperature smectics. In low temperature smectic phases on the other hand, rotations around the long axis may slow down considerably, and become important. For the case that the directorn $\hat{n}$ makes an angle $\Delta$ with the direction of the external magnetic field, one finds for fast rotations around the long molecular axis $\omega\tau_l \ll 1$

$$\frac{1}{T_{1RL}} = \frac{9}{64}\gamma^4\hbar^2 r^{-6}\frac{18\tau_l}{32}(1 + 3cos^2\Delta). \tag{2.37}$$

The relaxation rate for rotations about the short molecular axes in various mesophases is approximated to a BPP-like relation [7] and is written as

$$\frac{1}{T_{1R}} = A_R\sum_{p=1}^{2} p^2\frac{\tau_R}{1 + (p\omega\tau_R)^2} \tag{2.38}$$

where $A_R = \varepsilon C_1$ and $\varepsilon$ measures the anisotropy of local reorientations around the short axis. The constant $C_1$ for a molecule consisting of aliphatic groups in the core and aromatic groups in the end chains is given by

$$C_1 = \frac{9}{8}\gamma^4\hbar^2\frac{1}{15}\sum_k \frac{u_k(3l_k^2 - 1)^2}{r_k^6}. \tag{2.39}$$

Here $u_k$ stands for the ratio of protons belonging to $k^{th}$ group, to the total number of protons in the molecules, $l_k$' s are cosines of angle between internuclear vector $r_k$ of $k^{th}$ group and the long axis. In the limit $\omega\tau_R \ll 1$ the relaxation rate due to reorientations around short axis gives rise to frequency independent contribution given by,

$$\frac{1}{T_{1R}} = 5\varepsilon A_R\tau_R. \tag{2.40}$$

Usually, Arrhenius type of temperature dependence is assumed for $\tau_R$ since the reorientations are thermally activated, and hence $\tau_R$ is expressed as

$$\tau_R = \tau_0 \exp\left(\frac{E_{as}}{k_B T}\right). \tag{2.41}$$

Here $\tau_0$ is the pre-exponential factor and $E_{as}$ is the activation energy associated with the specific dynamic process ($k_B$ is the Boltzmann constant). Thus, a plot of $\ln(T_1)$ *vs* $T$ will asymptotically have two straight lines with slopes -$E_{as}/k$ and $E_{as}/k$ at higher and lower temperatures, respectively.

In ordered smectics rotations around the short molecular axis are known to be frozen [27]. The rotation about the long axis could however be still fast. The main contribution expected for $T_1^{-1}$ is due to the isotropic tumbling of the end chains [26], and is expressed as

$$\frac{1}{T_{1Re}} = C_1 \left[\frac{\tau_{ce}}{1+\omega^2\tau_{ce}^2} + \frac{4\tau_{ce}}{1+4\omega^2\tau_{ce}^2}\right]. \tag{2.42}$$

Here the constant $C_1$ represents the relative weights of end chain protons with respect to the total number of protons. $\tau_{ce}$ is the correlation time associated with the reorientations of the end chains. Assuming $\tau_{ce}$ to have an Arrhenius type of temperature dependence,

$$\tau_{ce} = \tau_0 \exp\left(\frac{E_{ce}}{k_B T}\right). \tag{2.43}$$

The $T_{1Re}$ shows a minimum at $\omega\tau_{ce} = 0.616$ and at this value

$$\frac{1}{T_{1Re}} = 1.43 C_1/\omega. \tag{2.44}$$

Further, at high temperatures, *i.e.* where $\omega\tau_{ce} \ll 1$

$$\frac{1}{T_{1Re}} = 5C_1\tau_{ce}, \tag{2.45}$$

thus making $T_{1Re}^{-1}$ frequency independent but strongly temperature dependent.

At temperatures well below the $T_1$ minimum, *i.e.* when $\omega\tau_{ce} \gg 1$

$$\frac{1}{T_{1Re}} = 2C_1/\omega^2\tau_{ce}. \tag{2.46}$$

## 2.4.2 Collective motions

### 2.4.2.1 Critical fluctuations ($T > T_{NI}$)

As has been discussed in the earlier chapter, the isotropic-nematic (IN) transition is a weak first-order transition and is satisfactorily described within the general formulation of the Landau theory [28] of second-order phase transition. Near the clearing temperature, short-range nematic order is encountered in the isotropic liquid and the orientations of the molecules are correlated spatially over a finite distance known as coherence length $\xi$. The pretransitional effects, which manifest, for example, as critical anomalies in magnetic relaxation measurements, are caused by fluctuations in the order parameter appropriate to the particular transition [29]. Fluctuations in the local order increase rapidly as this almost second-order phase transition is approached from above. The critical temperature $T_{NI}^*$, at which a second-order phase transition would occur, is usually within $1^o$C below $T_{NI}$, the observable transition temperature. The short-range order effects in the isotropic phase of nematics and cholesterics are discussed earlier [28]. These remarkable effects had been observed and studied by NMR [30–32], and by other suitable probing techniques, like light scattering experiments [33, 34].

Just above $T > T_{NI}$, the fluctuations in the orientation of the local

nematic order, having slowed down enough to match the NMR time scales, contribute to the relaxation rate. The fluctuations in the short-range order *i.e.* forming and breaking of the nematic clusters, modulate the dipolar interaction between the spins. The relaxation rate due to short-range nematic order ($R_{1CF} = 1/T_{1CF}$) is given by [3, 35]

$$\frac{1}{T_{1CF}} = A_{CF}\left[\frac{\tau_{CF}}{1+\sqrt{1+\omega^2\tau_{CF}^2}}\right]^{1/2}. \tag{2.47}$$

Here $A_{CF} = A^{'}T\sqrt{\eta}$ is a temperature dependent parameter, $A^{'}$ is a temperature independent quantity, $\eta$ is the effective viscosity and $\tau_{CF}$ is the average correlation time of the short-range nematic order. It is expressed as

$$\tau_{CF} = \frac{\eta\xi^2}{L}.$$

Here $\xi$ is the correlation length that measures the distance over which the local order persists in the isotropic phase and is given by,

$$\xi = \sqrt{\frac{L}{a(T-T_{NI}^{*})^{\gamma}}} \tag{2.48}$$

($a > 0$ is temperature independent and $\gamma = 1$ in the mean field approximation), $T_{NI}^{*}$ is the critical temperature slightly below $T_{NI}$ and $L$ is related to elastic constants. Assuming an Arrhenius-like behavior for $\eta$, its temperature dependence is expressed as

$$\eta = \eta_0 \exp\left(\frac{E_{CF}}{RT}\right)$$

where $E_{CF}$ is the activation energy for this process. Thus, the complete dependence of $\tau_{CF}$ and the CF term on $T$ will be

$$\tau_{CF} = \tau_{CF0}\frac{\exp(E_{CF}/RT)}{T - T^*_{NI}} \tag{2.49}$$

and

$$\frac{1}{T_{1CF}} = AT\exp\left(\frac{E_{CF}}{2RT}\right)\sqrt{\frac{\tau_{CF0}\exp(E_{CF}/RT)/T - T^*_{NI}}{1+\sqrt{1+\omega^2\left(\frac{\tau_{CF0}\exp(E_{CF}/RT)}{T-T^*_{NI}}\right)^2}}}. \tag{2.50}$$

Here $\tau_{CF0}$ is a constant.

For small frequencies [36], wherein the condition $\omega\tau_{CF} \ll 1$ is fulfilled for the whole temperature range, we find from (2.47) and (2.50) that

$$\frac{1}{T_1} = \frac{AT\exp(E_{CF}/RT)}{(T - T^*_{NI})^{1/2}} \tag{2.51}$$

$$T_1 \propto \xi^{-1} \propto (T - T^*_{NI})^{\gamma/2} \neq f(\omega).$$

Thus $T_1$ is strongly dependent on temperature but independent of frequency.

In the case of large Larmor nuclear frequencies, on the other hand, *i.e.* $\omega\tau_{CF} \gg 1$

$$\frac{1}{T_1} \propto \frac{1}{\sqrt{\omega}}.$$

Thus

$$T_1 \propto \sqrt{\omega} \neq f(T).$$

In this case, $T_1$ is proportional to the square root of frequency but is weakly dependent of temperature. This discussion is appropriate close to $T_{NI}$ where $\xi$ becomes large [32, 36].

#### 2.4.2.2 Order parameter fluctuations (Just below $T < T_{NI}$)

In contrast to short range nematic order fluctuations in the isotropic phase ($T > T_{NI}$), just below $T_{NI}$, fluctuations in the magnitude of the nematic order parameter $S$ are effective in relaxing nuclear spins, *i.e.*, the fluctuations in long-range orientational order modulates the dipole-dipole interactions between nuclear spins and influence the NMR spin relaxation. In particular, if these order parameter fluctuations (OPF) are dominant in comparison to the order director fluctuations (ODF), then the following spectral density model due to OPF is adequate to account for the observed relaxation process. The spectral density due to the OPF is expressed as [3]

$$J_{m_L}(m_L\omega) = A_{OPF}\left[\frac{\tau_{OPF}}{1+\sqrt{1+\left(m_L\omega\tau_{OPF}\right)^2}}\right]^{1/2} \tag{2.52}$$

where

$$A_{OPF} = \frac{k_B T}{4\sqrt{2}\pi L_N}\sqrt{\frac{\nu_N}{L_N}}\left[\kappa(0,m_L)\right]^2.$$

Here $[\kappa(0,m_L)]^2$ are the mean square averages of the Wigner rotation matrices expressed as a power series in $S$ [29]. These $\kappa$ values are needed to reduce the importance of the order parameter fluctuations as the orientational ordering increases far below $T_{NI}$ and the $\tau_{OPF}$ value is given by

$$\tau_{OPF} = \frac{\nu_N \xi_N^2}{L_N}. \tag{2.53}$$

Here $\nu_N$, $L_N$ and $\xi_N$ are the values of corresponding nematic viscosity,

elastic constant and coherence length, respectively. We may now distinguish two different cases

Case 1. In case of small Larmor frequencies *i.e.*, $\omega\tau_{OPF} \ll 1$

$$T_1 \propto \xi_N^{-1} \propto (T_{NI}^{+} - T)^{\nu'} \neq f(\omega).$$

where the critical exponent $\nu'$ has a mean field value of 1/2 . However, $\nu'$ has been found to be temperature dependent and takes an effective value of 2/5.

Case 2. In case of large Larmor frequencies *i.e.*, $\omega\tau_{OPF} \gg 1$

$$\frac{1}{T_1} \propto \frac{1}{\sqrt{\omega}}.$$

Thus

$$T_1 \propto \sqrt{\omega} \neq f(T).$$

In this case, $T_1$ is proportional to the square root of frequency but is weakly dependent on temperature.

#### 2.4.2.3 Order director fluctuations (mid nematic phase)

Order director fluctuations are a process of a collective nature. Of the various dynamic processes, which influence nuclear spin relaxation rates, phenomenon of director fluctuations is the one unique to liquid crystals. In the mid nematic phase order director fluctuations (ODF) constitute the dominant spin relaxation mechanism. These are treated as a superposition of normal modes of the elastically coupled entity of molecules in a liquid crystalline domain. There was much effort in the development of relaxation models to interpret the nuclear spin relaxation due to the director fluctuations. The failure of BPP-like model for nematic liquid crystals (*viz.* absence of

Lorentzian type frequency of relaxation rate) led Pincus [37] to derive the first expression for relaxation due to director fluctuations. Starting from this early model for the nuclear magnetic relaxation due to director fluctuations under the one elastic constant approximation ($K_1 = K_2 = K_3$; the Frank elastic coefficients), several improvements were made by many authors and these are discussed below.

The relaxation processes is considered to be due to the intra-molecular dipolar interactions that are modulated by hydrodynamic order director fluctuation modes. The free energy density of a bulk nematic liquid crystal in terms of splay ($K_1$), twist ($K_2$) and bend ($K_3$) is given by

$$f = \frac{1}{2}\left[K_1(div\ n)^2 + K_2(n.\ curl\ n)^2 + K_3(n \times curl\ n)^2\right]. \qquad (2.54)$$

The deformational free energy density is given by

$$f = \frac{1}{2V}\left[K_1\left(\frac{\partial n_x}{\partial x} + \frac{\partial n_y}{\partial y}\right)^2 + K_2\left(\frac{\partial n_y}{\partial x} - \frac{\partial n_x}{\partial y}\right)^2 + K_3\left[\left(\frac{\partial n_x}{\partial z}\right)^2 + \left(\frac{\partial n_y}{\partial z}\right)^2\right]\right]. \qquad (2.55)$$

In order to emphasize the spatial dependence of the orientation of the local director we define $n_x(r), n_y(r)$ as the Cartesian component at point $r$. The transverse component is now expressed in terms of the mode expansion

$$n_x(r) = V^{-1/2}\sum_q n_x(q)\exp(-iq.r) \qquad (2.56a)$$

$$n_y(r) = V^{-1/2}\sum_q n_y(q)\exp(-iq.r) \qquad (2.56b)$$

where $V$ is the volume. Substitution of these modes into equation (2.55),

evaluation of the gradients and their integration over the volume yields the total deformation energy as

$$\begin{aligned} F &= \frac{1}{2V}\sum_{q}\Big\{K_1|n_x(q)q_x + n_y(q)q_y|^2 \\ &+ K_2|n_x(q)q_y - n_y(q)q_x|^2 \\ &+ K_3 q_z^2\left[|n_x(q)|^2 + |n_y(q)|^2\right]\Big\}. \end{aligned} \tag{2.57}$$

The above quadratic form, when suitably diagnolized, yields two uncoupled transverse modes $n_\alpha(q)$; $\alpha = 1, 2$. ($n_1(q)$ lies in the plane of $(q, n)$ and is given by a combination of $K_3$ and $K_1$, while $n_2(q)$ is perpendicular to the plane $(q, n)$ and is a combination of $K_3$ and $K_2$). Defining $q_\parallel = q_z^2$ and $q_\perp^2 = q_x^2 + q_y^2$, equation (2.57) may be rewritten as

$$F = \frac{1}{2V}\sum_{q}\sum_{\alpha=1}^{2}|n_\alpha(q)|^2\left[K_3 q_z^2 + K_\alpha q_\perp^2\right]. \tag{2.58}$$

The transverse mode $n_\alpha(q,t)$ relaxes exponentially as

$$n_\alpha(q,t) = n_\alpha(q,0)\exp\left(-t/\tau_\alpha(q)\right)$$

with a damping time given by

$$\tau_\alpha(q) = \frac{\eta_\alpha}{K_3 q_z^2 + K_\alpha q_\perp^2}, \quad \alpha = 1, 2. \tag{2.59}$$

where $\eta_\alpha = \Gamma^{-1}$ is closely related to the appropriate viscosity coefficient. The frequencies of the two transverse modes go to zero in the long wavelength limit ($q \to 0$) in the nematic phase [38]. The mean square amplitude of each mode is obtained from the equipartition theorem as

$$\langle|n_\alpha(q)|^2\rangle = \frac{k_B T V}{(K_3 q_z^2 + K_\alpha q_\perp^2)}, \quad \alpha = 1, 2. \tag{2.60}$$

The spectral densities are obtained from the correlation function associated with these fluctuations leading to the modulation of the intra-molecular dipolar interactions. However these correlation functions have to be transformed from the magnetic-field-fixed frame (laboratory frame) to the director-fixed frame, and finally to the molecular-fixed frame, through proper Wigner rotation matrix elements. Such a transformation results in

$$G(t) = \langle F_h(0)F_h^*(t)\rangle = f_h(\Delta)\langle F_1(0)F_1^*(t)\rangle = f_h(\Delta)S^2\langle \delta n(r,0)\delta n(r,t)\rangle. \tag{2.61}$$

Here $S = \frac{1}{2}\langle 3cos^2\theta - 1\rangle$ is the nematic order parameter and the term $\Delta$ in the function $f(\Delta)$ is the angle between the magnetic field and the director. The corresponding spectral density is given by

$$J_h(p\omega) = f_h(\Delta)S^2 \int_{-\infty}^{\infty} e^{-ip\omega t}\langle \delta n(r,0)\delta n(r,t)\rangle dt. \tag{2.62}$$

Introducing the Fourier components of the director fluctuations of the nematic order (equation (2.56)) the spectral density is given by

$$J_h(p\omega) = f_h(\Delta)S^2 \int_{-\infty}^{\infty} e^{-ip\omega t} \sum_q \sum_{\alpha=1}^{2} \langle |n_\alpha(q)|^2\rangle e^{\tau/\tau_\alpha(q)} dt. \tag{2.63}$$

*Isotropic visco-elastic coefficients:*

In the one-constant approximation $K_1 = K_2 = K_3 = K$ and $\eta_1 = \eta_2$. This leads to a simple expression for the relaxation time

$$\tau_q = \frac{\eta}{Kq^2}.$$

Since the ODF modes should be restricted on physical grounds by longest and shortest possible wavelengths, the existence of upper and lower bounds

for frequencies should be considered. Thus it is necessary to impose a high-frequency cutoff wave vector $q_c = 2\pi/\lambda_c$ in the above integral. The spectral density function $J_1(\omega)$ can then be written as

$$J_1(\omega) = \frac{3k_BTS^2}{2\pi^2 K}\int_{-\infty}^{\infty} dt \int_0^{q_c} dq \exp\left(-tKq^2/n - i\omega t\right) \tag{2.64}$$

$$= \frac{3k_BTS^2}{4\sqrt{2}\pi K}\left(\frac{\eta}{K^3}\right)\omega^{-1/2}U\left(\frac{\omega_c}{\omega}\right) = AS^2\omega^{-1/2}U\left(\frac{\omega_c}{\omega}\right) \tag{2.65}$$

where $\omega_c = q_c^2 K/\eta$ and the cutoff function $U\left(\omega_c/\omega\right)$is given by

$$\begin{aligned} U\left(\frac{\omega_c}{\omega}\right) &= \frac{1}{2\pi}\ln\frac{\{\omega_c/\omega - (2\omega_c/\omega)^{1/2} + 1\}}{\{\omega_c/\omega + (2\omega_c/\omega)^{1/2} + 1\}} \\ &+ \frac{1}{\pi}\left\{\arctan\left[(2\omega_c/\omega)^{1/2} - 1\right] + \arctan\left[(2\omega_c/\omega)^{1/2} + 1\right]\right\}. \end{aligned} \tag{2.66}$$

The value of the wave vector corresponding to the high frequency cutoff, $q_c$, is usually assumed to be determined by the length of the mesogenic molecules *i.e.*, $\lambda_c = 2\pi/q_c \approx 30A^0$. Given typical values of $K$ in the range of $10^{-12} - 10^{-11}N$ and $\eta = 0.1P$ this corresponds to cutoff frequencies in the range of typical Larmor frequencies.

*Anisotropic viscoelastic constants:*

For nematics which have underlying smectic phases, the elastic constants are no more isotropic (the bend ($K_3$) and twist ($K_2$) elastic coefficients diverge critically as the nematic-smectic-A transition is approached) [39]. Hence one constant approximation is no longer adequate in evaluating the spectral density. A fully anisotropic spectral density expression was first derived by considering the anisotropic nature of the viscoelastic coefficients by Brochard and Blinc [39, 40]. But their expression does not reduce to that of

Pincus under one constant approximation. Vold and Vold [41, 42] have modified these formulae by considering ellipsoidal volume of integration for the $q$-modes instead of a cylindrical volume, in which case it reduces to Pincus model under one constant approximation. The spectral density in this case can be written as

$$J_1(\omega) = \frac{9k_BTS^2}{64\pi^2}\sum_\alpha \eta_\alpha \int_0^{q_z} dq_z \int_0^{q_{\perp c}\left(1-\frac{q_z^2}{q_{zc}^2}\right)^{1/2}} \frac{q_\perp dq_\perp}{\left(K_3q_z^2 + K_\alpha q_\perp^2\right)^2 + \eta_\alpha^2\omega^2}. \tag{2.67}$$

The above equation differs from that of Blinc's expression [36] in that the upper limit of the integral over $q_\perp$ has been modified to represent an ellipsoidal volume of integration, whose cross section in the $(q_x, q_y)$ plane is a circle of radius $q_{\perp c}$ and the maximum excursions along $q_z$ axis are $\pm q_{zc}$. To simplify the above integration we define

$$A_\alpha^2 = \frac{K_\alpha q_{\perp c}^2}{\eta_\alpha\omega}, \quad B_\alpha^2 = \frac{K_3 q_{zc}^2}{\eta_\alpha\omega}; \quad D_\alpha = |B_\alpha^2 - A_\alpha^2|. \tag{2.68}$$

The final expression for $J_1(\omega)$ can be written as [41, 42]

$$\begin{aligned}
J_1(\omega) &= \frac{3k_BTS^2}{8\pi\sqrt{2}\omega}\sum_\alpha \frac{1}{K_\alpha}\left[\frac{\eta_\alpha}{K_3}\right]^{1/2}\left\{\frac{1}{2\pi} ln\frac{B_\alpha^2 - B_\alpha\sqrt{2}+1}{B_\alpha^2 + B_\alpha\sqrt{2}+1} + \frac{1}{\pi}\arctan\left(B_\alpha\sqrt{2}-1\right)\right. \\
&+ \frac{1}{\pi}\arctan\left(B_\alpha\sqrt{2}-1\right) \\
&+ \frac{B_\alpha\sqrt{2}/2\pi}{\sqrt{2D\sqrt{1+A_\alpha^4} \mp A_\alpha^2}} ln\left[\frac{\sqrt{1+A_\alpha^4} \pm \sqrt{2D\sqrt{1+A_\alpha^4} \mp A_\alpha^2} + D}{\sqrt{1+A_\alpha^4} \mp \sqrt{2D\sqrt{1+A_\alpha^4} \mp A_\alpha^2} + D}\right] \\
&\mp \frac{B_\alpha\sqrt{2}/\pi}{\sqrt{2D\sqrt{1+A_\alpha^4} \pm A_\alpha^2}}\left[\arctan\frac{\sqrt{2}D - \sqrt{\sqrt{1+A_\alpha^4} \mp A_\alpha^2}}{\sqrt{\sqrt{1+A_\alpha^4} \pm A_\alpha^2}}\right. \\
&+ \left.\left.\arctan\frac{\sqrt{2}D + \sqrt{\sqrt{1+A_\alpha^4} \mp A_\alpha^2}}{\sqrt{\sqrt{1+A_\alpha^4} \pm A_\alpha^2}}\right]\right\}.
\end{aligned} \tag{2.69}$$

The spectral density for one constant approximation can be recovered from the above expression since the ellipsoidal of integration reduces to a sphere and $A_\alpha \to B_\alpha$ *i.e.*, $D \to 0$ for the isotropic nature of elastic constants. The frequency dependence of $J_1(\omega)$ as a function of three elastic constants for different combinations is shown in Figure 2.3. The values chosen are $K_1 = K_2 = 10^{-6}$ dyn, $\eta_1 = \eta_2 = 0.5$P, $\lambda_{zc} = \lambda_{\perp c} = 30A^0$ and $J_1(\omega)$ is plotted for different values of $K_3$ in the range $10^{-9} - 10^{-3}$ dyn. For Larmor frequencies well above the cutoff frequency $\omega_c$, the absolute value of $J_1$ is small and drops off as $\omega^{-2}$.

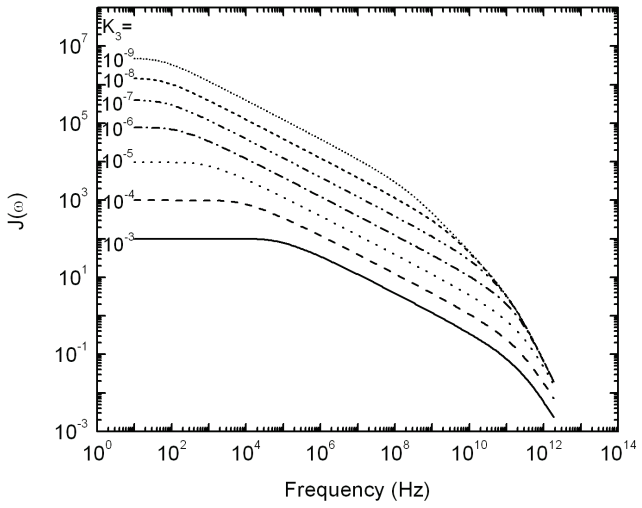


Figure 2.3: The spectral density$J_1(\omega)$ plotted as a function of frequency according to equation (2.69) and a variable elastic constant $K_3$. The other parameters are explained in the text.

Two distinct limiting cases can be observed from Figure 2.3.

Case 1: $\omega \ll \omega_c$

In the region where $\omega \ll \omega_c$ the frequency dependence of $J_1(\omega)$ is seen to vary from -1 to -1/2 as the value of $K_3$ changes from $K_3 \ll K_1, K_2$ to $K_3 \gg K_1, K_2$ respectively.

Case 2: $\omega \gg \omega_c$

In this case, $J_1(\omega)$ varies from $\omega^{-2}$ to $\omega^{-2/3}$ as $K_3$ is varied from $K_3 \ll K_1, K_2$ to $K_3 \gg K_1, K_2$.

The situation where $K_3 \ll K_1, K_2$ is equivalent to pseudo 2d systems in which the bend elastic term, $K_3$ does not contribute to the free energy and hence the relaxation mechanism for such systems results in a $\omega^{-1}$ dependence of $J_1(\omega)$ at low frequencies. Thus depending on the particular combination of elastic constants and viscosities, somewhat steeper frequency dependence than $\omega^{-1/2}$ can occur especially as the Larmor frequency approaches $\omega_c$.

Struppe and Noack [43] obtained an expression including both upper and lower cutoff frequencies but under single constant approximation. But the situation is more complex in nematics with underlying smectic phases: the visco-elastic properties are perceptibly more anisotropic on one hand; and the presence of cybotactic clusters (smectic organizations) may impose restrictions on the director fluctuations modes leading to the upper and lower cutoff frequencies. As is clear from the above, it is necessary to incorporate both upper and lower cutoff frequencies as well as anisotropy in elastic coefficients in the contribution to spin relaxation from DF modes. Venu and Sastry proposed a model by considering the lower and upper cutoff frequencies and anisotropy in elastic coefficients [44]. The details of this model were discussed elsewhere [45, 46]. The model predicts that $R_{1ODF}$ is frequency independent below any of the lower cutoff frequencies and it varies as $\omega^{-1/2}$ in the intermediate region between upper and lower cut off frequencies and varies as $\omega^{-1.5} - \omega^{-2}$ above upper cut off frequencies. The values of the cutoff frequencies vary due to the variations in elastic coefficients or due to the variations in the corresponding cutoff wavelengths.

#### 2.4.2.4 Layer undulations

The director fluctuations have less freedom in the smectic phase compared to the nematic because of the formation of layered structure. These structures impose severe constraints on the twist ($K_2$) and bend ($K_3$) elastic deformations. Energetically least expensive are layer undulations, which are pure splay deformations and spread in two dimensions *i.e.*, in the plane of the layer [3]. The spin relaxation caused by layer undulations in the smectic-A was first observed by Blinc *et al.* [40] in the smectic phases of Terephtal-bis-butylaniline (TBBA). The relaxation rate expression for this process can be derived from equation (2.69) by defining the following quantities [3]

$$\omega_{zc}^{\alpha} = \frac{K_3 q_{zc}^2}{\eta_\alpha}$$

and

$$\omega_{\perp c}^{\alpha} = \frac{K_\alpha q_{\perp c}^2}{\eta_\alpha}.$$

If $A_\alpha^2 \gg 1$ and $B_\alpha^2 \ll 1$ (*i.e.*, $\omega_{zc}^{\alpha} \ll \omega \ll \omega_{\perp c}^{\alpha}$) in equation (2.69), then the spectral density may be written as ($K_3 \ll K_2 = K_1$)

$$J_1(\omega) = \frac{3k_B T q_{zc}}{4\pi K_1}\omega^{-1}$$

$$= \frac{3k_B T}{2K_1 \xi_z}\omega^{-1} \qquad (2.70)$$

where $\xi_z$ is the coherence length in the $z$-direction of the part of the sample when the layers are parallel to each other, and is defined by $\xi_z = 2\pi/q_{zc}$ . The corresponding relaxation rate is [3]

$$\frac{1}{T_{1LU}} = A_{LU}\omega^{-1} \qquad (2.71)$$

where

$$A_{LU} = \frac{9}{8\pi}\left(\frac{\mu_0\gamma^2\hbar}{4\pi r^3}\right)^2 \frac{k_B T S^2}{K_1\xi_z}\left[d^2_{00}(\beta)\right]^2. \qquad (2.72)$$

Here $d^2_{00}(\beta)$ are Wigner rotation matrices. The above result is true if $\xi_z$ is independent of $q_\perp$ (*i.e.*, constant). If, however, this coherence length is wave vector dependent [28], *i.e.*,

$$\xi = \frac{1}{\lambda q_\perp^2}.$$

where $\lambda$ is a constant of the order of molecular length, a logarithmic dependence of $T_1$ is obtained [36]:

$$T_1^{-1} \propto \ln\left(1 + (\omega_{\perp c}/\omega)^2\right).$$

Here only the upper cutoff frequency was taken into account. This equation diverges as $\omega \to 0$. Sebastiao *et al.* [47–49] considered both the lower and upper cutoff frequencies in deriving an expression for the spectral density and it is expressed as

$$J_1(\omega) = \frac{3k_B T}{2K_1\xi_z\omega}\left(\frac{2}{\pi}\tan^{-1}\frac{\omega_c}{\omega} - \frac{2}{\pi}\tan^{-1}\frac{\omega_l}{\omega}\right) \qquad (2.73)$$

Where $\omega_c = K_1 q_c^2/\eta$ and $\omega_l = K_1 q_l^2/\eta$ are the high and low frequency cutoffs, respectively. In terms of coherence lengths $\xi_z$ and $\xi_\perp$, $q_c = 2\pi/\xi_z$ and $q_l = 2\pi/\xi_\perp$ . Therefore the expression for $A_{LU}$ in equation (2.71) is now given by

$$A_{LU} = \frac{9}{8\pi}\left(\frac{\mu_0\gamma^2\hbar}{4\pi r^3}\right)^2 \frac{k_B T S^2}{K_1\xi_z}\left[d^2_{00}(\beta)\right]^2\left(\frac{2}{\pi}\tan^{-1}\frac{\omega_c}{\omega} - \frac{2}{\pi}\tan^{-1}\frac{\omega_l}{\omega}\right). \qquad (2.74)$$

This equation reduces to equation (2.72) when $\omega_l \to 0$ and $\omega_c = \infty$.

#### 2.4.2.5 Reorientations mediated by translational displacements (RMTD)

In systems where low molecular mass calamitic molecules are confined in small nano-size porous cavities, or in chiral systems, the molecular translational displacements and molecular rotational motions can be mutually affected by the local structure of the matrix. The orientational time correlation of molecules decays partly as a consequence of their translational displacements along the rugged and/or curved surfaces relative to which the molecules in the adsorbed or surface ordered layer have a certain preferential orientation. This orientational correlation dependence with time was explained by the slow process called as "reorientations mediated by translational displacements (RMTD)". Relaxation by this mechanism is the combined consequence of the molecular dynamics appropriate to the mesophases, tempered by the structure of the confining medium. The orientation correlation function and spectral density expressions for RMTD were derived by Kimmich *et al.* [50]. The RMTD process is described by the probability density that a molecule is displaced by a distance $r$ in a time interval $t$, and by the probability that it alters the orientation from $\Omega_i$ to $\Omega_f$ in that distance $r$. The probability density can be expressed as

$$P\left(\Omega_i, \Omega_f, t\right) = \int \phi\left(\Omega_i, \Omega_f, r\right) \psi(r,t) d^z r \qquad (2.75)$$

where the integration is carried out over the whole topologically $z$-dimensional space ($z$ = 1, 2, or 3). $\psi(r,t)$ is the diffusion profile and $\phi\left(\Omega_i, \Omega_f, r\right)$ represents the probability density that the orientation changes from $\Omega_i$ to $\Omega_f$ in a distance $r$.

The orientation correlation function in terms of spherical harmonics is expressed as

$$G(t) = \frac{1}{\langle |Y_2^{(m)}|^2 \rangle} \int g_{2,m}(r) \psi(r,t) d^z r. \qquad (2.76)$$

Here $g_{2,m}(r)$ is the surface correlation function. The diffusion profile depends on the dimensionality $z$ and the validity of Einstein relation for normal diffusion. The probability density for the displacement $r$ in time $t$ for normal diffusion has the Gaussian form and can be analyzed in terms of modes with wave numbers $q$. The orientation correlation function for normal diffusion can then be written as

$$G(t) = \int_0^\infty Q(q) e^{-Dtq^2} dq. \tag{2.77}$$

where $Q(q)$ is the orientational structure factor and it depends on the structure of confining matrix. Thus the spatial correlation of the surface affects the reorientational time correlation of the diffusing anisotropic molecules near the surface.

The corresponding spectral density for RMTD is given by

$$J_k(\omega) = \int_0^\infty G_k(t) \cos(\omega t) dt = \int_0^\infty Q(q) \frac{2\tau_q}{1 + \omega^2 \tau_q^2} dq. \tag{2.78}$$

In the case of confined liquid crystal systems the spin-lattice relaxation contribution from the RMTD mechanism can be incorporated by using the two-phase fast-exchange model [51, 52]. Here we consider the confined mesogenic fluid to coexist in two phases, where the first phase consists of molecules in the surface layer with restricted tumbling (order parameter $S \neq 0$) and the second one of the bulk-like molecules with $S = 0$ (in the isotropic phase). The condition of fast exchange is fulfilled if the molecular exchange between the two phases, and between different positions or orientations within the ordered phase, takes place on a time which is very much shorter than the spin-lattice relaxation time. This condition imparts a single relaxation time of the system and is experimentally indicated by mono-exponential relaxation curves. Within the framework of two-phase fast-exchange model, there are four different situations to be distinguished and to be characterized by

the relative fractions of molecules being initially and finally in one of the two possible states (the surface layer or the bulk-like phase): $p_{s,s}(t)$ is the fraction of molecules initially and finally in the surface layer; $p_{s,b}(t)$ is the fraction of molecules initially in the surface layer and finally in the bulk-like phase; $p_{b,s}(t)$ is the fraction of molecules initially in the bulk-like phase and finally in the surface layer; $p_{b,b}(t)$ is the fraction of molecules initially and finally in the in the bulk-like phase. These fractions are normalized of course,

$$p_{s,s}(t) + p_{s,b}(t) + p_{b,s}(t) + p_{b,b}(t) = 1. \tag{2.79}$$

The total correlation function can then be analyzed into four partial correlation functions:

$$\begin{aligned} G_k(t) &= p_{s,s}(t)\langle Y_{2,k}(0)Y_{2,-k}(t)\rangle_{RMTD,RR} + p_{s,b}(t)\langle Y_{2,k}(0)Y_{2,-k}(t)\rangle_{EX,IR} \\ &+ p_{b,s}(t)\langle Y_{2,k}(0)Y_{2,-k}(t)\rangle_{IR} + p_{b,b}(t)\langle Y_{2,k}(0)Y_{2,-k}(t)\rangle_{IR}. \end{aligned} \tag{2.80}$$

The subscripts RMTD, RR, EX., and IR, stand for reorientations mediated by translational displacements and restricted reorientations of the molecules in the surface layer, molecular exchange and isotropic reorientations in the bulk-like phase, respectively. The correlation functions of the molecules that are at the beginning in one phase and at the end in the other phase are usually neglected [52–54]. Then the correlation function is described by two partial correlation functions, given by [54]

$$G_k(t) = P_{s,s}(t)G_k(t)_{RMTD,RR} + P_{b,b}(t)G_k(t)_{IR}. \tag{2.81}$$

Here $P_{s,s}(t)$ is the conditional probability that a molecule is initially and finally in the surface layer and $P_{b,b}(t)$ is the conditional probability that a molecule is initially and finally in the bulk-like phase. Using rate equations for the molecular populations in each phase, the conditions probability is calculated as [53]

$$P_{s,s}(t) = p_s(1-p_s)e^{\frac{-t}{\tau_{EX}}} + p_s^2 \tag{2.82}$$

$$P_{b,b}(t) = p_s(1-p_s)e^{\frac{-t}{\tau_{EX}}} + (1-p_s)^2 \tag{2.83}$$

where $\tau_{EX}$ denotes the exchange time of molecules between the surface and bulk-like phase, and $p_s$ stands for the fraction of molecules in the surface layer. The translational diffusion within the ordered layer and its thickness determine the exchange time of molecules.

In describing the time dependence of the correlation functions we take into account the fact that fast molecular reorientations and the much slower RMTD processes are virtually independent of each other. The total correlation function is then simplified as [54]

$$\begin{aligned} G_k(t) &= \left[p_s(1-p_s)e^{\frac{-t}{\tau_{EX}}} + p_s^2\right]\left[(1-S^2)e^{\frac{-t}{\tau_{RR}}} + S^2\right]e^{\frac{-t}{\tau_{RMTD}}} \\ &+ \left[p_s(1-p_s)e^{\frac{-t}{\tau_{EX}}} + (1-p_s)^2\right]e^{\frac{-t}{\tau_{RR}}}. \end{aligned} \tag{2.84}$$

Here $\tau_{RMTD}$ is the decay constant of the RMTD correlation and $S^2$ the square of the order parameter that represents the residual correlation of restricted tumbling in the long time limit, *i.e.*, before the exchange process and RMTD become effective. Since local molecular reorientations [LR], either isotropic or restricted due to local ordering, are much faster than the exchange and RMTD, these contributions persist in expressions like

$$\frac{1}{\tau_{RMTD}} + \frac{1}{\tau_{RR}} \approx \frac{1}{\tau_{RR}}$$

or

$$\frac{1}{\tau_{EX}} + \frac{1}{\tau_{IR}} \approx \frac{1}{\tau_{IR}}.$$

The spectral density functions $J_k(\omega)$ derived from equations (2.78) and (2.84), assume therefore a relatively simple form:

$$J_k(\omega) = J_k(\omega)_{LR} + J_k(\omega)_{EX,RMTD} \tag{2.85}$$

with

$$J_k(\omega)_{LR} = p_s(1-s^2)\frac{2\tau_{RR}}{1+\omega^2\tau_{RR}^2} + (1-p_s)\frac{2\tau_{IR}}{1+\omega^2\tau_{IR}^2} \tag{2.86}$$

$$J_k(\omega)_{EX,RMTD} = p_s(1-p_s)S^2\frac{2\tau}{1+\omega^2\tau^2} + p_s^2S^2\frac{2\tau_{RMTD}}{1+\omega^2\tau_{RMTD}^2} \tag{2.87}$$

where $\tau = (1/\tau_{RMTD} + 1/\tau_{EX})^{-1}$ and $J_k(\omega) = J_1(\omega) = J_2(\omega)$.

The description of the RMTD process with a single correlation time is often an oversimplification. The spin-relaxing capability of this process depends on the structure of the surface, *i.e.*, on the so-called surface structure factor. The surface effect is analyzed by a spatial Fourier transformation in terms of modes with wave numbers $q$ in the interval between $q_{min}$ and $q_{max}$. The correlation function for the diffusion mode with the wave number $q$ is assumed to be exponential with the decay time $\tau_q = (Dq^2)^{-1}$. Following the approach of Kimmich used in different porous media [51, 55] and assuming that in the range between $q_{min}$ and $q_{max}$ all the modes are equally weighted, the spectral density $J_k(\omega)_{EX,RMTD}$ becomes

$$\begin{aligned} J_k(\omega)_{EX,RMTD} &= \frac{p_s(1-p_s)S^2}{\Delta q}\int_{q_{min}}^{q_{max}}\frac{2\left(1/\tau_q + 1/\tau_{EX}\right)^{-1}}{1+\omega^2(1/\tau_q+1/\tau_{EX})^{-2}}dq \\ &+ \frac{p_s^2S^2}{\Delta q}\int_{q_{min}}^{q_{max}}\frac{2\tau_q}{1+\omega^2\tau_q^2}dq. \end{aligned} \tag{2.88}$$

Here $\Delta q = q_{max} - q_{min}$. A closed form of equation (2.88) can be obtained in the limits $\tau_q \ll \tau_{EX}$ and $\tau_q \gg \tau_{EX}$ with the crossover between the two regimes centered at $q_c = (D\tau_{EX})^{-1/2}$. When the RMTD is much faster than the exchange process and does not leave any residual correlation, the two terms in equation (2.88) merge into a single one, which is governed by the RMTD mechanism:

$$J_k(\omega)_{EX,RMTD} \quad \rightarrow J_k(\omega)_{RMTD} = \frac{\sqrt{2}p_s S^2}{\Delta q\sqrt{D}}\omega^{-1/2}\Big[f\left(\frac{\omega_{RMTDmax}}{\omega}\right) - f\left(\frac{\omega_{RMTDmin}}{\omega}\right)\Big] \tag{2.89}$$

where

$$f(w) = \arctan\left(\sqrt{2w}+1\right) + \arctan\left(\sqrt{2w}-1\right) + arc\tanh\left(\frac{\sqrt{2w}}{w+1}\right). \tag{2.90}$$

Here $\omega_{RMTDmin} = Dq_{min}^2$ , $\omega_{RMTDmax} = Dq_{max}^2$.

The linear dependence on $p_s$ is characteristic for systems where the RMTD correlation function decays to zero before the molecules emerge from the ordered into the isotropic phase. In the opposite case, *i.e.*, in the limit of fast molecular exchange compared to the RMTD modulation, equation (2.88) transforms to

$$J_k(\omega)_{EX,RMTD} \approx p_s(1-p_s)S^2\frac{2\tau_{EX}}{1+\omega^2\tau_{EX}^2} + \frac{\sqrt{2}p_s^2S^2}{\Delta q\sqrt{D}}\omega^{-1/2}\left[f\left(\frac{\omega_{RMTDmax}}{\omega}\right)-f\left(\frac{\omega_{RMTDmin}}{\omega}\right)\right]. \quad (2.91)$$

The RMTD term is here identical to that of equation (2.89) apart from the prefactor $p_s^2$ which appears in the expression when a molecule, being initially in the surface layer, makes several excursions into the bulk-like phase before ending at time $t$ in the surface layer again. The RMTD spectral density functions in the range between $\omega_{RMTDmin}$ and $\omega_{RMTDmax}$ is proportional to $\omega^{-1/2}$ as shown by equations (2.89) and (2.91). The low frequency cutoff $\omega_{RMTDmin}$ determines the turning point where $J_k(\omega)_{RMTD}$ levels off into a plateau, independent of $\omega$ and proportional to $D^{-1}$:

$$J_k(\omega\rightarrow 0)_{RMTD} = \frac{2g(p_s)S^2l_{min}l_{max}}{\pi^2}D^{-1}. \quad (2.92)$$

Here $g(p_s)$ is a function depending on the relation between $\tau_{EX}$ and $\tau_q$, and $l_{min} = \pi/q_{max}$ and $l_{max} = \pi/q_{min}$ determine the smallest and largest curvilinear displacements where a notable change in the orientation of the surface director is attained and these length scales are dependent on the dimensionality of the pores. A third dispersion regime occurs at frequencies above $\omega_{RMTDmax}$, where the slope of the dispersion curve becomes steeper and proportional to $\omega^{-2}$. The spectral density in this range is given by

$$J_k(\omega\rightarrow\infty)_{RMTD} \approx \frac{2g(p_s)S^2D\pi^2}{3l_{min}^2}\omega^{-2}. \quad (2.93)$$

It should be stressed that the characteristic $J_k(\omega)_{RMTD} \propto \omega^{-1/2}$ behavior in the middle range of the dispersion regime depends on the weight factors ascribed to the contributions of modes with different wave numbers $q$. When

surface orientational structure factor is constant then the relaxation rate of RMTD is given by [54, 56]

$$\begin{aligned}\frac{1}{T_{1RMTD}} &= A_{RMTD}\Big\{\frac{1}{\omega^{1/2}}\Big[f\left(\frac{\omega_{RMTDmax}}{\omega}\right)-f\left(\frac{\omega_{RMTDmin}}{\omega}\right)\Big] \\ &+ \frac{4}{(2\omega)^{1/2}}\Big[f\left(\frac{\omega_{RMTDmax}}{2\omega}\right)-f\left(\frac{\omega_{RMTDmin}}{2\omega}\right)\Big]\Big\}. \end{aligned} \quad (2.94)$$

The prefactor $A_{RMTD}$ depends on the residual dipole-dipole proton spin interaction, diffusion coefficient and on the micro structural features of the confined liquid crystal.

In general the orientational structure factor is a complex function of the wave number $q$. In some cases it can be approximated by the analytical form [55]

$$Q(q) = cq^{-\chi} + e. \quad (2.95)$$

Here $c$ and $e$ are constants independent of the wave number $q$. The constant $e$ can be neglected in the low frequency dispersion regime and inserting equation (2.95) into equation (2.78) and using the expression $\tau_q = (Dq^2)^{-1}$, the spectral density $J_k(\omega)_{RMTD}$ is written as [56]

$$J_k(\omega)_{RMTD} \propto \int_{q_{min}}^{q_{max}} \frac{2\tau_q q^{-\chi}}{1+\omega^2\tau_q^2}dq = \frac{2}{D}\int_{q_{min}}^{q_{max}} \frac{q^{2-\chi}}{q^4+\left(\frac{\omega}{D}\right)^2}dq. \quad (2.96)$$

Replacing $q\sqrt{D/\omega}$ by $z$ yields

$$\frac{1}{T_{IRMTD}} = A_{RMTD}\left\{\frac{1}{\omega^p}\int_{z_{min}}^{z_{max}} \frac{z^{3-2p}}{1+z^4}dz + \frac{1}{(2\omega)^p}\int_{z_{min}}^{z_{max}} \frac{z^{3-2p}}{1+z^4}dz\right\} \quad (2.97)$$

with $p = (1 + \chi)/2$, $z_{max} = \left(\frac{\omega_{RMTDmax}}{\omega}\right)^{1/2}$, $z_{min} = \left(\frac{\omega_{RMTDmin}}{\omega}\right)^{1/2}$.

The integration in equation (2.97) can be performed analytically for $\chi \neq 0$ by extending the limits of integration from zero to infinity. The resulting $T_{1RMTD}^{-1}$ dispersion curve is directly related to $\chi$ and follows the power law, $T_{1RMTD}^{-1} \propto \omega^{-p}$ [56].

# References

[1] A. Abragam, *The Principles of Nuclear Magnetism*, Clarendon Press, Oxford (1961).

[2] C. P. Slichter, *Principles of Magnetic Resonance*, Springer-Verlag, Berlin (1996).

[3] R. Y. Dong, *Nuclear Magnetic Resonance of Liquid Crystals*, Springer-Verlag, New York (1997).

[4] R. Kimmich, *NMR Tomography, Diffusometry, Relaxometry*, Springer-Verlag, Berlin (1997).

[5] R. Y. Dong, *Nuclear Magnetic Resonance spectroscopy of Liquid Crystals*, World Scientific, Singapore (2009).

[6] Malcom H. Levitt, *Spin Dynamics: Basics of Nuclear Magnetic Resonance*, John Wiley sons Ltd. (2005).

[7] N. Bloembergen, E.M. Purcell, and R.V. Pound, Phys. Rev. **73**, 679 (1948).

[8] M. Goldman, *Spin temperature and Nuclear Magnetic Resonance in solids*, Oxford, England **51**, (1970).

[9] D. Wolf, *Spin temperature and Nuclear Spin Lattice Relaxation in matter*, Clarendon Press, Oxford (1979).

[10] R. K. Wangsness and F. Bloch, Phys. Rev. **89**, 72, (1953).

[11] A. G. Redfield, Adv. Magn. Reson. **1**, 1 (1965).

[12] R. J. C. Brown, H. S. Gutowsky, and K. Shimomura, J. Chem. Phys. **38**, 76 (1963).

[13] D. K. Green and J. G. Powles, Proc. Phys. Soc. **85**, 87 (1965).

[14] P. S. Hubbard, Phys. Rev. **131**, 1155 (1963).

[15] S. Chandrasekar, Rev. Mod. Phys. **15**, 1 (1943).

[16] G. J. Kruger, Phys. Rep. **82**, 229 (1982).

[17] R. Y. Dong, Israel J. Chem. **23**, 370 (1983).

[18] C. G. Wade, Annu. Rev. Phys. Chem. **28**, 47 (1977).

[19] H. C. Torrey, Phys. Rev. **92**, 962 (1953).

[20] S. Zumer and M. Vilfan, Phys. Rev. A **17**, 424 (1978).

[21] C. K. Yun, and A.G. Frederickson, Mol. Cryst. Liq. Cryst. **12**, 73 (1970).

[22] G. J. Kruger, and H. Spiesecke, Z. Naturforsch **28a**, 964 (1973).

[23] I. Zupancic, I. Pirs, R. Blinc, and J. W. Doane, Sol. State Commun. **15**, 227 (1974).

[24] J. F. Harmon and B. N. Muller, Phys. Rev. **182**, 400 (1969).

[25] M. Vilfan and S. Zumer , Phys. Rev. A **21**, 672 (1980).

[26] R. Blinc ,M. Vilfan, M. Luzar, J. Seliger and V. Zagar, J. Chem. Phys. **68**, 303 (1978).

[27] J. Seliger, R. Oresedkar, V. Zagar, and R. Blinc, Phys. Rev. Lett. **38**, 411 (1977).

[28] P. G. de Gennes, *The Physics of Liquid Crystals*, Oxford University, New York (1974).

[29] J. H. Freed, J. Chem. Phys. **66**, 4183 (1977).

[30] R. Blinc, D. L. Hogenboom , D. E. O Reilly, and E. M. Peterson, Phys. Rev. Lett. **23**, 969 (1969).

[31] B. Cabane, Adv. Mol. Relaxation Processes. **3**, 341 (1972).

[32] S. K. Ghosh, E. Tettamanti and A. Panatta, Phys. Rev. B **21**, 1194 (1980).

[33] T. W. Stinson III and J. D. Litster, Phys. Rev. Lett. **25**, 503 (1970).

[34] T. W. Stinson III and J. D. Litster, Phys. Rev. Lett. **30**, 688 (1973).

[35] F. V. Chavez, F. Bonetto and D. J. Pusiol, Chem. Phys. Lett. **330**, 368 (2000).

[36] R. Blinc, *NMR basic principles and progress*, ed., Pintar M.M., **13**, 97 (1976).

[37] P. Pincus, Solid State Commun. **7**, 415 (1969).

[38] J. W. Doane, and D. L. Johnson, Chem. Phys. Lett. **6**, 291 (1970).

[39] F. Brochard, J. Phys. (Paris) **34**, 411 (1973).

[40] R. Blinc, M. Luzar, M. Vilfan. and M. Burgar, J. Chem. Phys. **63**, 3445 (1975).

[41] R. R. Vold and R. L. Vold, J. Chem. Phys. **88**, 4655 (1988).

[42] R. R. Vold and R. L. Vold, *The Molecular Dynamics in Liquid Crystals*, edited by G.R. Luckhurst and C.A. Veracini, Kluver Academic Publishers, London (1994) p. 207, and the references therein.

[43] J. Struppe and F. Noack, Liq. Cryst. **20**, 595 (1996).

[44] K. Venu and V. S. S. Sastry, Solid State Phys. (India), **42**, 15 (2000).

[45] V. Satheesh, Ph.D. Thesis, University of Hyderabad (2000).

[46] B. V. N. Phani Kumar, Ph.D. Thesis, University of Hyderabad (2003).

[47] P. J. Sebastiao, M. H. Godihno, A. C. Ribeiro, D. Guillon, and M. Vilfan, Liq. Cryst. **11**, 621 (1992).

[48] P. J. Sebastiao, A. C. Ribeiro, H. T. Nguyen, and F. Noack, Z. Naturforsch. Teil A **48**, 851 (1993).

[49] P. J. Sebastiao, A. C. Ribeiro, H. T. Nguyen, and F. Noack, J. Phys. II France **5**, 1707 (1995).

[50] R. Kimmich, and H. W. Weber, Phys. Rev. B **47**, 11788 (1993) .

[51] R. Kimmich, E. Anoardo, Prog. Nucl. Magn. Reson. Spectrosc. **44**, 257 (2004).

[52] E. Anoardo, F. Grinberg, M. Vilfan, and R. Kimmich, Chem. Phys. **297**, 99 (2004).

[53] E. E. Burnell, M .E. Clark, J. A. M. Hinke, and N. R. Cahpman, Biophys. J. **33**, 1 (1981).

[54] P. J. Sebastiao, D. Sousa, A. C. Ribeiro, M. Vilfan, G. Lahajnar, J. Seliger, and S. Zumer, Phys. Rev. E **72**, 061702 (2005).

[55] S. Stapf, R. Kimmich, and J. Neiss, J. Appl. Phys. **75**, 529 (1994).

[56] M. Vilfan, T. Apih, P. J. Sebastiao, G. Lahajnar, and S. Zumer, Phys. Rev. E **76**, 051708 (2007).

# 3

# Experimental Details of Pulsed and Field-Cycling NMR Relaxometers

In this chapter the experimental arrangement to measure nuclear spin relaxation times, as a function of Larmor frequency and temperature is discussed. This includes the generation of resonant *rf* pulse sequences, detection of magnetization decays, and data acquisition for subsequent processing. The work presented in this thesis was carried out on the commercial fast field-cycling spectrometer (Stelar Spinmaster FFC 2000, Italy) in the frequency range of 10 kHz to 10 MHz, and on a variable field pulsed NMR spectrometer to cover the high frequencies from 10 MHz to 50 MHz. We first discuss the methodology of such measurements on pulsed NMR spectrometers, introducing in the process different *rf* pulse sequences and their relative merits. We follow it up with a discussion on the working principle of the more recent field-cycling NMR technique, to access very low resonance fields ($\sim$ 10 kHz), over coming the instrumentation limitation normally encountered at such low frequencies. Finally, we present the specifications of the spectrometers used for the present work.

## 3.1 Pulsed NMR methodology

A nuclear magnetic moment $\boldsymbol{\mu}$ (arising due to a spin $I$ and the gyromagnetic ratio $\gamma = \mu/I$), in the presence of an external Zeeman magnetic field $\mathbf{H_0}$, experiences a torque equal to the rate of change of angular momentum. The equation of motion can be written as [1, 2],

$$\frac{d\boldsymbol{\mu}}{dt} = \gamma(\boldsymbol{\mu} \times \mathbf{H_0}). \tag{3.1}$$

Representing the total magnetization $\sum \boldsymbol{\mu}_i$ of the system by $\mathbf{M}$ the equation of motion of the total macroscopic magnetization becomes,

$$\frac{d\mathbf{M}}{dt} = \gamma(\mathbf{M} \times \mathbf{H_0}). \tag{3.2}$$

Application of a small time dependent *rf* field $\mathbf{H_1(t)}$ with a frequency $\omega$ to perturb the quantizing static field $\mathbf{H_0}$, in a plane perpendicular to $\mathbf{H_0}$, modifies the equation 3.2 as,

$$\frac{d\mathbf{M}}{dt} = \gamma\mathbf{M} \times [\mathbf{H_0} + \mathbf{H_1}(t)]\,. \tag{3.3}$$

Transforming into a rotating co-ordinate system having an angular frequency ($\omega$) as that of the perturbing field ($\mathbf{H_1(t)}$) and moving about an axis parallel to $\mathbf{H_0}$ (say the $z$-axis), the equation of motion of the magnetization in the new co-ordinate system with an effective field $\mathbf{H_{eff}}$ becomes,

$$\frac{\partial\mathbf{M}}{\partial t}\Big|_{rot} = \gamma\mathbf{M} \times \mathbf{H_{eff}} \tag{3.4}$$

where

$$\mathbf{H_{eff}} = [(\mathbf{H_0} + \boldsymbol{\omega}/\gamma) + \mathbf{H_1(t)}]\,.$$

It can be seen that the magnetization that was initially parallel to the quantizing static field $\mathbf{H_0}$ (along, say, the $z$-direction) precesses about $\mathbf{H_1(t)}$

in the $y$-$z$ plane under the condition of resonance ($\omega = \omega_0 = -\gamma H_0$). If $\mathbf{H_1}$ is applied for a time interval $t_w$ ($rf$ pulse) the angle of the precessing cone is given by $\theta = \gamma H_1 t_w$. For a given $\mathbf{H_1}$ if the magnetization is rotated through $\theta = 180^0$ it is called a $\pi$ pulse and if it is rotated through $\theta = 90^0$ is called a $\pi/2$ pulse.

Bloch's phenomenological equations [1, 3] depict the time evolution of the macroscopic magnetization ($\mathbf{M}$) in the presence of applied fields and the relaxation processes to be discussed. They introduce the spin-lattice relaxation time ($T_1$) and the spin-spin relaxation time ($T_2$), for different magnetization components, expressed as

$$\frac{dM_z}{dt} = \gamma(M \times H)_z + \frac{M_0 - M_z}{T_1} \tag{3.5a}$$

$$\frac{dM_x}{dt} = \gamma(M \times H)_x - \frac{M_x}{T_2} \tag{3.5b}$$

$$\frac{dM_y}{dt} = \gamma(M \times H)_y - \frac{M_y}{T_2}. \tag{3.5c}$$

The spin-lattice relaxation time ($T_1$) is the characteristic time associated with the dissipation of the differential energy of the spin system (relative to equilibrium) to the lattice (all the degrees of freedom other than the spin degrees of freedom) which is an irreversible process, and hence involves a change in the entropy of the spin system, whereas $T_2$ is the time constant associated with the processes reaching internal equilibrium with the ensemble of spins. After a $\pi/2$ pulse the magnetization $\mathbf{M}$ is flipped into the $x$-$y$ plane (Figure 3.5). This corresponds to a non-equilibrium condition of the spin system since at equilibrium the net magnetization in the $x$-$y$ plane should be zero. The spin system loses this coherence energy in the $x$-$y$ plane (Figure 3.5) in a characteristic time identified as the spin-spin relaxation time ($T_2$) associated with this reversible process and involves no change in the net entropy of the system. Hence $T_1$ will normally be greater than $T_2$.

The decay of the excess magnetization in the $xy$-plane to equilibrium called the free induction decay (FID), is recorded as an observable *emf* induced in a pick up coil due to the time dependent magnetization. Normally the same induction coil is used for both creating a non-equilibrium condition of the spin system (by the application of pulsed *rf*) and subsequently detecting the FID. A typical FID for a Lorentzian resonance line would be an exponentially decaying sinusoid. The rate of decay of the FID depends not only on the spin-spin relaxation time ($T_2$) but also on the broadening caused by the Zeeman field inhomogeneity as well as possible inhomogeneities in the sample. Thus the time constant determined from the FID, denoted by $T_2^*$ (apparent $T_2$), is shorter than $T_2$.

## 3.2 High field pulsed NMR spectrometer

A variable frequency high field pulsed NMR spectrometer used for relaxation time measurements (in the frequency range of 10-50 MHz) is home-built and available in our laboratory. The details of this spectrometer are briefly discussed in this section. The magnet used is manufactured by Bruker Spectrospin (Model BE25) and is energized using a power supply (Bruker, Model No. B-MN 155/45 A6). The pole caps are $10''$ in diameter and the pole gap is adjustable upto $4''$. The magnet has a stability of 1 part in $10^6$ with a very good homogeneity over a sample of about 1 $cm^3$. A maximum magnetic field of about 1.5 T with long term stability could be obtained with good cooling arrangements.

The high field pulsed NMR spectrometer broadly consists of three units (i) a transmitter (ii) a matching network or probe and (iii) a receiver. The block diagram is given in Figure 3.1. The transmitter generates appropriate pulsed *rf* radiation, amplifies and delivers it to the matching network (probe). The probe consists of passive elements including the sample coil. At resonance

the applied voltage is multiplied to several fold and the nuclei are subjected to a high value of *rf* field. The receiver picks up the weak signal from the NMR coil and amplifies it in stages. This amplified signal is detected by the phase sensitive detector and processed through a low pass filter and a video amplifier. Finally a signal averager is used to improve the signal-to-noise (S/N) ratio. Here we employed an automated NMR hardware, (Spinmaster from Stelar, Italy) to take care of all *rf* operations. Spinmaster encapsulates transmitter and receiver parts of the NMR spectrometer into a single console. It consists of RF, Digital unit and power supply.

### 3.2.1 RF and Digital units

The latest generation of direct digital synthesizers (DDS), programmable logic and fast A/D and D/A converters are implemented in the RF electronics of Spinmaster. The unit operates in the 2 to 80 MHz band and all pertinent settings are under digital control. The RF and digital unit further consist of: 1. Direct digital synthesizer (DDS) *rf* unit; 2. RF power transmitter; 3. RF receiver unit; 4. Acquisition Manager (AQM).

The direct digital synthesizer (DDS) *rf* unit consists of (i) clock generator (ii) DDS controlled- frequency and phase control unit and (iii) *rf* and pulse modulator. The clock generator sends a sinusoidal reference signal at 80 MHz as output. This clock output is divided by a factor of 2 and the resultant 40 MHz clock output is available for Acquisition Manager. The DDS controller is used to control the system frequency and phase difference between two channels. RF and pulse modulator produce the pulsed *rf* output which is to be fed to the transmitter. The level of this pulsed *rf* output can be varied from 0.25 V to 2.5 V.

The RF power transmitter of Spinmaster delivers power up to 300W in the pulse mode. The maximum power level can be adjusted through the Acq. NMR software. The receiver amplifies the *emf* induced by the nuclear mag-

netization from its initial level (of order of a microvolt) to the level required for data handling and display (of order volts). In the process, the nuclear signal is demodulated (*i.e.*, the *rf* frequency removed) by an appropriate detector (normally a phase-sensitive detector). The receiver is capable of withstanding overloaded voltages and also recovers fast from these overload voltages (due to leakages during pulse ON periods). This is a quadrature receiver with an additional diode detection channel and programmable amplifier filters.

Acquisition manager (AQM) is the heart of the Spinmaster. It is connected to a standard PC parallel port which transmits logical commands called interface primitives. It has an in built CPU (Z180) which decodes the instructions into a set of commands to be sent to the hardware interface at planned time intervals. Furthermore, this CPU reports the current status of the hardware and of the experiment to the PC, programs the hard ware units through a proprietary parallel, bi-directional 8-bit bus (Stelar bus) and sends the acquired data to the host PC. At boot time, the Z180 executes a configuration routine and establishes communication with the PC. In practice, the time-critical instructions are executed by the pulser, which are loaded by the Z180. The host may stop/start the Z180 and the flow of instructions under its control, but the AQM executes the instructions related to configuration and sequence independently.

### 3.2.2 Probe

The probe or the matching network which houses the sample coil plays an important role in the performance of the spectrometer. An ideal probe must effectively couple the sample coil to the transmitter during pulse ON time and to the receiver during pulse OFF time for signal detection. It should also decouple the receiver from the transmitter during the pulse ON period. For the present experiments we used a single-coil probe. The single-coil probe arrangement is simpler and has many advantages and some disadvantages

with respect to the crossed-coil probe. Probably the main advantage of the single-coil is its much higher power efficiency since the coil can be tightly wound around the sample, in contrast to the crossed coil probe in which the transmitter coil must be considerably larger and adjusted for minimum coupling to the receiver coil. Probe is tuned to the desired frequency by adjusting tuning and matching capacitors. If the probe is not properly tuned and/or matched, *rf* power is not optimally transferred, thus lengthening the $90^o$ pulse width and worsening S/N ratio. Tuning a probe is obviously necessary when a different nucleus is to be observed. Not so obviously, it is often necessary after changing the sample. This is due to the sample's *rf*-properties. To tune a probe, directional coupler is used as an impedance sensor, and the output is displayed on a dip meter.

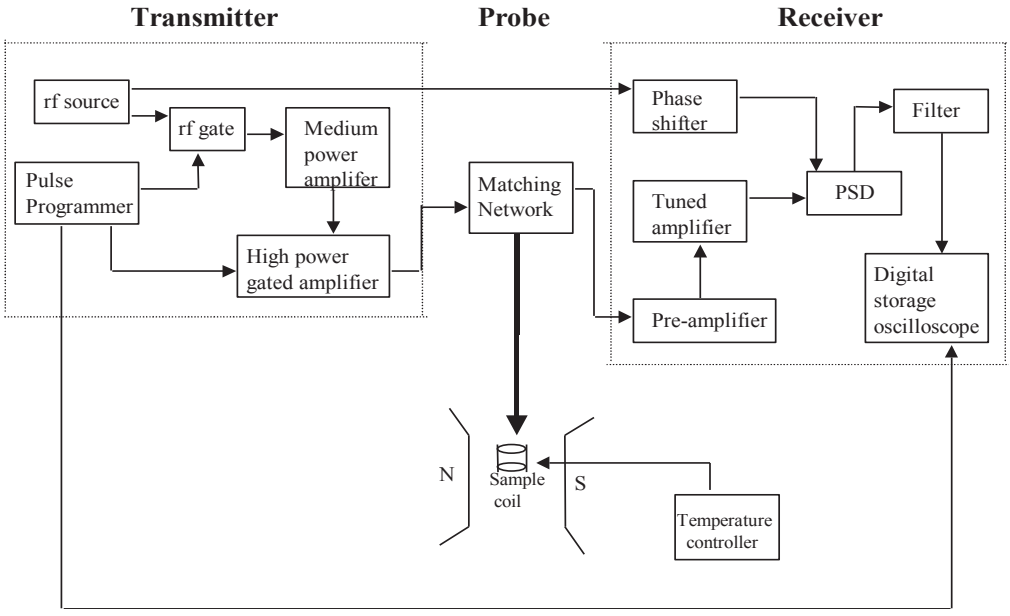


Figure 3.1: Block diagram of a high field pulsed NMR spectrometer.

## 3.3 Pulse sequences for spin-lattice and spin-spin relaxation times $T_1$ and $T_2$

To measure various relaxation times ($T_1$ and $T_2$), different pulse sequences, corresponding to the different initial non-equilibrium conditions required to be created, are necessary. The details of such pulse sequences used in the present studies are given below [4].

### 3.3.1 $T_1$ Measurements

#### 3.3.1.1 Saturation recovery sequence ($\pi/2 - \tau - \pi/2$)

This sequence consists of a $\pi/2$ pulse followed by another $\pi/2$ pulse after a variable delay $\tau$. The first $\pi/2$ pulse tilts the magnetization into the $xy$ plane (magnetization along the $z$-direction is made zero), which is then allowed to evolve for a time $\tau$. The evolved magnetization is then sampled by a second $\pi/2$ pulse which tilts whatever magnetization that is developed along the $z$-axis into the $xy$ plane for observation. The amplitude of the FID, $M(\tau)$ at a fixed time from the sampling pulse develops from zero at time $\tau = 0$ to $M_0$ at time $\tau = \infty$ and satisfies the following equation

$$M_z(\tau) = M_0 \left[1 - \exp(-\tau/T_1)\right]. \tag{3.6}$$

By repeating the experiment for different values of $\tau$ and then fitting the data to equation (3.6), by a least square fitting procedure, $T_1$ is obtained. Typical magnetization recovery in the presence of this sequence is shown in Figure 3.2.

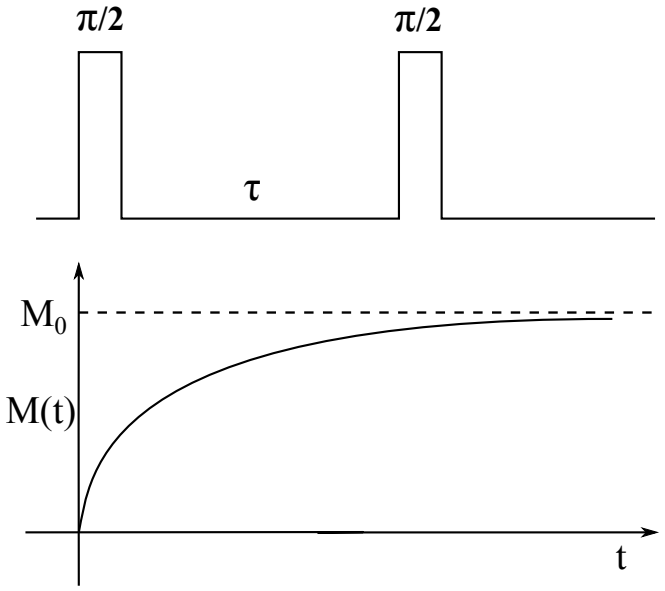


Figure 3.2: Saturation recovery for $T_1$ measurements.

#### 3.3.1.2 Inversion recovery sequence ($\pi - \tau - \pi/2$)

In this sequence the first $\pi$ pulse tilts the equilibrium magnetization along the $z$-direction into the negative $z$ direction and the evolution is monitored along the $z$-axis by another sampling $\pi/2$ $rf$ pulse after a time $\tau$ [4, 5]. The magnetization recovery from -$M_0$ to $M_0$ follows the equation, (Figure 3.3)

$$M_z(t) = M_0 \left[1 - 2\exp(-\tau/T_1)\right]. \qquad (3.7)$$

$M_0$ is the amplitude of the FID after a time $\tau = \infty$. A least square fitting of the data to equation (3.7) gives the spin-lattice relaxation time $T_1$.

The advantages of this method over saturation recovery sequence are:

(i) $T_1$ can be roughly estimated initially by finding time $\tau_0$ for which the magnetization is zero, as $T_1 = \tau_0/ln2$.

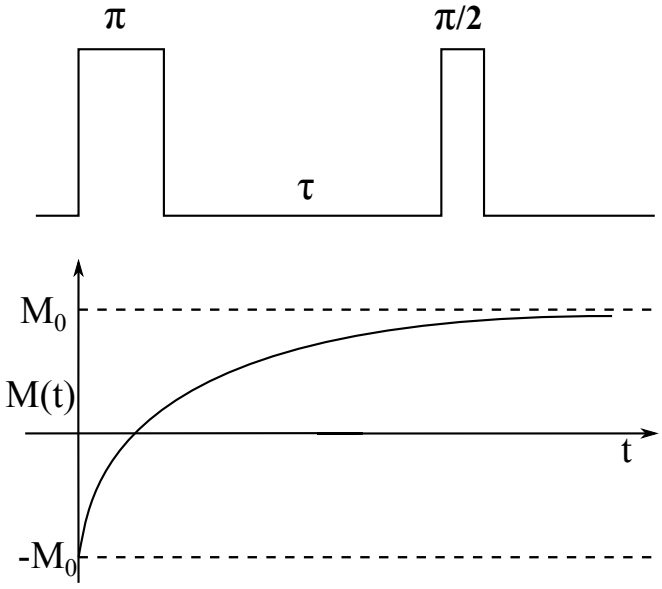


Figure 3.3: Inversion recovery sequence for $T_1$ measurements.

(ii) The data has twice the dynamic range (-$M_0$ to $M_0$) as compared to the saturation recovery sequence (0 to $M_0$), hence increasing the apparent signal-to-noise ratio.

The disadvantage of this method over saturation recovery is that it is time consuming because this sequence starts with an initial equilibrium magnetization in the negative $z$-direction and the magnetization has to evolve to the positive $z$-direction before repeating the sequence. It takes a mimimum of $5T_1$ times to fully recover the magnetization before repeating the sequence and this will involve considerable experimentation time if $T_1$ is of the order few hundred milliseconds (which is the case with typical LC system at normal Larmor frequencies).

One disadvantage of using any of the two methods is that, if the initial preparatory pulse width ($\pi$ or $\pi/2$) is not set properly or if $H_1$ is not homogeneous, the initial condition of the magnetization (-$M_0$ or zero, respectively) is not met and hence leading to a reduction in the signal strength.

#### 3.3.1.3 Saturation burst sequence

This sequence is an improved version of the saturation recovery sequence, where the initial preparatory $\pi/2$ pulse is replaced by a closely spaced burst (usually 5 to 10) of $\pi/2$ pulses which is followed by a sampling $\pi/2$ pulse after a variable time, $\tau$. The spacing between two $\pi/2$ pulses in the burst ($\tau$) is chosen such that the $T_2$ process is complete but $T_1$ process has not effectively taken place (*i.e.*, $T_2 < \tau \ll T_1$) (Figure 3.4). The advantage of using this sequence is that the burst ensures the zeroing of magnetization, even if the pulse width is not exactly set to $\pi/2$ or if $H_1$ is slightly inhomogeneous. The evolution of the magnetization in this pulse sequence is given by equation (3.6). The other advantage of using this method is that the long waiting times ($5T_1$) for long $T_1$ measurements is eliminated as there is no need for allowing the magnetization to recover fully before the sequence is repeated. In this sequence the first pulse of the next burst can act as a sampling pulse.

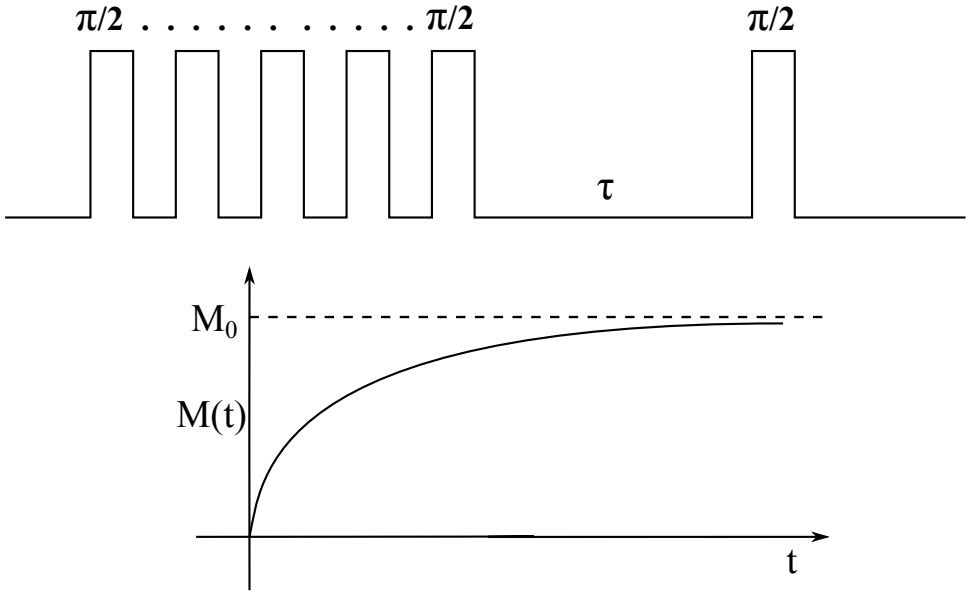


Figure 3.4: Saturation burst sequence for $T_1$ measurements.

## 3.3.2 $T_2$ Measurements

### 3.3.2.1 Spin-echo method

Due to the spatial inhomogeneity in the applied dc field, the time constant associated with the free induction decay (FID) $T_2^*$ is shorter than $T_2$ and hence the FID after a single $\pi/2$ pulse can not be used to measure $T_2$. Instead, the spin echo method with a $(\pi/2 - \tau - \pi)$ sequence [6] is used. The effect of this pulse sequence on the spin system is shown in Figure 3.5, which can be understood as follows. The first $\pi/2$ pulse puts the magnetization in the transverse plane (say along $x'$-axis, if the pulse is applied along $y'$-axis). The magnetization starts de-phasing due to the spread in the Larmor frequencies. Next $\pi$ pulse (along the same $y'$-axis) at time $\tau$ inverts all individual magnetic moments (to lie along -$x'$ axis) thereby inverting the sequence of de-phasing as shown in Figure 3.5.

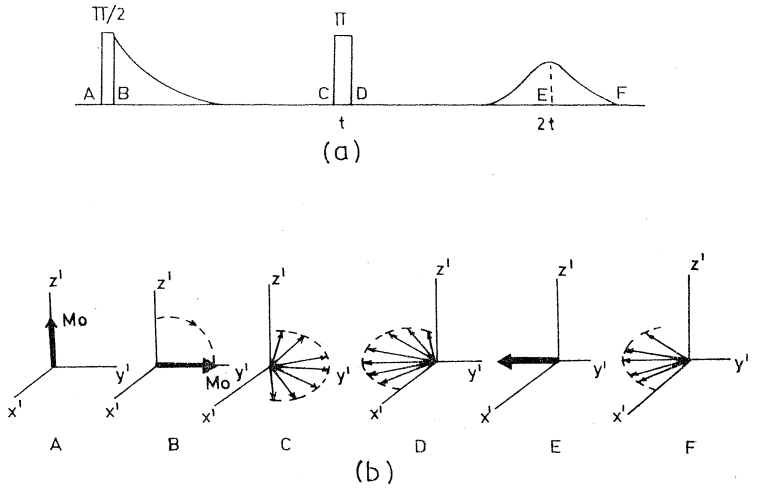


Figure 3.5: Spin echo sequence for $T_2$ measurements.

Therefore the spins refocus again after the time interval $\tau$ from the $\pi$ pulse forming an echo. If the $\pi$ pulse can invert the direction of the de-phasing of

all spins then the echo will have same magnitude as that of the FID. This means that the phase relations among these spins have not changed during the time $2\tau$. But these phase relations may change for some spins during the time $2\tau$ (*e.g.*, if the de-phasing is due to time varying local fields) and such spins do not coalesce with the other spins and so their contribution to spin echo will be missing. Thus any process which causes individual spins to de-phase in a irreversible manner will reduce the amplitude of the echo, and one obvious example of such process is spin-flip due to the spin-spin interaction. Thus by measuring the amplitude of the echo as a function of $\tau$ one can measure $T_2$ since the spin echo amplitude decreases as $\exp(-\tau/T_2)$.

#### 3.3.2.2 Carr-Purcell sequence

If there is a rapid diffusion in the inhomogeneous magnetic field, the spin echo amplitude is further reduced [1] and the above sequence is not effective for measuring $T_2$. A sequence suggested by Carr and Purcell [7] is well suited in such cases. This sequence consists of a $\pi/2$ pulse followed by a series of $\pi$ pulses at $t$, $3t$, $5t$ etc. The spin echoes arising out of this sequence is shown in Figure 3.6. It can be shown [8] that this sequence makes the contribution of diffusion due to the field inhomogeneity negligible. In this sequence error in setting the width of pulse does lead to some error in $T_2$ but this can be rectified by the insertion of a $90^0$ phase shift between the $\pi/2$ pulse and successive $\pi$ pulses, as suggested by Meiboom and Gill [9].

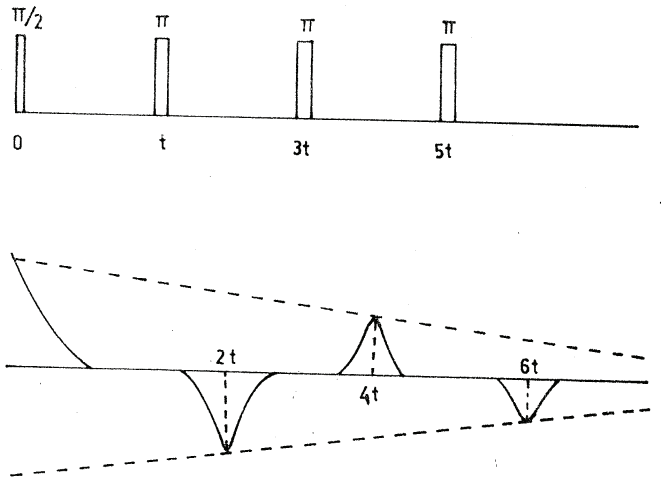


Figure 3.6: Carr-Purcell sequence for $T_2$ measurements.

## 3.4 Field-cycling NMR

A field-cycling spectrometer is characterized by the ability to periodically and significantly vary its longitudinal magnetic field strength, $B_0$ , on a time scale short compared to the spin-lattice relaxation times studied [10, 11]. This is usually achieved by either rapidly moving the sample between regions of different field strengths *via* mechanical methods, or keeping the sample stationary and changing the external field by varying the current through the solenoid. The main benefits of field-cycling over fixed-field spectrometers are their ability to affect spins with different gyromagnetic ratios without the need for multi-channel spectrometers with electronics tuned to multiple frequencies. Also, the preparation, recovery and detection of the spins can occur at different fields, allowing the frequency dependent study of the relaxation rates. Field-cycling relaxometry is the only NMR technique that permits one to cover several decades of the frequency with the same instrument and it is a powerful technique for the identification and characterization of various types of molecular dynamic processes in complex systems.

### 3.4.1 Field-cycling principle

The principle of a field-cycling NMR (FCNMR) relaxometry experiment is demonstrated in Figure 3.7. The sample is polarized in a magnetic field $B_p$ kept as high as technically possible with moderate requirements on homogeneity. The relaxation process takes place in a variable low-field interval $B_r$. The signal remaining after this relaxation interval is detected in a fixed field $B_d$ which is again as high as possible with preferably better homogeneity. The signals are acquired with a radio frequency (RF) unit tuned to a predetermined frequency irrespective of the relaxation field chosen. For detection, either the free induction decay after a simple $90^0$ RF pulse or a spin echo produced by a sequence of two or more pulses is recorded. In the Figure 3.7, T is the total period of the cycle which is repeated many times during the course of relaxation time measurements. The transit times ($t_{OFF}$ ($B_p \rightarrow B_r$) and $t_{ON}$ ($B_r \rightarrow B_d$) are the switching times of field OFF and ON respectively. The main conditions to be satisfied with these switching times is that on one hand they should be fast compared to the relaxation times of the system under study and on the other hand, they should be slow enough such that the time varying magnetic fields do not contain components in the vicinity of the Larmor frequency. The detailed theoretical and experimental background for FCNMR was extensively discussed in review articles [10–13].

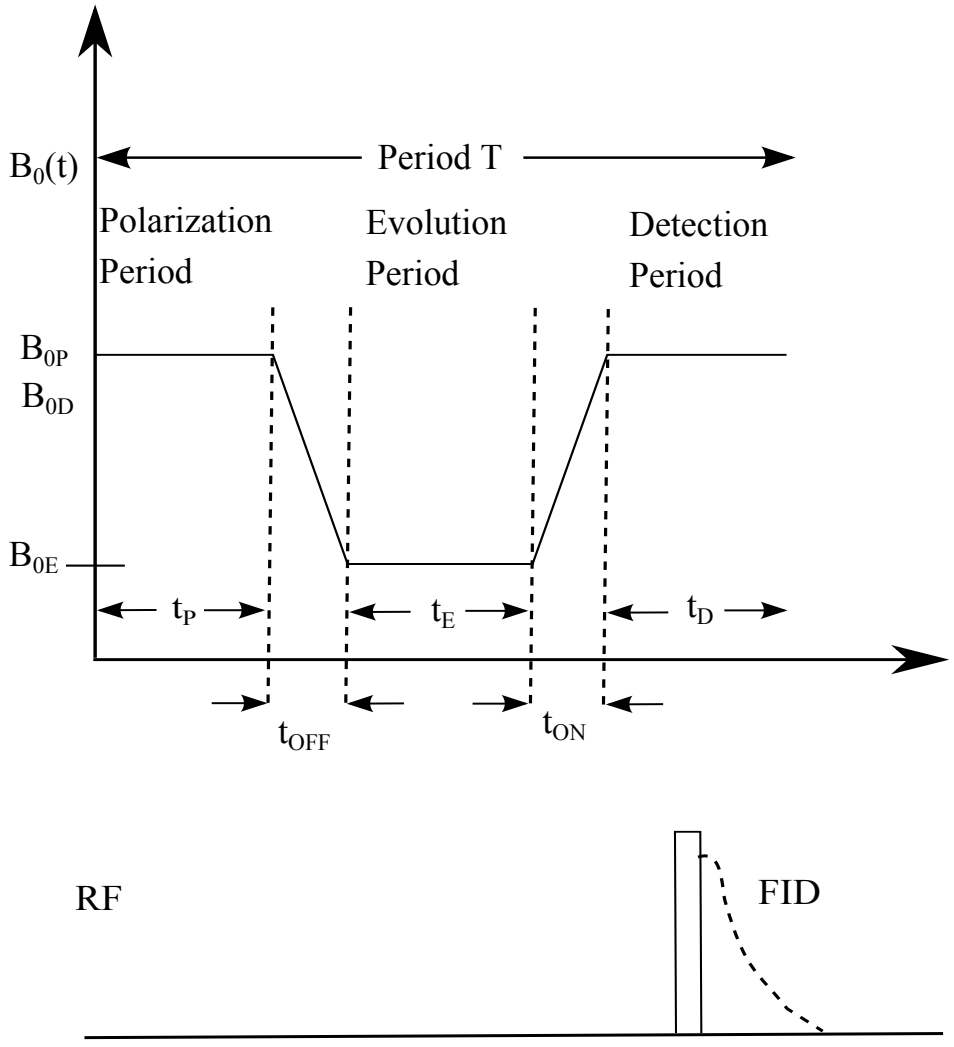


Figure 3.7: Schematic representation of a typical field-cycle experiment.

## 3.5 Pulse sequences for $T_1$ measurements

On field-cycling NMR relaxometers, the $T_1$ measurements are performed by using two standard pulse sequences.
1. Pre-polarized (PP) sequence for low fields (below 4 MHz)
2. Non-polarized (NP) sequence for high fields (above 4 MHz).

### 3.5.1 PP Sequence ($B_r \ll B_p$)

In this case, the sample is polarized in the polarization field, $B_p$, which is chosen as high as possible. The magnetic field is then switched to the preselected relaxation field, $B_r$, at which the spin-lattice relaxation is to be measured. The magnetization remaining after the relaxation interval $\tau$ is finally detected with the aid of a $90^o$ RF pulse or a suitable spin echo sequence in the form of an NMR signal after switching the magnetic field to a detection field $B_d$. After having recorded the signal, the magnetic field is switched back to the polarization field. Incrementing the relaxation interval $\tau$ thus permits one to record the relaxation curve for a given relaxation field $B_r$. The spin-lattice relaxation dispersion is then scanned point by point by stepping $B_r$ through a series of discrete values spread over the desired magnetic field (or frequency) range. Figure 3.8 shows a typical field cycle and time intervals needed to measure spin-lattice relaxation times by using PP sequence.

### 3.5.2 NP sequence ($B_r \rightarrow B_p$)

If the relaxation field $B_r$ approaches the polarization field $B_p$ the dynamic range of the relaxation curve becomes too small for accurate evaluation of spin-lattice relaxation times. In this case it is more favorable to start the cycle in the absence of any polarization field. Here non-equilibrium state is created by switching the field to the desired relaxation field $B_r$ value and the spins are allowed to relax for a time period $\tau$ and the remaining magnetization

is detected with the aid of $90^o$ pulse after switching the magnetic field to a detection field $B_d$. The process is repeated for different $\tau$ values to measure the spin-lattice relaxation time. Figure 3.9 shows a typical field cycle and time intervals needed to measure spin-lattice relaxation times by using NP sequence. In the present work, a commercial relaxometer (Stelar Spin mater, Italy) was used, and Figure 3.10 shows the block diagram.

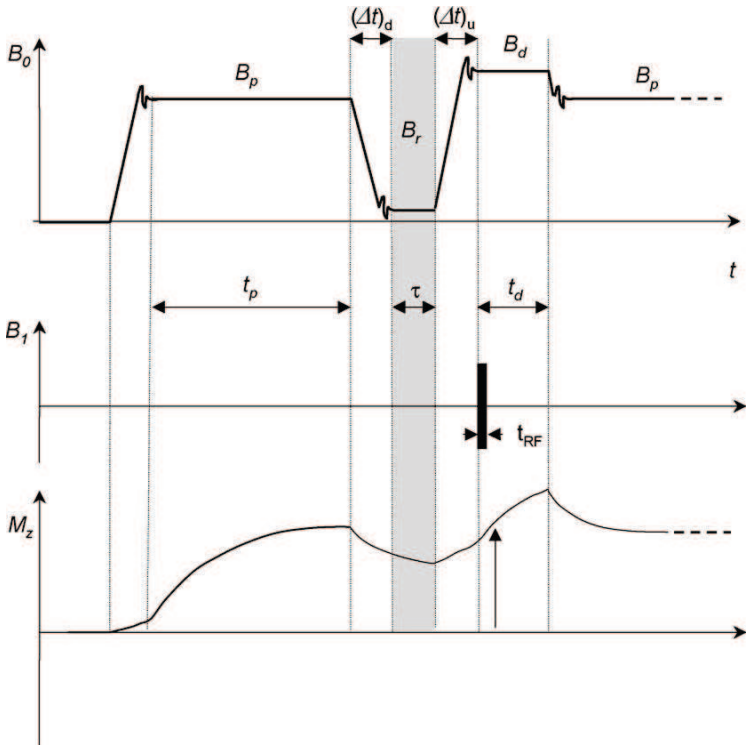


Figure 3.8: Field cycle for low relaxation fields ($B_r \ll B_p$): schematic representation of the external field $B_0$, the radio frequency amplitude $B_1$, and the magnetization $M_z$ in the diverse field-cycling time intervals for polarization fields much larger than the relaxation field. The shaded section indicates the variable relaxation interval $\tau$. The vertical arrow indicates the time when the signal is recorded. The polarization interval $t_p$ is typically chosen to be five times the spin-lattice relaxation time in that field. The detection interval $t_d$ may be as short as needed for the acquisition of an FID signal. The down and up field switching times are indicated by the intervals $(\Delta t)_d$ and $(\Delta t)_u$, respectively. $t_{RF}$ is the RF pulse width. The cycle is repeated periodically for different relaxation intervals $\tau$ and different relaxation fields $B_r$ while all other intervals and magnetic fields remain constant [11].

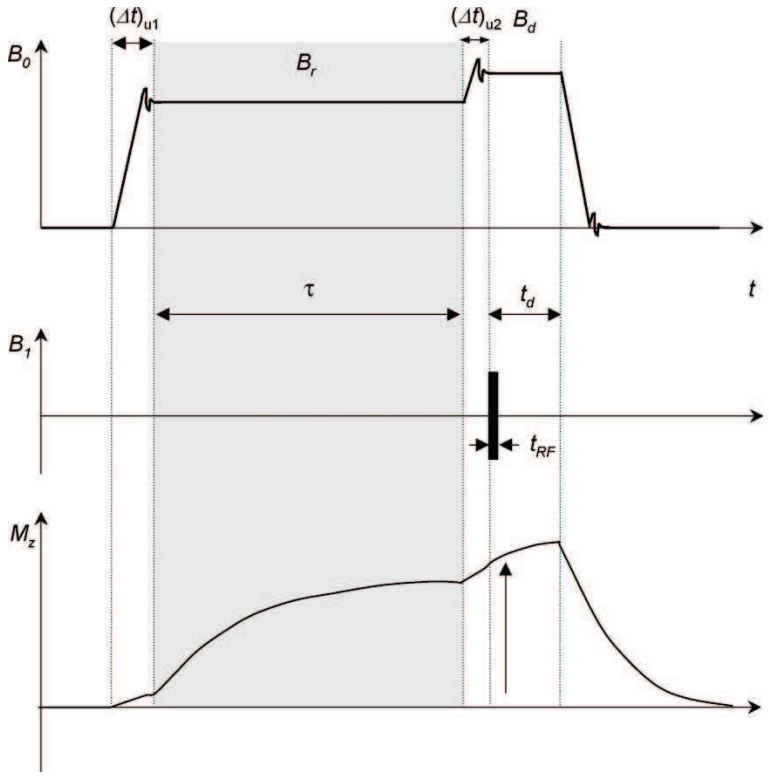


Figure 3.9: Field cycle for high relaxation fields ($B_r \rightarrow B_d$): schematic representation of the external flux density $B_0$, the radio frequency amplitude $B_1$, and the magnetization $M_z$ in the diverse field-cycling time intervals for relaxation fields approaching the detection field. The shaded section indicates the relaxation interval $\tau$. The vertical arrow indicates the time when the signal is recorded. The field switching times are indicated by the intervals $(\Delta t)_{u1}$ (from zero to the relaxation field) and $(\Delta t)_{u2}$ (from the relaxation field to the detection field). $t_{RF}$ is the RF pulse width. The recycle delay should be long enough to ensure complete relaxation of the magnetization before the next cycle begins. The cycle is repeated periodically for different relaxation intervals $\tau$ and different relaxation fields $B_r$ while all other intervals and magnetic fields remain constant [11].

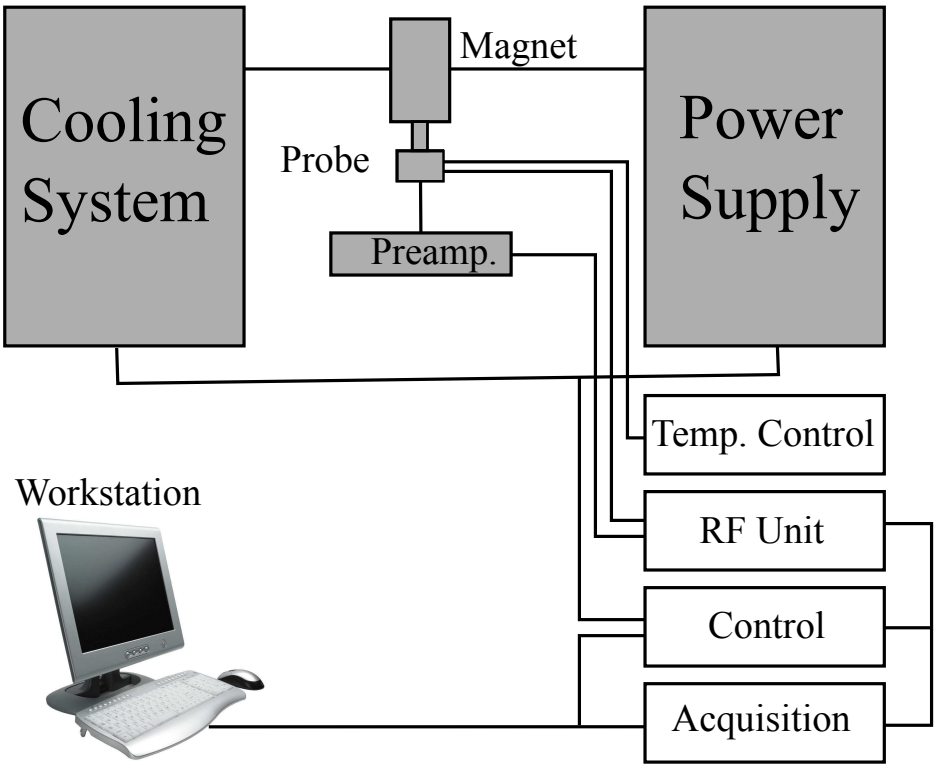


Figure 3.10: Block diagram of a Stelar FFCNMR Relaxometer.

Table 3.1: Specifications of pulsed NMR spectrometer

| | |
|---|---|
| Operating frequency range | 3.5 MHz to 60 MHz |
| Field stability | 1 in $10^6$ |
| Field homogeneity | 1 in $10^6$ |
| Bandwidth | 2 MHz at a given frequency |
| Pulsed *rf* power | up to 300W |
| ON/OFF ratio of the gated pulse | 100 dB modulator |
| Typical $\pi/2$ pulse width | 2-4 $\mu$s for proton |
| Pulse sequence used | Inversion recovery, Saturation burst |
| Method of detection | Single coil parallel resonance type |
| Transmitter isolation | 60 dB minimum |
| Recovery time | 15 $\mu$s |
| *rf* gain of the receiver | Typically 80 dB, adjustable over a range of 40 dB |
| Temperature range | 25$^o$C to 120$^o$C (with 0.1$^o$C stability over the period of the experiment) |

Table 3.2: Specifications of FFCNMR relaxometer

| | |
|---|---|
| Magnet | Aluminum air coil system |
| Maximum operating frequency | 21 MHz |
| Field switching time | $< 0.15$ ms/MHz |
| Field stability | 1 in $10^5$ |
| Field homogeneity | 1 in $10^4$ over 1 cm$^3$ |
| Bandwidth of the *rf* spectrometer | 2 MHz |
| Pulsed *rf* power | up to 300W |
| ON/OFF ratio of the gated pulse | 100 dB modulator |
| Typical $\pi/2$ pulse width | 5-10 $\mu$s for proton |
| Method of detection | Single coil parallel resonance type |
| Transmitter isolation | 60 dB minimum |
| Recovery time | 20 $\mu$s |
| Interface bus with PC | LPT |
| *rf* gain of the receiver | Typically 80 dB, adjustable over a range of 40 dB |
| Temperature controller | Gas flow type PID, VTC 90 (Stelar made) |
| Temperature range | -140$^o$C to 140$^o$C with 0.1$^o$C stability over a day |

## 3.6 Sample preparation

All the liquid crystalline compounds reported in this work were synthesized in the laboratory of Professor R. Dabrowski at the Military University of Technology, Warsaw, Poland and were used without further purification. The pure or bulk liquid crystal samples were sealed in standard NMR tubes under vacuum ($10^{-5}$ Torr) by removing the dissolved paramagnetic impurities using the freeze-pump-thaw technique. The liquid crystal-aerosil mixtures were prepared by the solvent method [14]. Aerosil (type A300 from Degussa Corp.) was dried over night at 200$^o$C under vacuum before adding it to the liquid crystal. Aerosil powder was added to a dilute solution of liquid crystal in pure acetone. This solution was kept in the sonicator for about 2 hours to achieve a homogeneous dispersion. The solvent was then evaporated by keeping the sample at 60$^o$C about 15 hours. The mixture was transferred into the NMR tube and was sealed under vacuum. Aerosil A300 consists of small silica spheres of average diameter 7nm and a specific surface area of 300 $m^2/g$. The surface of these spheres is covered with hydroxyl groups that interact with each other via hydrogen bonding and thus form a 3-d network. Due to the hydrophilic nature of the spheres and the polar nature of the liquid crystal, the alignment of the molecules at the silica surfaces is expected to be homeotropic.

Liquid crystal-Aerosil mixtures are usually characterized in terms of the aerosil density defined as $\rho_a = m_a/V_{LC}$, where $m_a$ is the mass of aerosil and $V_{LC}$ is the volume of the liquid crystal. Assuming the density of the LC to be $\approx 1 g/cm^3$, $\rho_a$ can be written as just $m_a/m_{LC}$, where $m_{LC}$ is the mass of the liquid crystal. Relaxation measurements in Chapters 5 and 6 are carried out on composites with $\rho_a = 0.05, 0.07$ $g/cm^3$.

# References

[1] C. P. Slichter, *Principles of Magnetic Resonance*, Springer-Verlag, Berlin (1996).

[2] A. Abragam, *The Principles of Nuclear Magnetism*, Clarendon Press, Oxford (1961).

[3] F. Bloch, Phy. Rev. **70**, 460 (1946).

[4] E. Fakushima and S. B. W. Roeder, *Experimental Pulsed NMR: A Nuts and Bolts Approach*, Addision Wesley, Reading, Massachusetts (1981).

[5] T. C. Farrar and E. D. Becker, *Pulsed and Fourier Transform NMR*, Academic Press, New York (1971).

[6] E. L. Hahn, Phys. Rev. B **80**, 580 (1950).

[7] H. Y. Carr, and E. M. Purcell, Phys. Rev. **94**, 630 (1964).

[8] D. C. Ailion, *Methods of Solid State Physics*, ed., J. N. Mundy, S. J. Rothman, K. H. Fluss and L. C. Sumedskjaer, (Academic Press), **21**, 439(1983).

[9] S. Meiboom and D. Gill, Rev. Sci. Instrum. **29**, 6881 (1958).

[10] F. Noack, *NMR field-cycling spectroscopy: principles and applications*, Prog. Nucl. Magn. Reson. Spectrosc. **18**, 171 (1986).

[11] R. Kimmich and E. Anarado, *Field cycling NMR relaxometry*, Prog. Nucl. Magn. Reson. Spectrosc. **44**, 257 (2004).

[12] R. Kimmich, Bull. Magn. Reson. **1**, 195(1980).

[13] E. Anoardo, G. Galli, and G. Ferrante, Appl. Magn. Reson. **20**, 365 (2001).

[14] H. Haya, C. W. Garland, Phys. Rev. E **56**, 3044 (1997).

# 4

# Multi-nuclear NMR relaxometry study of slow dynamics in liquid crystals

## 4.1 Introduction

The laterally fluorinated liquid crystal compounds have attracted recent attention because of their potential applications in display technology and telecommunications [1–9]. The replacement of hydrogen with fluorine on the aromatic core reduces the melting point and smectogenity leading to a wide nematic range. Mixtures of these singly or doubly fluorinated compounds (on the aromatic cores) have high figure-of-merit, low viscosity and high birefringence, which are the favorable physical parameters for liquid crystal display devices. Detailed dielectric studies were carried out on singly fluorinated compounds to examine the correlation times of reorientations [6]. Our interest in studying them using NMR relaxometry is to examine the type of slow molecular processes in these systems, and we wish to study them probing with two different nuclei ($^1H$ and $^{19}F$) residing on the same molecule. Based on physical arguments, we expect the two nuclear species to have qualitatively different relaxation paths, and hence expectedly different types of dynamic information on the same molecule. With this objective, we have chosen two liquid crystals (belonging to the family of tolanes) with one fluorine

substituted in the place of hydrogen attached on the core. In NMR experiments involving liquid crystals, the $^1H$ spin relaxation process are effectively mediated by homo-nuclear dipolar interactions time modulated by various molecular processes pertinent to the system. As was discussed in Chapter-2 (Theory chapter) the spin-lattice relaxation rates are determined by molecular reorientations (either individual or collective). In a similar experiment with a lone $^{19}F$ (spin-$\frac{1}{2}$) as the probing nucleus, however, the relaxation process could be via three mechanisms: the hetero-nuclear dipolar coupling with neighboring protons, chemical shift anisotropy and spin-rotation interaction (this interaction being relatively ineffective in case of $^1H$ nuclei). We find that in the present system under the conditions of low frequency relaxometry the last mechanism is dominant, and hence the experiments are able to report exclusively on the underlying modulating molecular process involving angular momentum correlations. We present here complementing results of our study on spin-lattice relaxation rate dispersions of proton and fluorine nuclei as a function of Larmor frequency at different temperatures in the isotropic phase of two singly fluorinated liquid crystal systems.

The present experiment involving spin-lattice relaxation rates of two distinct nuclear spins coupled through dipolar interaction develops certain interesting features during the field-cycling process. As we reach out to probe slower dynamic process by making the resonance frequencies of the two systems progressively smaller, the two spin systems (say, $I$ for proton and $S$ for fluorine), which are to begin with (at higher frequencies) are *unlike* (due to distinct and well separated resonance lines) and hence have hetero-nuclear dipolar interaction, start developing overlapping resonance lines imparting thereby certain degree of homo-nuclear dipolar coupling, much like the case of *like* spins. In terms of nuclear spin Hamiltonian of the two spins, the experiment can thus transit from a weak-coupling limit (WC: $I$-$S$ interaction energy is smaller than the difference between the Lamor frequencies of $I$ and $S$ amplitude-wise) to the strong-coupling limit (SC). In our case involving $^1H$ and $^{19}F$, the region of relatively larger resonance frequencies ($\geq 400$ kHz) is in

the weak-coupling limit of the NMR experiment, and hence the dispersions are modeled in terms of different individual/collective dynamic processes, contributing to the respective spin-lattice relaxation rates ($R_1 = T_1^{-1}$). At lower frequencies (strong-coupling limit) the overlap of the resonance lines of the two nuclear species provides another mechanism ($T_{21}^{-1}$), different from $R_1$ ($= T_1^{-1}$), and the experimental data are interpreted accordingly.

## 4.2 Experimental details

The molecular structure and the phase sequence of the liquid crystals 4′-butoxy-3′-fluoro-4-isothiocyantotolane (4OFTOL) and 4′-butoxy-3-fluoro-4-isothiocyantotolane (4OTOLFo) are shown in Figure 4.1. We shall henceforth refer to 4OFTOL as sample 1 and 4OTOLFo as sample 2. These compounds were synthesized in the laboratory of Prof. R. Dabrowski in Warsaw, Poland. The method of synthesis and properties are described in Ref. [10, 11]. Sample preparation, experimental set up and various pulse sequences used for relaxation measurements are given in Chapter 3. Frequency dispersions of proton and fluorine spin-lattice relaxation rates $R_1$ at different temperatures in the isotropic phase were measured over a frequency range of 10 kHz to 50 MHz with a commercial fast field-cycling NMR relaxometer (Stelar, Italy), supplemented by a variable-field pulsed NMR spectrometer covering the higher end of the frequencies (10 - 50 MHz). The frequency dependence of the relaxation rates of both the nuclei for sample 1 are shown in Figures 4.2 and 4.3, and for sample 2 are shown in Figures 4.4 and 4.5. The relaxation rates were also measured as a function of temperature at chosen Larmor frequencies $\nu_L$ ($\omega = 2\pi\nu_L$) for both the nuclei and the results are shown in Figures 4.6 and 4.7 for sample 1 and Figures 4.8 and 4.9 for sample 2. Temperature of the samples was maintained by passing dry air over them to an accuracy of $\pm$ 0.1$^o$C. Relative errors in the $R_1$ measurements of proton are within 2% and in the case of fluorine the errors are within 5%. The frequency dispersion data of proton for sample 1 clearly show the onset of critical fluctuations even at 11$^o$C away from the isotropic-nematic transition temperature ($T_{NI}$).

The temperature variation of proton data also confirms the contribution of critical fluctuations near, and as well as far away, from the transition. In the case of sample 2 the critical fluctuations contribution is negligible at $11^oC$ away from the respective $T_{NI}$ and the dispersion observed at higher frequencies is governed by individual processes. However in the case of fluorine, the relaxation rate dispersions are qualitatively different from those of protons in both the compounds (comparing Figures 4.2 and 4.4 with Figures 4.3 and 4.5). These exhibit a low-frequency enhancement in the relaxation rate at all the temperatures in the isotropic phase of both the samples. The temperature dependence of the spin-lattice relaxation rate of fluorine nuclei also shows a contrasting behavior compared to the proton. The last two observations point to possible differences in the relaxation pathways of the two nuclear species, even though they reside on the same liquid crystal molecule.

4'-butoxy-3'-fluoro-4-isothiocyantotolane (4OFTOL)

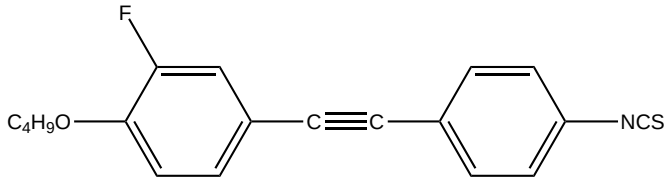


Cr 64.2°C N 71.6°C I

Sample 1

4'-butoxy-3-fluoro-4-isothiocyantotolane (4OTOLFo)

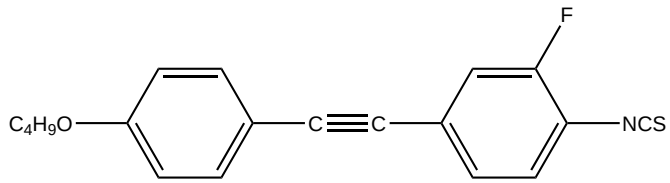


Cr 96.7°C N 89.9°C I

Sample 2

4'-butoxy-2-fluoro-4-isothiocyantotolane (4OTOLFm)

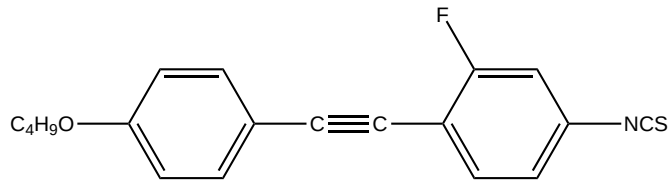


Cr 70.3°C N 94.5°C I

Sample 3

Figure 4.1: Molecular structures and phase sequences of liquid crystals 4OFTOL (Sample 1) and 4OTOLFo (Sample 2) [4OTOLFm (Sample 3) is given for comparison].

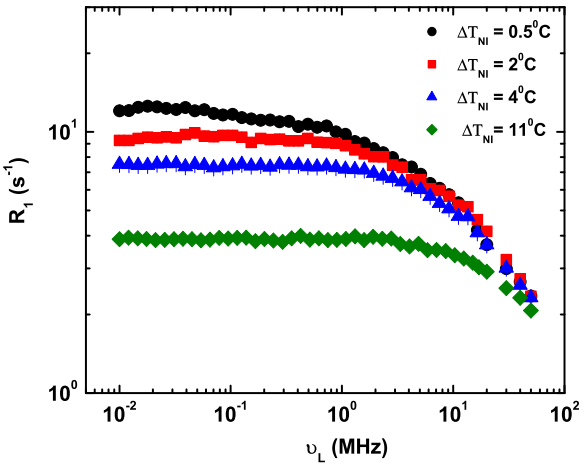


Figure 4.2: Proton spin-lattice relaxation rate of sample 1 at different temperatures as a function of Larmor frequency.

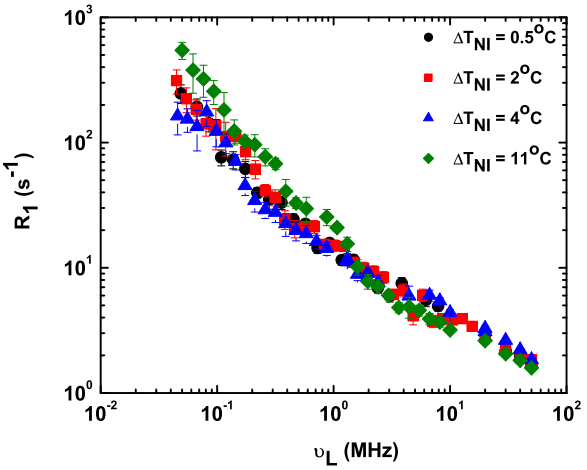


Figure 4.3: Fluorine spin-lattice relaxation rate of sample 1 at different temperatures as a function of Larmor frequency.

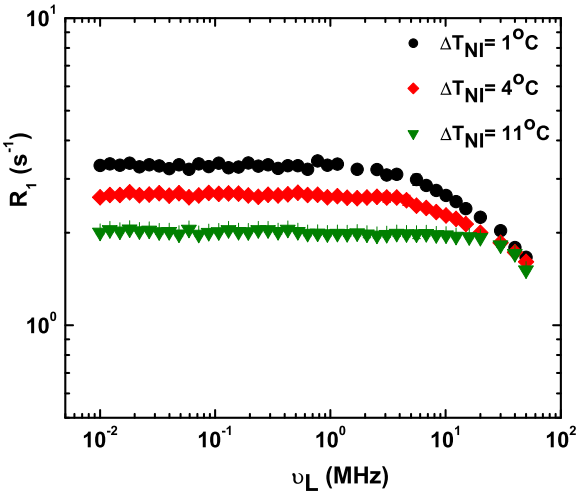


Figure 4.4: Proton spin-lattice relaxation rate of sample 2 at different temperatures as a function of Larmor frequency.

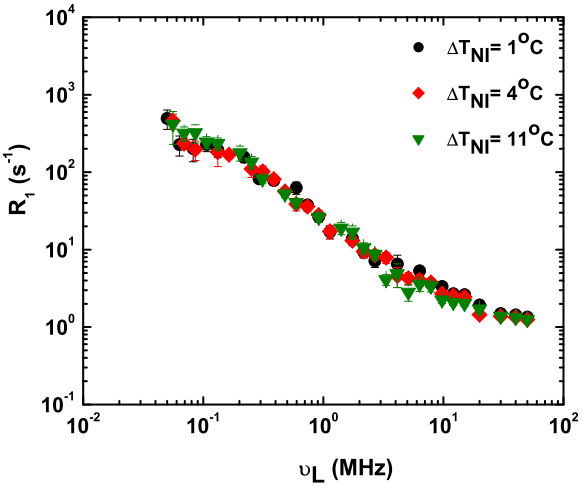


Figure 4.5: Fluorine spin-lattice relaxation rate of sample 2 at different temperatures as a function of Larmor frequency.

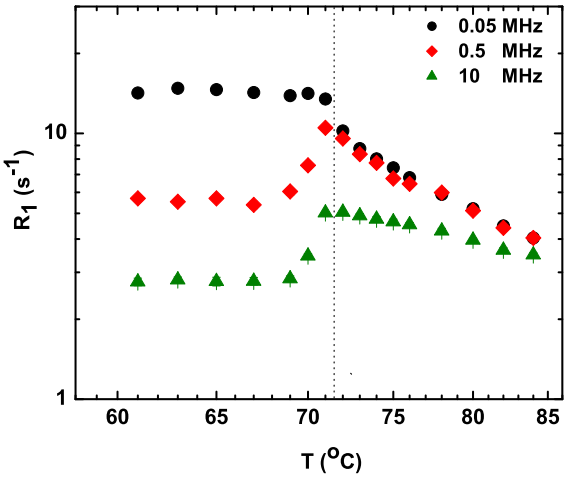


Figure 4.6: Proton spin-lattice relaxation rates plotted against temperature at different Larmor frequencies for sample 1. The dotted line in the figure indicates the isotropic-nematic transition temperature.

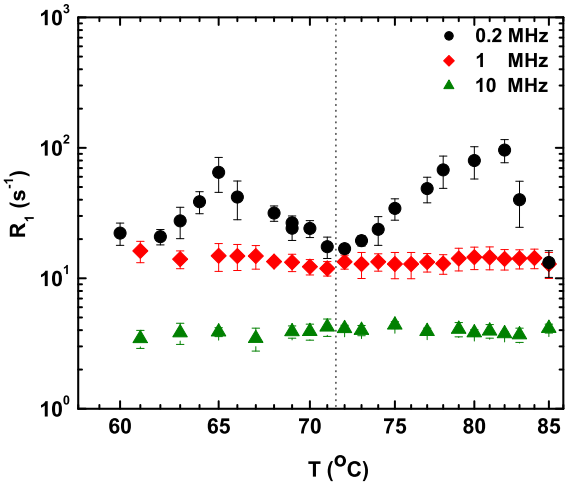


Figure 4.7: Fluorine spin-lattice relaxation rates plotted against temperature at different Larmor frequencies for sample 1. The dotted line in the figure indicates the isotropic-nematic transition temperature.

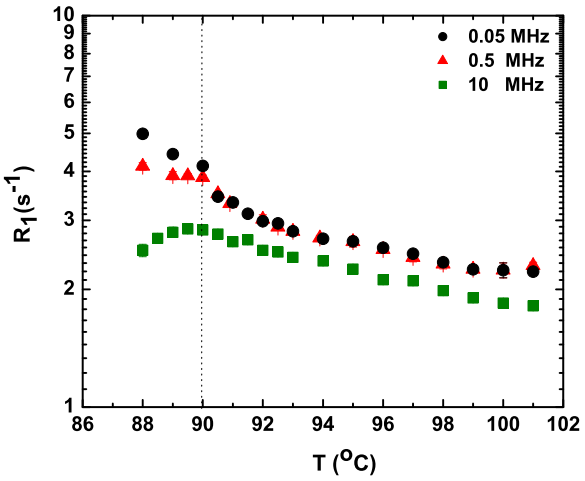


Figure 4.8: Proton spin-lattice relaxation rates plotted against temperature at different Larmor frequencies for sample 2. The dotted line in the figure indicates the isotropic-nematic transition temperature.

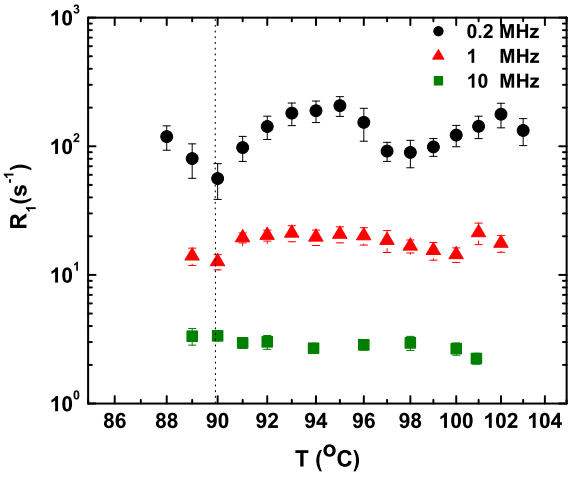


Figure 4.9: Fluorine spin-lattice relaxation rates plotted against temperature at different Larmor frequencies for sample 2. The dotted line in the figure indicates the isotropic-nematic transition temperature.

## 4.3 Relaxation models

### 4.3.1 Proton relaxation

Proton spin-lattice relaxation in such systems is known to occur via the time modulation of dipole-dipole interactions [12–14] and the relevant dynamic mechanisms that modulate (randomly) this interaction within the NMR window are: individual molecular reorientations modulating intra-molecular dipolar couplings; translational diffusion effecting the inter-molecular dipolar interactions; collective dynamics arising from critical fluctuations of the nematic order; and possibly a constant background contribution from such other processes which are too fast for the experiment. In our system we find from our analysis that the translational diffusion contribution is practically constant over the frequency range, and hence cannot be distinguished from the background. The dispersion thus is due to molecular reorientations (about the molecular short axes) (R), and critical fluctuations (CF). Assuming that the models are statistically independent, the measured relaxation rate ($R_{1H}$) can be written as a sum of three contributions:

$$R_{1H} = R_{1H0} + R_{1HR} + R_{1HCF}. \tag{4.1}$$

The first contribution represents the constant background, while the second and third terms are contributions from R and CF mechanisms, respectively. The theoretical expressions for these processes are given in Chapter 2.

### 4.3.2 Fluorine relaxation

Fluorine spin-lattice relaxation is mediated, in principle, through the time modulation of inter- and intra-molecular dipolar interactions, chemical shift anisotropy (CSA), and spin-rotation interaction. The contribution from the chemical shift anisotropy (CSA) to the relaxation is not significant in the

present case due to two reasons: relatively very low fields at which the experiments are especially designed and performed, and effective averaging of the CSA tensor component correlations in the isotropic phase. In the present case, its relaxation through intra-molecular dipolar interaction *via* hetero-nuclear coupling with proton, and spin-rotation interaction involving molecular angular momentum correlations, seems to be more appropriate [15–19]. The other contributions are negligible in our analysis in the frequency range of our experiment. In our experiments we find that the non-equilibrium magnetization of both fluorine and proton decay exponentially to equilibrium over at least three decades of time scales, indicating that the two spin reservoirs are not coupled during the relaxation process [14]. Thus the effect of hetero-nuclear coupling of, say, fluorine to proton is modifying the expression for the relaxation rate (of *like* spins, equations 2.20 to 2.23a) involving uncoupled reservoirs of *unlike* spins.

Focussing on the possible contribution to the fluorine relaxation from intra-molecular hetero-nuclear dipolar coupling with neighboring protons ($R_{1F}^{HF}$), the fluorine spin-lattice relaxation rate in the presence of coupling to unlike spins ($^1H$ and $^{19}F$) is written as

$$R_{1F}^{HF} = A_1^{HF}\left[\frac{1}{12}J^{(0)}\left(\omega_F - \omega_H\right) + \frac{3}{2}J^{(1)}\left(\omega_F\right) + \frac{3}{4}J^{(2)}\left(\omega_F + \omega_H\right)\right]. \quad (4.2)$$

with $J^k(\omega)$ representing the spectral density corresponding to fluctuations of the k$^{th}$ tensor component in the interaction Hamiltonian at the frequency $\omega$. We use this expression for analyzing the fluorine data, drawing upon R and CF mechanisms to modulate the H-F dipolar coupling and hence contribute to the spectral densities, at the appropriate frequencies, as above (Here after we drop the superscript HF for convenience). However we observe that the contribution at low frequency (through the term $J^{(0)}\left(\omega_F - \omega_H\right)$ is not adequate to account for the very significant enhancement of fluorine relaxation rate ($R_{1F}$) at low frequencies ($\sim$ 1 MHz). So, we need to look for a qualitatively different pathway for the coupling of fluorine spin system to

the lattice. An explanation of this observation seems to lie in examining the concept connected with the model: the torques experienced by the molecule due to its interactions with its neighbors are on the time scale of molecular interactions (like,*e.g.*, molecular collisions), and hence fluctuate rapidly. This however does not take into account the possibility that there could be slow collective modes in the system which can in principle generate torques on a much longer time scale. In such a case, a well designed probe could sense such an environment, and could report on the underlying collective molecular processes.

In this context, conclusions of earlier molecular dynamic studies in liquid crystals using electron spin resonance (ESR) techniques, in their mesophases in general and in their isotropic phase in particular, may be recalled. Extensive investigations on the line shapes of ESR spectra of different nitroxide radicals dissolved in liquid crystals indicated that simulation of spectral shapes based on simple rotational dynamical models was not adequate in accounting for the observed data [20, 21]. Subsequent time domain studies using 2-d ESR methods confirmed that such probing nitroxide molecules were subjected to influences of local ordering. The effect of time fluctuations of this ordering is two fold: on one hand it produces a potential arising out of the mean torques and the angular momentum components of the probe tend to relax on a modified time scale in the presence of this torque; and on the other the potential of the mean torque itself, in addition, undergoes a slow rotational diffusion as a result of the dynamics of the locally ordered structure, termed as the cage, taking place on a much longer time scale, in effect representing the collective modes in the system. And the larger the probe molecule is, the more sensitive is its own dynamics to these modes, and hence the more discernible will be the details of these processes to the probing spins residing on the molecule. The question of dealing with a wide spectrum of torques influencing the random rotational dynamics of a probing molecule is normally approximated to the assumption of the existence of two distinct regions relative to the time scale of the experiment: those which are very

fast and provide the usual mechanism for the angular momentum relaxation on a very short time scale; and those which persist on a much longer scale competing with the time scales of the spin dynamics. These are dealt with, for example in the case of the ESR experiment, by extending the space of relevant stochastic variables, needed to account for the random time modulation of the associated magnetic interaction, to include the cage dynamics as well, along with measurable spin variables. The random process as described in this composite space is then presumed to be Markovian, and is dealt with suitably by generalizing the associated stochastic Liouville equation (SLE). This method of dealing with slow modes to interpret observations in magnetic resonance spectroscopy through the so-called augmented SLE was developed by Freed and his coworkers [21], and extensive 2-dimensional ESR work on probes of different sizes to elucidate this mechanism was reported earlier [22, 23]. The idea thus is to include these slow modes through a model of a slowly relaxing local structure (SRLS) influencing the dynamics of the probe, besides the other local processes. Modeling the dynamics of SRLS is a matter of choice, and a simple isotropic rotational Brownian motion of the cage on a well separated time scale (with correlation time $\tau_C$) was earlier found to be reasonably adequate to represent the effect of these slow collective modes. From the detailed ESR studies [21] the correlation times of such cages in the isotropic phases are estimated to be in terms of ns. The inferred value very much depends on the size and symmetry of the reporting probe, the effect being increasingly significant with larger and more anisotropic ESR probes as a rule. Important message from these interesting investigations, relevant to our present work, is the observation that even in the isotropic phase the probing ESR molecules seem to experience very slow torques as a result of short range cooperative behavior of the anisotropic molecules constituting the medium.

The above scenario needs to be discussed in the present context, however with two important differences: here the probe molecule is one of the liquid crystal molecules itself and hence the effect of these slow processes is expec-

ted to be most effectively experienced and reported; and secondly, unlike the case of the ESR relaxation processes mentioned (which are still sensitive to correlations among different molecular orientations and hence could experience the effect of the fluctuating torques rather indirectly via coarse-grained angular variables), the relaxation mechanism of fluorine (under the specific experimental situation pertinent to the present study) is primarily governed by the relaxation processes of the (liquid crystal) molecular angular momentum components themselves, thus leading to a direct observation of these slow processes. Thus the present field-cycling NMR experiment with the fluorine probe seems to be focusing directly, and effectively, on these slow modes of the liquid crystal medium. These ideas can now be readily adapted to the nuclear spin relaxation phenomena.

We consider the dispersion profile data as belonging to two distinct regions: the Larmor frequency region high enough for the weak coupling limit (where the resonance lines of both the nuclei are well separated) to be valid and hence the above relaxation formulation can be applied for interpreting the data (WC limit); and the low frequency region wherein the hetero-nuclear coupling between $^{19}F$ and $^{1}H$ nuclei acquires homo-nuclear character due to the progressive overlap of resonance lines and hence leads to a qualitatively different path for relaxation (cross-relaxation mechanism: SC limit). Fluorine nuclei in the present case are, for all practical purposes as per the earlier argument, exclusively relaxed via the spin-rotation interaction (in the WC limit) and hence via the angular momentum fluctuations. These in turn are sensitive to the local torques experienced in the medium, and following the arguments advanced in the earlier ESR work, one can divide them into two time-scales: the shorter time scales ($\sim 10^{-12}$ to $10^{-13}$ sec) aiding the usual angular momentum relaxation processes encountered in simple unstructured liquids; and the longer time scales of the cage dynamics corresponding to slower angular component fluctuations. The relaxation rate of fluorine in the high frequency range ($\geq$ 400 kHz), corresponding to the so-called weak-coupling limit [14] in terms of NMR spin Hamiltonian, is then written as

$$R_{1F} = R_{1F0} + R_{1FR} + R_{1FCF} + R_{1FC}. \tag{4.3}$$

The first term is due to fast processes and it is found to be very small (relative to other dominating contributions) within the errors so we neglect this contribution in our analysis. The second term arises from the time modulation of hetero-nuclear dipolar interaction through molecular reorientations. The third term is the contribution of effect of critical fluctuations of the short-range nematic order on the hetero-nuclear dipolar coupling. The spectral density expressions for these relaxation models are given in Chapter 2, and we use equation 4.2 for evaluating the relaxation rate contribution.

The fourth term is the contribution coming from the slow collective modes representing the time modulation of the torques due to relaxation of local structures coupling to the spin through their effect on molecular rotational dynamics. This is modeled as [15, 21]

$$R_{1FC} = A_{FC}\frac{\tau_C}{1+\omega^2\tau_C^2}. \tag{4.4}$$

Here $A_{FC}$ is a temperature dependent parameter quantifying the degree of this coupling.

## 4.4 Data analysis and discussion

### 4.4.1 Sample 1

The experimental data are analyzed by using non-linear least squares procedure [24]. The proton dispersion data are fitted to equation 4.1 at the four temperatures, as shown in Figures 4.10 to 4.13. Each dispersion is decomposed into a frequency-independent contribution (from fast processes, like molecular reorientations around the long-axes and alkyl chain dynamics). We also

find from our analysis that the inter-molecular dipolar interaction modulated by the translational diffusion is also relatively fast on our experimental time scale, and hence leads to a constant contribution along with the other such processes. This leaves the possible mechanisms which can contribute to the dispersion of the data to comprise of: reorientations around the short-axes and critical fluctuations of the order parameter of the transition. The fitted model parameters are given in Table 4.1. The experimental data as well as the analysis clearly show that contribution from the CF mechanism extends to low frequency region even at 11$^o$C away from the transition into the isotropic phase, which is somewhat unusual in typical liquid crystals. Interestingly, these correlation times $\tau_{CF}$ are quite high near the transition (363 ns) and this mechanism continues to be operative even far away into the isotropic phase (35 ns) (see Table 4.1). The $\tau_{CF}$ values measured with this technique for other samples like 4OTOLFm (4′-butoxy-2-fluoro-4-isothiocyantotolane) and 8OCB (4′-octyloxy-4-cyanobiphenyl) were, respectively, 68 ns and 180 ns near the transition, and the presence of CF was not observed at such higher temperatures, unlike the present system [19, 25]. Dielectric studies on this system [6] suggest that the transverse dipole moment of this molecule is not completely averaged out due to the location of fluorine atom on the core (see Figure 4.1), which seems to hinder the wing rotation about the para axes.

Interestingly, this situation is different for example, even from a closely related system wherein the fluorine substitution is in the meta position (referred to as 4OTOLFm, Figure 4.1). Our proton dispersion measurements on both these systems [19, 25] show a lower $\tau_{CF}$ values near the transition point. In particular the comparison with 4OTOLFm and 4OTOLFo are more relevant since the only difference in these compounds is the location of the fluorine and consequent differential averaging of the lateral dipole moment. We observe from the present work that such remnant transverse dipoles residing on the molecules of 4OFTOL are perhaps promoting larger nematic cluster sizes due to cooperative interactions introduced by the unaveraged electric dipolar coupling among the molecules during the pretransitional dynamic organiza-

tion of the molecules, leading of course to longer life times of the clusters ($\tau_{CF}$). It may further be noted that this difference between the structures of 4OFTOL and other singly fluorinated compounds also leads to differences in their order parameter values [6]. The molecular reorientations about the short axes are characterized by a correlation time $\tau_R$ varying from 3.96 ns to 2.4 ns as the sample is heated by about 11$^o$C (see Table. 4.1), while the corresponding variation in the related system 4OTOLFm over a comparable temperature range above the clearing point is from 1.67 to 1.39 ns [19, 26]. The temperature dependence of the relaxation rate at low frequencies shown in Figure. 4.6 further provides evidence for the presence of significant critical fluctuations even at elevated temperatures.

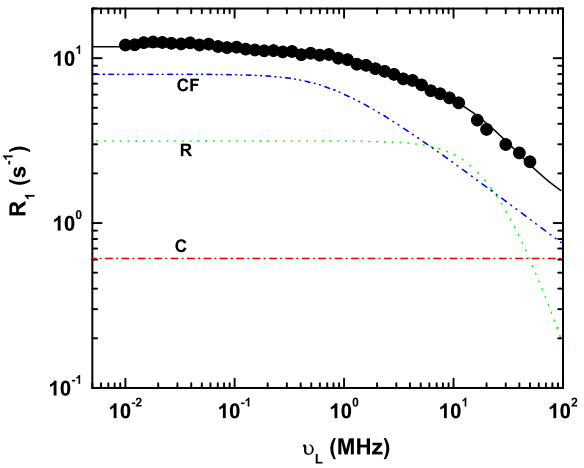


Figure 4.10: Proton spin-lattice relaxation rate dispersion of Sample 1 plotted against Larmor frequency is fitted to equation 4.1 at $\Delta T_{NI} = 0.5^o$C.

In order to analyze the more pronounced fluorine dispersion, we use the correlation times ($\tau_R$ and $\tau_{CF}$) obtained from the proton results as supplementary inputs, and focus on its interpretation (within the WC limit) in terms of the collective modes modulating the spin-rotation interaction, as

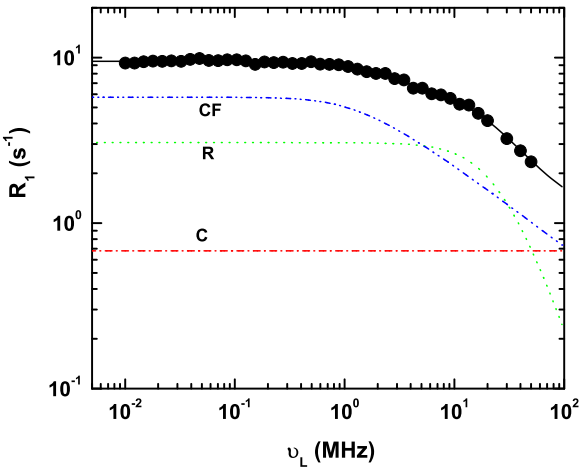


Figure 4.11: Proton spin-lattice relaxation rate dispersion of Sample 1 plotted against Larmor frequency is fitted to equation 4.1 at $\Delta T_{NI} = 2^o$C.

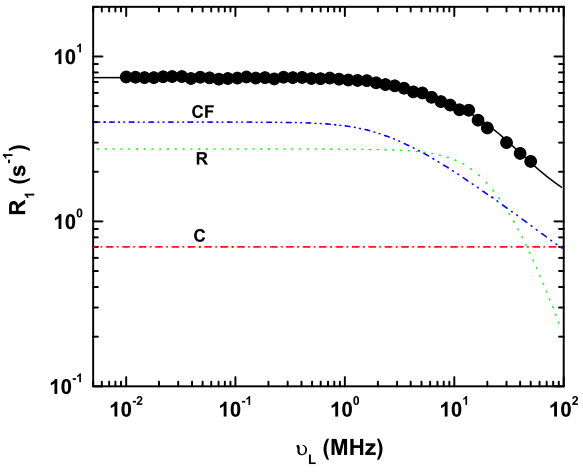


Figure 4.12: Proton spin-lattice relaxation rate dispersion of Sample 1 plotted against Larmor frequency is fitted to equation 4.1 at $\Delta T_{NI} = 4^o$C.

discussed above. Thus, relaxation rates of fluorine in this frequency region are accounted for in terms of dynamic models included in equation 4.3 ($\geq 400$ kHz), and we report the best fit parameters in Table 4.2. The two processes (R and CF) involved to interpret proton data, are found to be inadequate to simulate the fluorine results in the WC regime, its dispersion in the low frequency region thus necessitating the presence of yet another slow process with a qualitatively different frequency dependence. The additional mechanism is a manifestation of the effect of rotational diffusion of locally ordered structures, which produces slow torques coupling to the angular momentum components of the molecules. The spin-relaxation process in the present case is able to probe this dynamics *via* spin-rotation interaction. The time scale $\tau_C$ of this process is in the range of 260 - 300 ns (Table 4.2), and is practically unaffected by temperature within the errors of estimation. The general trend of the increasing strength of the coupling of molecules with the local structures ($A_C$ in the Table 4.2), as the sample is heated away from the transition point, is seen as a possible reflection of the decreasing attenuating effect of competing critical fluctuations involving relatively longer range nematic clusters, especially in view of practically constant $\tau_C$ in this temperature range. The insensitivity of proton to this dynamics is understood as due to its relatively smaller spin-rotation constant (the spin rotation constant ($C$) of proton in a simple liquid like HF being about 5 times less compared to fluorine [17]), and hence substantially less coupling to the lattice ($\sim C^2$). The contributions $A_{1FR}$ and $A_{FCF}$ shown in the Table 4.2 represent the coupling of the fluorine system to the lattice *via* the hetero-nuclear dipolar interaction with protons, arising due to different time modulations.

The analysis of the data in the SC limit (typically below 400 kHz in the present sample) qualitatively differs from above. We find that the extrapolations from the fitted dynamic model (determined by the high frequency dispersion) deviate substantially, and systematically, from the experimental observations (Figure 4.3). The additional contribution, which makes the experimental data much higher than the predictions from dynamics assigned

in the WC regime, comes from the overlap of the two resonance lines. From NMR point of view, as one moves from the WC to SC regime, the so-called flip-flop terms (term $B$ in the dipolar interaction Hamiltonian [14]) begin to contribute via mechanisms which conserve the total energy of the two spins during the low field FCNMR cycle (different from non-conserving flip-flops in the WC regime), - succinctly described as the *like* spins. Of course during the detection cycle the two resonance lines are again well separated and the experiment is fortuitously monitoring the remnant fluorine magnetization only. Thus the additional loss of fluorine magnetization *via* this energy conserving flip-flop interaction with proton system in the SC regime (during the evolution cycle of the experiment) is thus seen as an additional mechanism for the fluorine spin-lattice relaxation itself (at the time of detection). This process, referred to as cross-relaxation between the two spins ($T_{21}$) has been dealt with theoretically earlier [27].

In terms of nuclear spin Hamiltonian comprising of the Zeeman term and a perturbing nuclear dipole-dipole interaction, and with the valid assumption of conservation of total energy of the Hamiltonian, the question is connected with finding out the probability of resonant absorption at a given frequency. This in turn inquires into the rate at which the Zeeman and dipolar energies could come into equilibrium. A higher order perturbation calculation is in principle necessary, with repeated operation of the interaction Hamiltonian on the system. This involves operator products of alternating terms comprising of either $A$ and $B$ (secular and pseudo-secular terms in the dipolar interaction) on one hand, and the transition inducing terms ($C$, $D$, $E$, and $F$) on the other. It was simplified [27] with a combination of perturbation calculation for the transition inducing terms and method of moments for the secular terms. The resulting transition probability for the Zeeman energy of a spin to be converted into dipolar energy leads to a characteristic time $T_{21}$, which is intermediate in nature between $T_1$ and $T_2$. This process will become rapidly ineffective if the Zeeman splitting of the spins become larger than the spin-spin (dipolar in our case) coupling among them. Obviously this mechanism becomes effective in the SC regime. This simplified expres-

sion for this pathway which assist the fluorine Zeeman reservoir to exchange energy with dipolar reservoir, assuming specific line shapes for the two NMR lines is given by [27]

$$T_{21}^{-1} = A_{OL} \int \int g_H(\nu') g_F(\nu'') \delta(\nu' - \nu'') d\nu' d\nu'' \tag{4.5}$$

with $A_{OL} = |\langle E_H, E_F | H_{HF}^d | E_H \pm h\nu, E_F \pm h\nu \rangle|^2$.

Here $A_{OL}$ is related to the square of the matrix element of the Hamiltonian involving simultaneous energy-compensating flip flops of the two spin species mediated by the $B$ term.

Recognizing this interesting path whose efficacy is obviously dependent on the overlap integral between the two resonance lines, we tried to interpret the differential contribution (in the SC regime) in terms of this integral ($R_{1OL} = R_{1EXPT} - R_{1F}$) with variable prefactor ($A_{OL}$) and variable line widths of the two nuclei ($\Delta_H$ and $\Delta_F$). We assumed Lorentzian line shapes for both the NMR spectra in this phase. In the Figures 4.14 - 4.17 the total contribution, including this contribution in the SC regime is shown along with the experimental observations. Estimates of the fit parameters of this mechanism are given in Table 4.3. With this additional mechanism it is now possible to account for the dispersion over the entire frequency region. It should be pointed out that in view of the limited number of data points pertaining to this region of overlap (arising from constraints on fast switching of the fields compatible to this high relaxation rates), the data fit can at best be said to demonstrate this interesting mechanism that comes into play in the FCNMR experiment. The values of the fit parameters are therefore expected to provide perhaps reasonable order-of-magnitude estimates. The contributions from the dynamical models and from the overlap integral are plotted separately at a temperature close to the transition, as shown in Figure 4.18.

The experimental results indicate that the deviations from the predictions of dynamic models in the low frequency region occur at progressively higher

frequencies as the transition temperature is reached. This is perhaps to be expected as the lines broaden as the transition temperature is reached due to pretransitional effects. The data fit suggests that there is a small increase of line width (FWHM) only in the case of fluorine (varying from about 20 to 24 kHz), while proton width remains essentially constant at about 4 kHz, (typical for wide line proton NMR resonance lines in the isotropic phase of liquid crystals). It may be pointed out that the values of these line widths so determined are intrinsic, and are free from the instrument artifacts (like, apparent line width values due to field inhomogenieties), since the observations pertain to dipolar interactions between nuclei residing on the same molecule. The experimentally measured values of these widths, which include contributions from field and sample inhomogenieties as well, are found to be about 45 kHz ($^{19}F$) and 16 kHz ($^{1}H$). These values are consistent with the fit (intrinsic line width) by introducing identical data, measurement artifact for both the nuclei, as is to be expected. Finally, relatively higher line widths of fluorine ($\sim$ 20 kHz, relative to 4 kHz of proton) is also supportive of strong contribution of $J^0(0)$ at the site of fluorine, signalling its sensitivity to a very slow molecular process, which we identify here as the SRLS.

While the fluorine relaxation is seen to be profoundly affected by the introduction of the homo-nuclear component in its dipolar coupling with proton in the SC regime, such is not the case with protons  this mechanism does not lead to discernible additional contribution in this limit. This is understood, keeping in view that there are several protons residing on the molecule having homo-nuclear dipolar interaction all through the dispersion regime, and hence addition of one more such coupling with fluorine is not experimentally making an observable difference.

The variation with temperature of the fluorine relaxation rate at a few frequencies is shown in Figure 4.7. Focusing on the data in the isotropic phase, we note that the relaxation rate is practically constant at 10 and 1 MHz, while there is a curious variation at 0.2 MHz. This frequency falls in

the SC limit where both dynamic processes as per equation 4.2 as well as the cross-relaxation mechanism are operative. Since the angular momentum correlation times increase with increase in temperature (as opposed to reorientational correlations) the occurrence of such a relaxation rate maximum, and its possible shift on temperature axes with changes in Larmor frequency (due to possibly thermally activated rotation with temperature of the underlying time scale $\tau_C$) are known and expected in favorable cases [28]. Such an interpretation to the observed maximum with temperature at this low frequency is however difficult to sustain because the relaxation rate is not entirely due to spin-rotation interaction contribution, and is contaminated with a temperature dependent overlap contribution. A simple argument assigning the maximum as due to the maximal coupling of the spin system to the lattice (brought about by a time scale in the system matching with the employed Lamor frequency) would have led to, in principle, a very slow characteristic time of the order of about 900 ns (satisfying $\omega\tau \simeq 1$ ). But this inference at best can be considered as yet another indication of a slow mode in this phase of the system, confirming perhaps the order-of-magnitude of the time scale of the underlying dynamics extracted from the dynamic models as applied to the high frequency data.

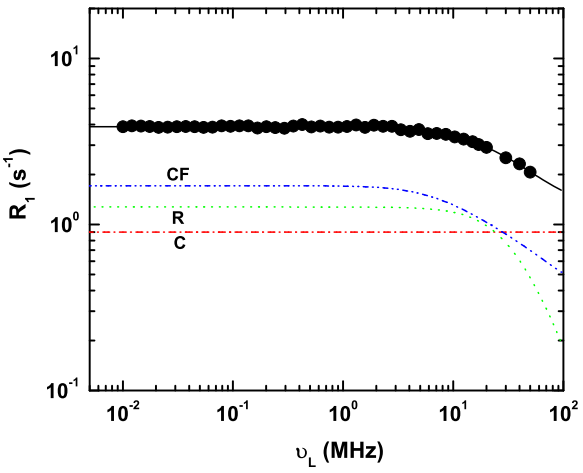


Figure 4.13: Proton spin-lattice relaxation rate dispersion of Sample 1 plotted against Larmor frequency is fitted to equation 4.1 at $\Delta T_{NI} = 11^{o}$C.

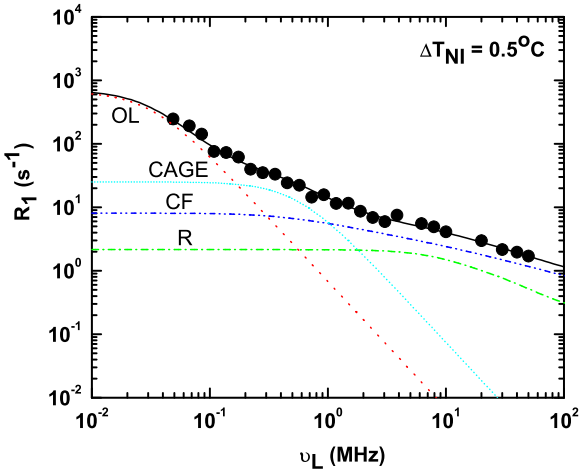


Figure 4.14: Fluorine spin-lattice relaxation rate dispersion of Sample 1 plotted against Larmor frequency is fitted to equation 4.2 $\Delta T_{NI} = 0.5^{o}$C.

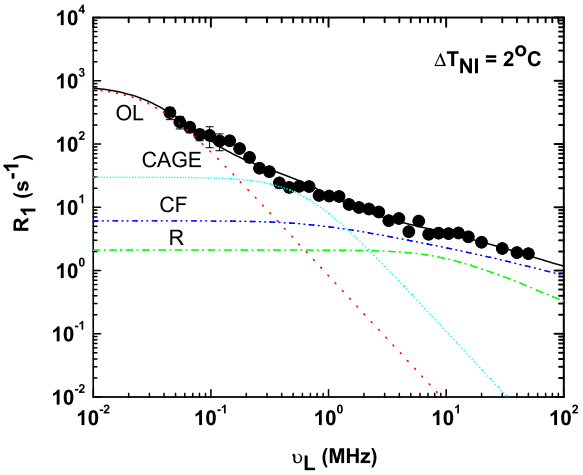


Figure 4.15: Fluorine spin-lattice relaxation rate dispersion of Sample 1 plotted against Larmor frequency is fitted to equation 4.2 $\Delta T_{NI} = 2^{o}$C.

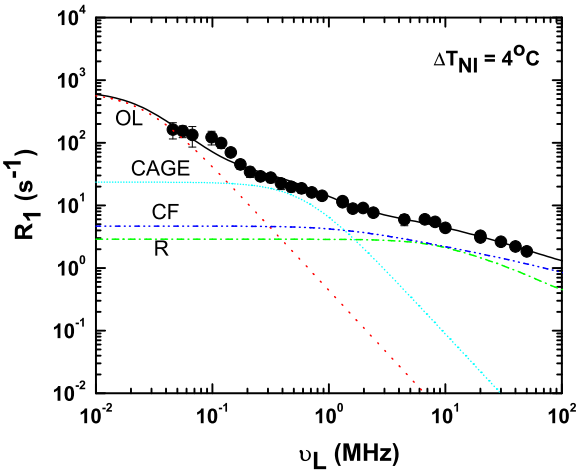


Figure 4.16: Fluorine spin-lattice relaxation rate dispersion of Sample 1 plotted against Larmor frequency is fitted to equation 4.2 $\Delta T_{NI} = 4^{o}$C.

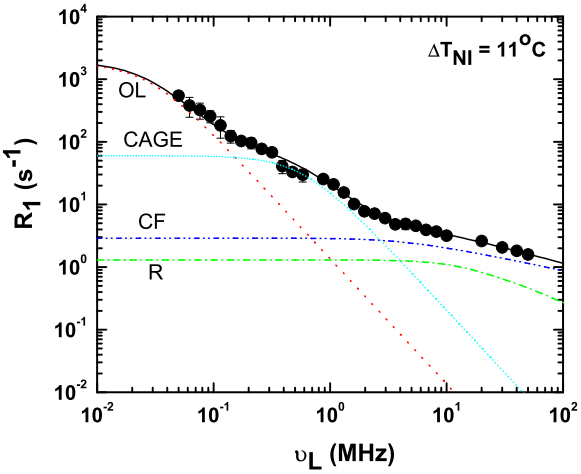


Figure 4.17: Fluorine spin-lattice relaxation rate dispersion of Sample 1 plotted against Larmor frequency is fitted to equation 4.2 $\Delta T_{NI} = 11^{o}$C.

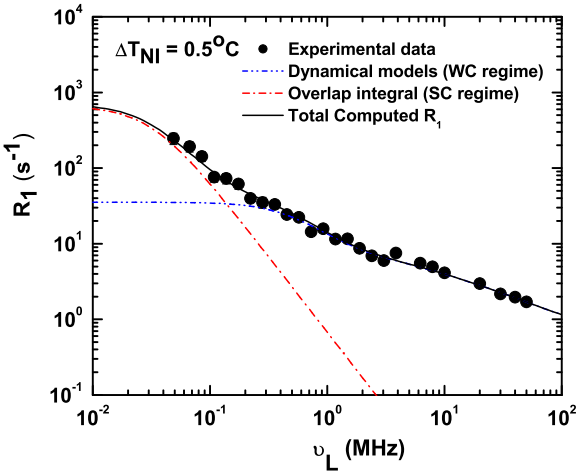


Figure 4.18: Fluorine Spin-lattice relaxation rate of Sample 1 from dynamical models and cross-relaxation (overlap integral) at $\Delta T_{NI} = 0.5^{o}$C.

Table 4.1: Parameters extracted by fitting the $^{1}$H dispersions to equation. 4.1.

| $\Delta$T $^{o}$C | $R_{1H0}$ $s^{-1}$ | $A_{1HR}$ $10^{9}$ $s^{-2}$ | $\tau_R$ ns | $A_{HCF}$ $10^{3}$ $s^{-3/2}$ | $\tau_{CF}$ ns |
|---|---|---|---|---|---|
| 0.5 | 0.61 ± 0.01 | 0.8 ± 0.02 | 3.96 ± 0.07 | 18.75 ± 4.37 | 362.85 ± 10.74 |
| 2 | 0.68 ± 0.01 | 0.87 ± 0.03 | 3.51 ± 0.07 | 18.1 ± 6.05 | 203.02 ± 7.42 |
| 4 | 0.7 ± 0.008 | 0.79 ± 0.01 | 3.49 ± 0.06 | 17 ± 2.53 | 110.68 ± 1.77 |
| 11 | 0.9 ± 0.006 | 0.54 ± 0.16 | 2.38 ± 0.25 | 12.93 ± 3.04 | 35.06 ± 6.26 |

Table 4.2: Parameters extracted by fitting the $^{19}$F dispersions to equation 4.3.

| $\Delta$T $^{o}$C | $A_{1FR}$ $10^{9}$ $s^{-2}$ | $\tau_R$ ns | $A_{FCF}$ $10^{3}$ $s^{-3/2}$ | $\tau_{CF}$ ns | $A_{FC}$ $10^{8}$ $s^{-2}$ | $\tau_C$ ns |
|---|---|---|---|---|---|---|
| 0.5 | 0.41 ± 0.11 | 3.96 | 14.22 ± 1.85 | 362.8 | 0.09 ± 0.009 | 292.24 ± 61.89 |
| 2 | 0.45 ± 0.008 | 3.51 | 14.36 ± 0.13 | 203 | 0.11 ± 0.006 | 261.86 ± 29.06 |
| 4 | 0.62 ± 0.008 | 3.49 | 15 ± 0.14 | 110.7 | 0.09 ± 0.006 | 260.14 ± 33.45 |
| 11 | 0.41 ± 0.19 | 2.38 | 16.39 ± 3.64 | 35.1 | 0.22 ± 0.01 | 272.99 ± 26.53 |

Table 4.3: Parameters extracted by fitting overlap integral.

| $\Delta$T $^{o}$C | $A_{OL}$ $10^{13}$ | $\Delta_F$ kHz ($^{19}F$) | $\Delta_H$ kHz ($^{1}H$) |
|---|---|---|---|
| 0.5 | 7.2 | 24 | 4 |
| 2 | 8.8 | 24.4 | 4 |
| 4 | 4.9 | 20.6 | 4 |
| 11 | 13.9 | 20 | 4 |

### 4.4.2 Sample 2

We now present relaxation dispersion results on Sample 2 (4OTOLFo). We find on one hand that the observations support the general conclusions drawn in the previous section on slow processes from fluorine data. On the other, the analysis of this data presents certain interesting differences in the dynamic processes of the two samples.

The proton relaxation dispersion at three temperatures in the isotropic phase are analyzed based on equation 4.1 using a non-linear least squares method [24] and the fits are shown in Figures 4.19 - 4.21. The spin-lattice relaxation at $11^oC$ away from $T_{NI}$ is well described by individual molecular reorientations and constant background coming from other fast processes. At $\Delta T_{NI} = 1$ and $4^oC$, the dispersions are fitted with molecular reorientations (R) and orientational order critical fluctuations (CF) arising from the dynamic organization of nematic clusters within the isotropic phase. The reorientational correlation times in 4OTOLFo are small compared to the other fluorinated liquid crystal systems 4OFTOL (Sample 1) and 4OTOLFm (Sample 3) [19]. In the case of sample 1, the reorientational correlation time $\tau_R$ is 2.4 ns at $11^oC$ away from the transition and it increases to 4 ns as the temperature cools down to $0.5^oC$ away from $T_{NI}$ [29], whereas in the case of 4OTOLFm, this is varying from 1.67 to 1.39 ns in a comparable temperature range of our study [19]. The correlation times of critical fluctuations are comparable with those of 4OTOLFm but are small compared to 4OFTOL (sample 1). Such order fluctuations are not in evidence at temperatures far away from $T_{NI}$ in this compound. The activation energy associated with the rotational diffusion in this system is small compared to the other two compounds (Sample 1 and Sample 3), and the energies are 2.5, 7.5 and 20.8 kJ for 4OTOLFo, 4OTOLFm and 4OFTOL, respectively. The only difference in these three compounds is the location of fluorine atom on the aromatic cores (molecular structures of these compounds are given in Figure 4.1), and Sample 2 is reported to be monotropic [6]. The temperature dependent data

at different Larmor frequencies shown in Figure 4.8 support the presence of contribution of critical fluctuations as the transition is approached from the above.

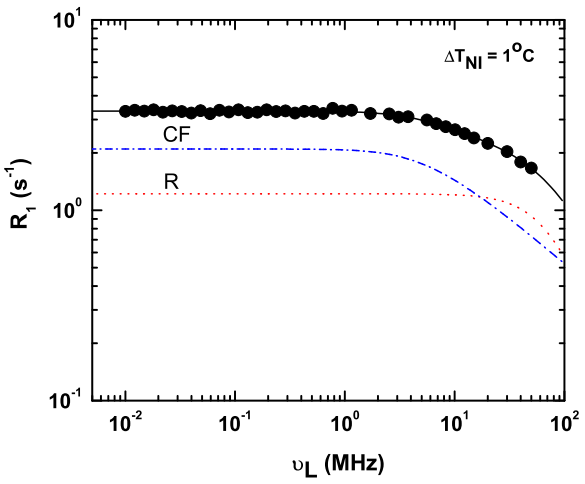


Figure 4.19: Proton spin-lattice relaxation rate dispersion of Sample 2 plotted against Larmor frequency is fitted to equation 4.1 at $\Delta T_{NI} = 1^o$C.

The fluorine dispersion data in the weak-coupling limit are analyzed using equation 4.3. The correlation times $\tau_R$ and $\tau_{CF}$ determined from the proton fits are taken as inputs in the fluorine analysis. The dynamic processes described for proton dispersions are inadequate to explain the fluorine dispersion data and these dispersions clearly indicate the existence of another slower process which could explain the observed relaxation rate increase in the WC regime. Thus we proceed with the analysis of this data on similar lines as the previous sample. The time scale $\tau_C$ of this process is in the range of 230 -280 ns (Table 4.5), and is practically unaffected by temperature within the errors of estimation. The insensitivity of proton to this dynamics is explained earlier in the case of Sample 1. The contributions $A_{1FR}$ and $A_{FCF}$ shown in the Table 4.5 represent the coupling of the fluorine system to the lattice via the hetero-nuclear dipolar interaction with protons, arising

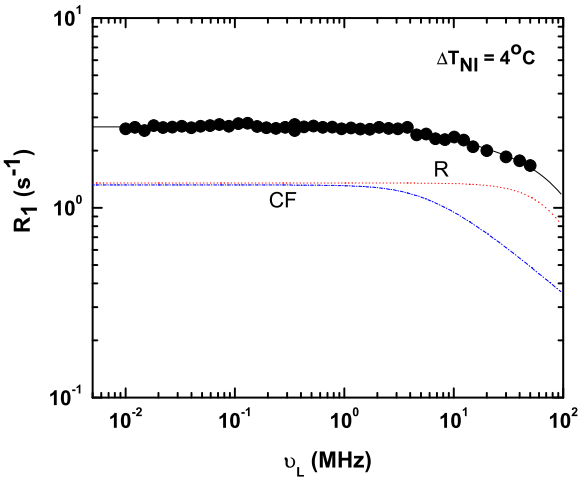


Figure 4.20: Proton spin-lattice relaxation rate dispersion of Sample 2 plotted against Larmor frequency is fitted to equation 4.1 at $\Delta T_{NI} = 4^{o}$C.

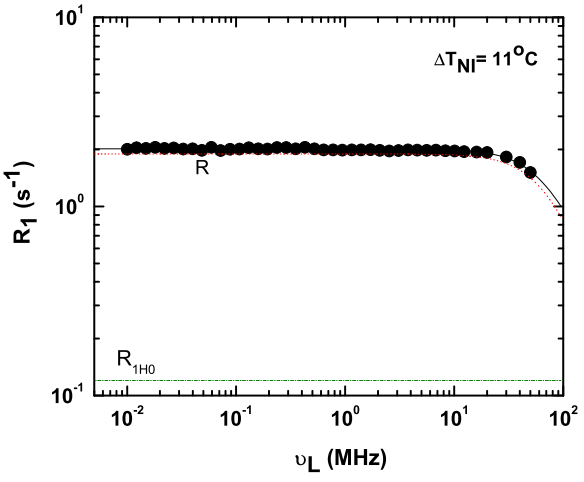


Figure 4.21: Proton spin-lattice relaxation rate dispersion of Sample 2 plotted against Larmor frequency is fitted to equation 4.1 at $\Delta T_{NI} = 11^{o}$C.

due to different types of time modulations.

The data in the strong-coupling limit, not accounted fully by the above dynamical models, are again interpreted with contribution arising out of the overlap of the two resonance lines ($R_{1OL} = R_{1EXPT} - R_{1F}$) with variable prefactor ($A_{OL}$) and variable line widths for both the nuclei ($\Delta_H$ and $\Delta_F$). Figures 4.22 - 4.24 show the total contribution to the relaxation rate coming from dynamic models as well as the cross-relaxation contribution (estimated by the overlap integral) in the SC regime, along with the experimental observations. Estimates of the fit parameters of this mechanism are given in Table 4.6. The line widths obtained from the fit are 4 kHz and 40 kHz for proton and fluorine, respectively. When compared with sample 1, the line width obtained for fluorine nuclei for this sample is higher and is not varying with temperature.

Figure 4.9 shows the temperature dependent spin-lattice relaxation data of fluorine at different Larmor frequencies. This compound also shows that the relaxation rate is independent of temperature at 10 MHz. At 1 and 0.2 MHz the relaxation rate shows two maxima within the temperature range of our study. In view of the discussion presented in the case of Sample 1, dealing with qualitatively different contributions to the relaxation rate at these frequencies, (*viz.* temperature dependent spin-rotation interaction contribution and cross relaxation contribution due to overlap of lines), it is difficult to assign and interpret these observed temperature dependent extrema. At the least, it can be concluded that there are slow enough processes in the sample leading to $R_1$ maxima even at these low resonance frequencies.

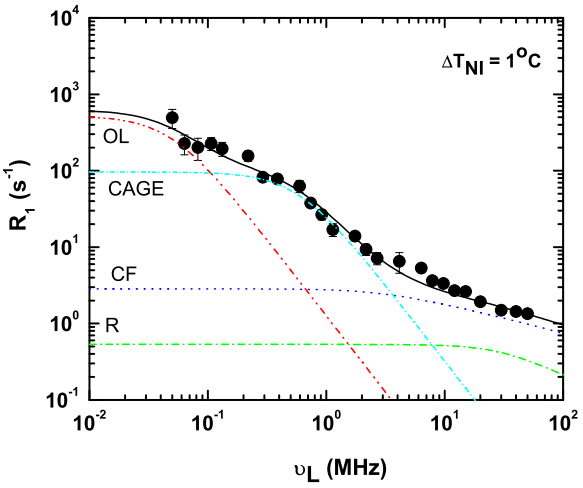


Figure 4.22: Fluorine spin-lattice relaxation rate dispersion of Sample 2 plotted against Larmor frequency is fitted to equation 4.2 at $\Delta T_{NI} = 1^o$C.

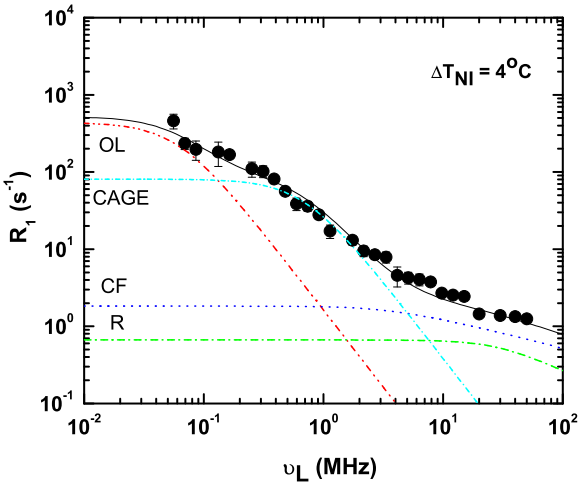


Figure 4.23: Fluorine spin-lattice relaxation rate dispersion of Sample 2 plotted against Larmor frequency is fitted to equation 4.2 at $\Delta T_{NI} = 4^o$C.

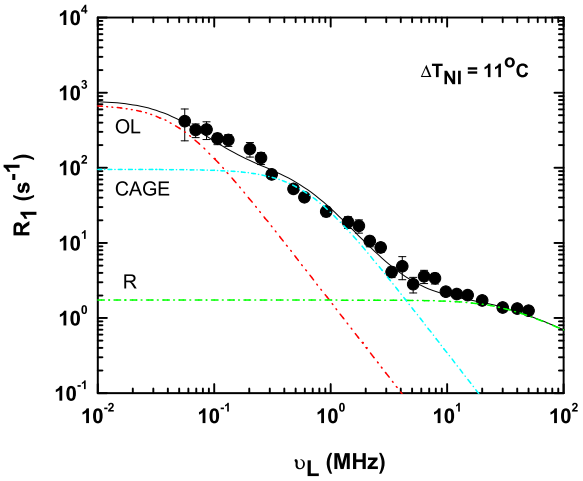


Figure 4.24: Fluorine spin-lattice relaxation rate dispersion of Sample 2 plotted against Larmor frequency is fitted to equation 4.2 at $\Delta T_{NI} = 11^{o}$C.

Table 4.4: Parameters extracted by fitting the $^{1}$H dispersions of Sample 2 to equation. 4.1.

| $\Delta$T $^{o}$C | $R_{1H0}$ $s^{-1}$ | $A_{1HR}$ $10^{9}$ $s^{-2}$ | $\tau_R$ ns | $A_{HCF}$ $10^{3}$ $s^{-3/2}$ | $\tau_{CF}$ ns |
|---|---|---|---|---|---|
| 1 | – | 1.24 ± 0.11 | 0.98 ± 0.11 | 13.35 ± 2.16 | 49.40 ± 7.17 |
| 4 | – | 1.52 ± 0.1 | 0.75 ± 0.15 | 11.62 ± 2.79 | 34.03 ± 6.03 |
| 11 | 0.12 ± 0.05 | 1.85 ± 0.04 | 1.02 ± 0.02 | – | – |

Table 4.5: Parameters extracted by fitting the $^{19}$F dispersions of Sample 2 to equation 4.3.

| $\Delta$T $^{o}$C | $A_{1FR}$ $10^{9}$ $s^{-2}$ | $\tau_R$ ns | $A_{FCF}$ $10^{3}$ $s^{-3/2}$ | $\tau_{CF}$ ns | $A_{FC}$ $10^{8}$ $s^{-2}$ | $\tau_C$ ns |
|---|---|---|---|---|---|---|
| 1 | 0.4 ± 0.02 | 1 | 13.53 ± 0.13 | 49.5 | 0.35 ± 0.02 | 275.15 ± 28.74 |
| 4 | 0.5 ± 0.01 | 1 | 9.57 ± 0.13 | 34 | 0.35 ± 0.02 | 233.5 ± 22.07 |
| 11 | 1.30 ± 0.01 | 1 | – | – | 0.36 ± 0.02 | 263.65 ± 24.97 |

Table 4.6: Parameters extracted by fitting overlap integral (Sample 2).

| $\Delta$T $^o$C | A$_{OL}$ $10^{13}$ | $\Delta_F$ kHz ($^{19}F$) | $\Delta_H$ kHz ($^1H$) |
|---|---|---|---|
| 1 | 14.1 | 39.2 | 4 |
| 4 | 18.6 | 40 | 4 |
| 11 | 18.5 | 39 | 4 |

## 4.5 Conclusions

The present study attempts to interpret qualitatively different spin-lattice relaxation dispersions of two very similar nuclei with close gyromagnetic ratios ( $\gamma_H \approx \gamma_F$, within 6 %) in the isotropic phase of two liquid crystals. While there are a large number protons ($^1H$) residing on the liquid crystal molecule, a lone member ($^{19}F$) is attached to the aromatic core of the molecule. The latter has limited access to the lattice via the usual dipolar interaction terms due to the dissimilar $\gamma$'s (*unlike* spins) in the high frequency region of the experiment (*i.e.*, the so-called weak-coupling limit), and hence its observed significant coupling to lattice modes, as well as its discernible dispersion, calls for a mechanism which depends on a specific interaction unique to this species, *viz.*, the relatively strong spin-rotation. This mechanism however samples time correlations of molecular angular momentum components rather than reorientations which couple to the dipolar terms. Thus the chosen systems are in a fortuitous circumstance of sampling two types of correlations of the dynamic processes of the system, and the present work is concerned with the interpretation of the experimental data recognizing this distinction. The FCNMR experiment also allows an effective contact of the fluorine system with protons (despite their differing $\gamma$'s ) at low enough frequencies. In this regime, called the strong-coupling limit, the hetero-nuclear coupling acquires an effective homo-nuclear component due to overlap of the resonance lines, and the spin-lattice relaxation of the fluorine is now aided by this coupling, proportional to the degree of overlap. Due to the inherent effective coupling

among protons over the entire region (in the sense of wide NMR experiment) the onset of this additional mechanism is not detectable from proton data. The differing temperature dependences of the relaxation rates of the two nuclear systems clearly indicate the presence of two distinct slow underlying molecular processes, experienced by the same molecule but reported differently by the two participating probes. In that sense this is an interesting attempt to use two nuclear probes on the molecule to examine the dynamics through the dispersion study of respective nuclear spin-lattice relaxation rates. This experiment essentially translates to mapping of spectral densities of the time correlation functions of distinct processes modulating different lattice-coupling mechanisms. The slowly relaxing local structures involved in this study to interpret fluorine relaxation data were proposed, and convincingly confirmed, by detailed ESR experiments earlier [21–23]. The present FCNMR experiments provide perhaps the first evidence of such slow modes, with a direct mapping of their representative spectral density. Finally, a comment may be made on an interesting feature of this measurement. Within the same FCNMR experiment, the evolution cycle (particularly in the strong-coupling limit) allows the flip-flop terms (term B in the dipolar interaction) to more readily exchange the magnetization between the two spin systems (making the interaction to assume a pseudo-secular character expected of *like* spins), while in the detection cycle with well separated resonance lines such changes in the fluorine magnetization (occurred during the evolution cycle) are now perceived as irreversible losses to the lattice, - contributing thus to its detectable spin-lattice relaxation rate.

# References

[1] Carmen Catanescu, L. C. Chien, Shin-Tson Wu, Mol. Cryst. Liq. Cryst. **411**, 93 (2007).

[2] Yung-Ming Liao, Narayana swamy Janarthanan, Chain-Shu Hsu, Sebastian Gauza, Shin-Tson Wu, Liq. Cryst. **33**, 1199 (2006).

[3] S. Gauza, S. Wu, A. Spadlo, and R. Dabrowski, J. Display Technology **2**, 247 (2006).

[4] S. Gauza, C. Wen, Y. Zhao, S. Wu, A. Ziolek, and R. Dabrowski, Mol. Cryst. Liq. Cryst. **453**, 215 (2006).

[5] S. Gauza, J. Li, S. Wu, A. Spadlo, R. Dabrowski, Y. Tzeng, and K. Cheng, Liq. Cryst. **32**, 1077 (2005).

[6] J. Czub, S. Urban, R. Dabrowski, and B. Gestblom, Acta Physica Polonica A **107**, 947 (2005).

[7] J. Li, S. Gauza, and S. Wu, Optics Express 12, 2002 (2004).

[8] D. Demus, Y. Goto, S. Sawada, E. Nakagawa, H. Saito, R. Tarana, Mol. Cryst. Liq. Cryst. **260**, 1 (1995).

[9] Il-Kook Huh, Yong-Bae Kim, Liq. Cryst. 29, 1265 (2002).

[10] A. Spadlo, R. Dabrowski, M. Filipowicz, Z. Stolarz, J. Przedmojski, S. Gauza, C. Y. Fan, S.T. Wu, Liq. Cryst. **30**, 191 (2003).

[11] A. Spadlo, J. Dziaduszek, R. Dabrowski, K. Czuprynski, Shin-Tson Wu, SPIE, **4759**, 79 (2002).

[12] R. Y. Dong, *Nuclear Magnetic Resonance of Liquid Crystals*, Springer-Verlag (1997).

[13] R. Y. Dong, *Nuclear Magnetic Resonance spectroscopy of Liquid Crystals*, World Scientific, Singapore (2009).

[14] A. Abragam, *The Principles of Nuclear Magnetism, Clarendon Press*, Oxford (1961).

[15] P. S. Hubbard, Phys. Rev. **131**, 1155 (1963).

[16] D. K. Green and J. G. Powles, Proc. Phys. Soc. **85**, 87 (1965).

[17] H. S. Gutowsky, I. J. Lawrenson, and K. Shimomura, Phys. Rev. Lett. **6**, 349 (1961).

[18] R. J. C. Brown, H. S. Gutowsky, and K. Shimomura, J. Chem. Phys. **38**, 76 (1963).

[19] M. TrivikramRao, M. Rajeswari, K. Venu and V.S.S. Sastry, and R. Dabrowski (communicated to Phys. Rev. E, 2011).

[20] J. H. Freed, J. Chem. Phys. **66**, 4183 (1977).

[21] J. H. Freed, A. Nayeem, and S. B. Rananavare, *The Molecular Dynamics of Liquid crystals*, Edited by G.R. Luckhurst, and C. A. Veracini, (Kluwer, 1994), Chap.4; J. H. Freed, A. Nayeem, and S. B. Rananavare, ibid., Chap.5 and references therein.

[22] V. S. S. Sastry, A. Polimeno, R. H. Crepeau, and J. H. Freed, J. Chem. Phys. **105**, 5753, (1996).

[23] V. S. S. Sastry, A. Polimeno, R. H. Crepeau, and J. H. Freed, J. Chem. Phys. **105**, 5773, (1996).

[24] W. H. press, B. P. Flennery, S. A. Teukolsky, W. T. Vetterling, *Numerical Recipes, the art of scientific computation*, Cambridge University press, Cambridge (1986).

[25] M. Rajeswari, S. Dhara, K. Venu, V. S. S. Sastry, R. Dabrowski, to be appear in Mol. Cryst. Liq. Cryst. (2011).

[26] M. Trivikram Rao, Ph.D Thesis, University of Hyderabad (2008).

[27] N. Bloembergen, S. Shapiro, P. S. Pershan, J. O. Artman, Phys. Rev. **114**, 445 (1959).

[28] F. Koksal and S. Bahceli, J. Chem. Soc. Faraday II, **74**, 1844 (1978).

[29] M. Rajeswari, Trivikram R. Molugu, Surajit Dhara, K. Venu and V. S. S. Sastry, and R. Dabrowski (communicated to J. Chem. Phys, 2011).

# 5

# NMR relaxometry study of a liquid crystal 8OCB confined to random porous networks formed by aerosil particles

## 5.1 Introduction

Study of quenched random disorder effects on liquid crystalline properties were explored earlier through various experimental techniques [1] like calorimetry [2], X-ray scattering and intensity fluctuations [2, 3], dielectric spectroscopy [4, 5], proton and deuteron nuclear magnetic resonance (DNMR) [6–9] and optical anisotropy measurements [10]. Liquid crystal (LC)-aerosil systems are of great importance because the random disorder can be introduced in a controlled manner unlike the other random porous matrices like aerogel [11], CPG [12–14] and anopore [15] etc. When the nano-size particles are introduced into the LC system, they induce local ordering near the surfaces, and hence the potential to interfere with the long-range orientational order in the medium. This has a profound effect on the correlations in the nematic order in different mesophases, and in particular on the dynamic organization

of molecules in the isotropic phase in the vicinity of the I-N transition. This effect is more pronounced more the density of the silica particles in the system is.

The surface of aerosil particles used in the experiments is covered with hydroxyl groups that tend to form hydrogen bond with each other. At low densities $\rho_s < 0.01$ g/cm$^3$ (here after we drop the units for convenience), the number of particles are too small to form a network and they act as impurities added to the LC. As the concentration increases above the gelation threshold, with $\rho_s$ ranging from 0.01 to 0.1, the silica spheres are able to form a network, known as soft gel. If the concentration increases beyond 0.1, the network becomes more rigid and this dispersion is known as stiff gel. By the addition of aerosil particles in a controlled manner the silica density can be suitably calibrated as to the LC system from no-gel to soft-gel to the stiff-gel regime. The earlier proton NMR measurements were carried out in the high temperature phase above the isotropic-nematic transition [6]. Here, the objective of the present work is to see the effect of confinement on spin-lattice relaxation rate in the isotropic as well as in low temperature mesophases where the long-range orientational order is seriously affected with the addition of silica particles, as quenched random disorder is introduced in liquid crystalline phases. This effect was explored in detail earlier in 8CB-aerosil mixtures with DNMR experiments in all the phases [8, 9] and in many other liquid crystals using calorimetric technique [16, 17].

In this context, we report on the results of our studies on two liquid crystal systems, 4′-octyloxy-4-cyanobiphenyl (8OCB) and 4-propyl-4′-pentylazoxy benzene (PPA) embedded in an aerosil matrix forming a 3-d random network. These two systems are chosen for their contrasting differences: the 8OCB molecules host electrical dipoles essentially parallel to their long axis, while PPA molecules have dipoles in a plane perpendicular to the long axis. The host matrix in the two cases being maintained the same, these two systems may provide interesting points of comparison originating from the

location of the dipoles and consequent manifestation. With this objective we carried out detailed investigations on these two systems, encompassing their mesophases. In this chapter we present the work on 8OCB. Thus our focus is on the frequency dispersion of proton spin-lattice relaxation rates of this bulk liquid crystal and when it is confined to random network formed by the silica particles at two different concentrations. Such a dispersion profile provides an insight, and reasonable quantitative estimates, of the underlying characteristic molecular processes in such complex environments. The confinement introduces slow reorientational correlations near the surface in the presence of significant adsorption, and these occur in the kHz frequency regime. Application of FCNMR methods to investigate dynamics on this time scale is known, and comprehensively reviewed recently [18].

## 5.2 Experimental details

The liquid crystal (LC)-aerosil mixtures are prepared using the solvent method [2]. The liquid crystal 8OCB under study was synthesized in the laboratory of Prof. R. Dabrowski in Warsaw, Poland. The molecular structure and its phase sequence are shown in Figure 5.1. The preparation details of LC-aerosil mixtures were explained in Chapter 3. Aerosil (A300) consists of small silica spheres of 7 nm in diameter and has a specific surface area of 300 $m^2/g$. The surface of the spheres is covered with hydroxyl groups and they interact with each other and form a 3-d network in the LC environment. Because of the hydrophilic nature of the aerosil particles and the polar nature of the LC, the molecules orient homeotropically at the surface. The schematic picture of how aerosil forms a network in liquid crystal environment is shown in Figure 5.2. The density of silica in our samples was 0.05 (Sample A) and 0.07 (Sample B) $g/cm^3$. The average void size formed by the aerosil particles at these concentrations is estimated to be 133 nm and 90 nm, respectively [14]. The shift of the transition temperatures in the presence of confinement is within $\pm$1K at both the concentrations.

Proton spin-lattice relaxation times are measured at different Larmor frequencies using the field-cycling NMR relaxometer from 10 kHz to 10 MHz and the pulsed field-variable spectrometer from 10 MHz to 50 MHz. To measure $T_1$ on the FCNMR relaxometer pre-polarized and non-polarized pulse sequences are used [18, 19]. An inversion recovery sequence is used at higher frequencies. The decay of magnetization has been found to be exponential in our experiments indicating single relaxation time constant. Relative errors in the $T_1$ measurements are within 3% and the temperature of the sample is controlled to within $\pm$0.1K.

Figures 5.3a - 5.3c show the frequency dependence of relaxation rate measurements of bulk 8OCB in different phases and Figures 5.4a - 5.4c and 5.5a - 5.5c show the frequency dispersion of 8OCB confined to aerosil matrix at the two different concentrations. The shapes of the dispersions in the bulk phases are characteristic of the mesophase of the liquid crystal. Dispersions of confined systems clearly show, in each of the mesophases, deviations from the respective bulk profiles with an enhancement of the relaxation rates at the low frequency end. Figures 5.6 - 5.8 show the temperature dependence of relaxation rates at different Larmor frequencies of the bulk and confined samples, bringing out specific features of the different phases in the bulk as well as in confined LC systems.

4'-octyloxy-4-cyanobiphenyl (8OCB)

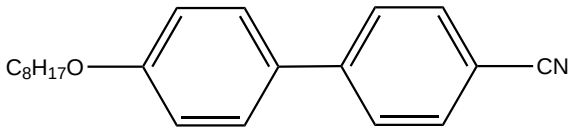


Cr 54.5°C Sm A 67°C N 80°C I

Figure 5.1: Molecular structure and phase sequence of a liquid crystal 8OCB.

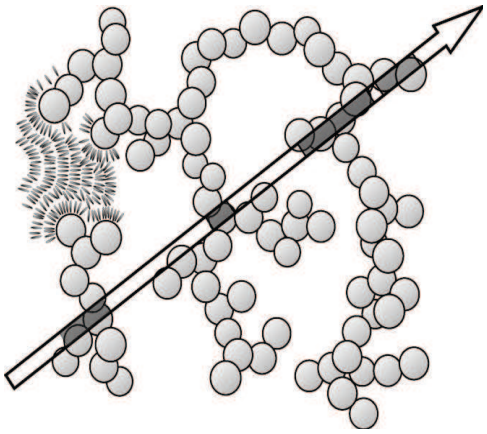

Figure 5.2: Schematic representation of the aerosil network formed by diffusion limited aggregation process, circles represent aerosil particles, "hairs" in the upper left corner represent liquid crystal molecules. Open and shaded parts of arrow show void and solid chords, respectively [14].

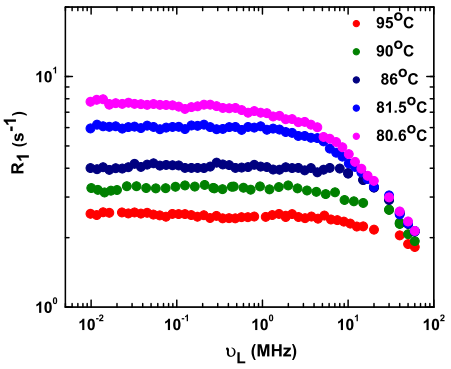


(a)

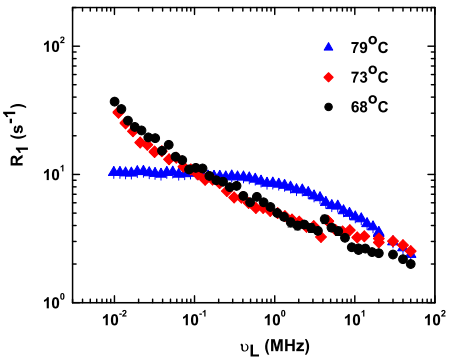


(b)

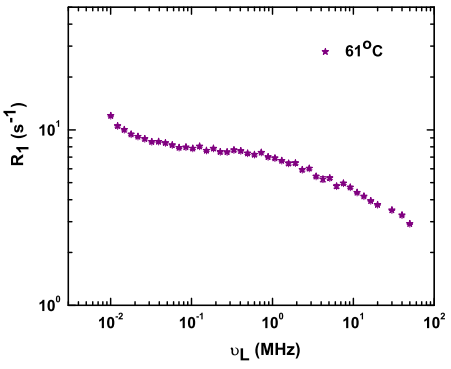


(c)

Figure 5.3: Frequency dispersions of the proton spin-lattice relaxation rate of bulk 8OCB in different phases: (a) Isotropic;(b) Nematic; (c) Smectic.

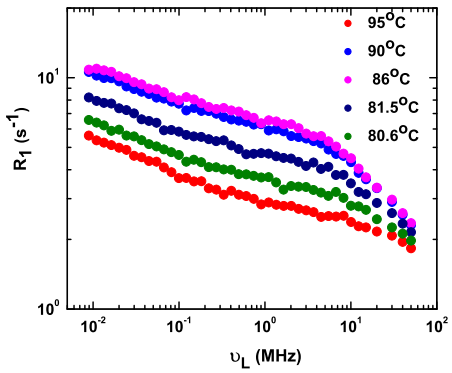


(a)

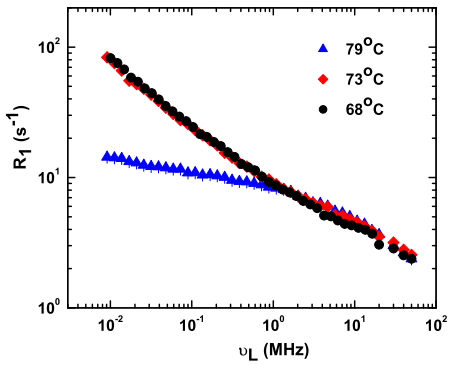


(b)

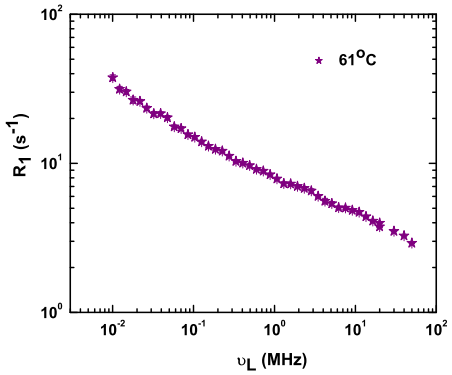


(c)

Figure 5.4: Frequency dispersions of the proton spin-lattice relaxation rate of Sample A in different phases: (a) Isotropic; (b) Nematic; (c) Smectic.

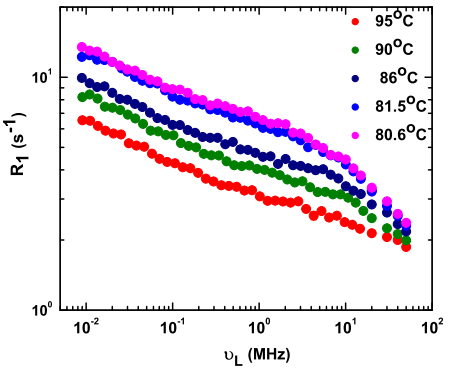


(a)

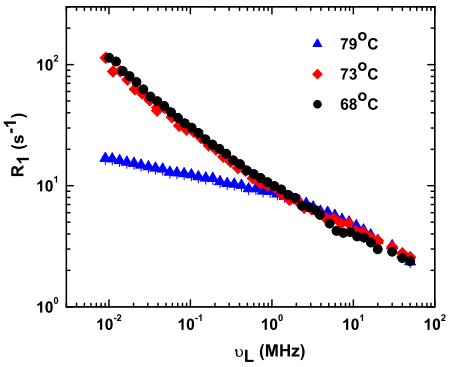


(b)

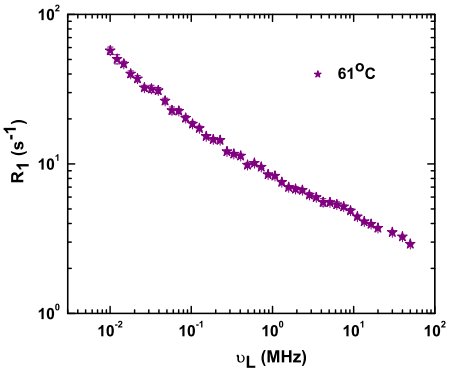


(c)

Figure 5.5: Frequency dispersions of the proton spin-lattice relaxation rate of Sample B in different phases: (a) Isotropic; (b) Nematic; (c) Smectic.

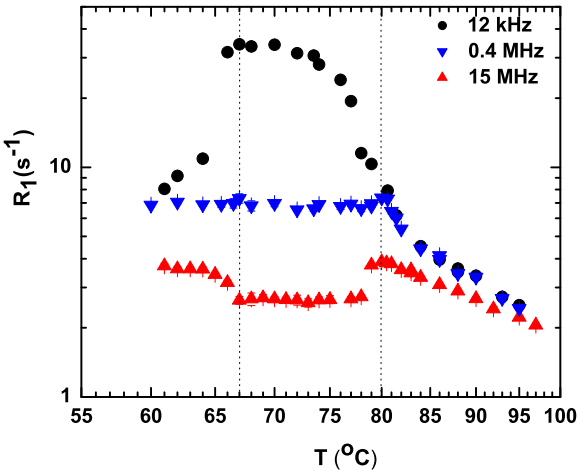


Figure 5.6: Temperature dependence of the proton spin-lattice relaxation rate at three Larmor frequencies in bulk 8OCB.

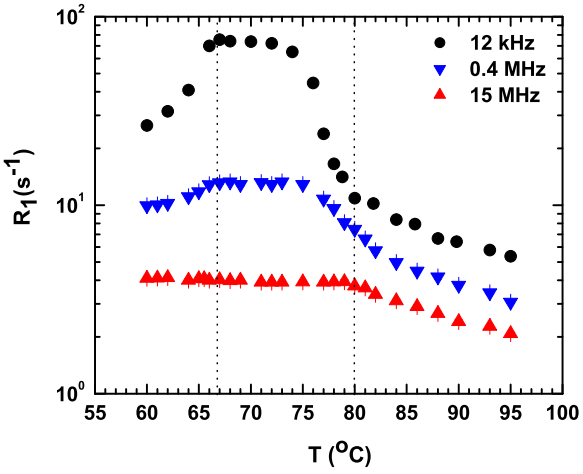


Figure 5.7: Temperature dependence of the proton spin-lattice relaxation rate at three Larmor frequencies in Sample A.

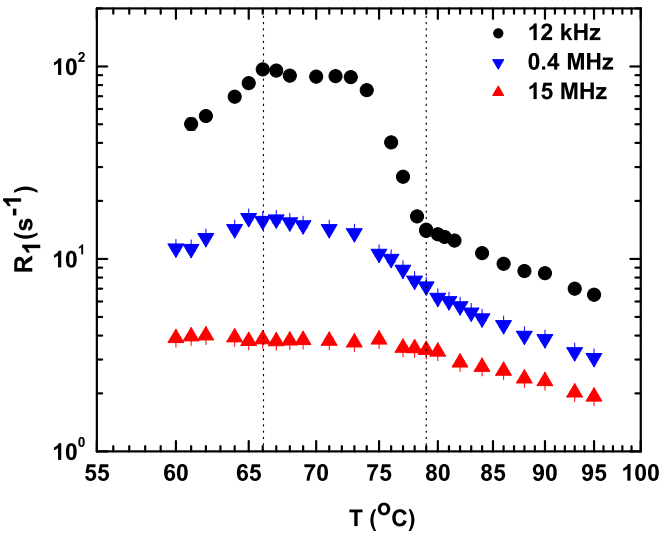


Figure 5.8: Temperature dependence of the proton spin-lattice relaxation rate at three Larmor frequencies in Sample B.

## 5.3 Relaxation models

Spin-lattice relaxation of protons occurs via the time modulation of dipole-dipole interactions between the neighboring spins [20]. The time variation of spin interactions occurs due to molecular reorientations, translational displacements, and collective fluctuations like orientational order critical fluctuations (CF) (pre-transitional effects in the isotropic phase), order parameter fluctuations (OPF) just below I-N transition, order director fluctuations (ODF) in mid nematic phase or layer undulations (LU) in smectic phase etc, for bulk systems [21]. In the case of confined systems, the confinement introduces additional slow reorientational dynamics into the system at the surface layers, and this is reflected in the relaxation measurements as increase in the relaxation rate at low frequencies. This is attributed to a process identified as reorientations mediated by translational displacements (RMTD) [22, 23]. Depending on the mesophase of the liquid crystal, different dynamic processes contribute to the total relaxation. Details of these relaxation models are already discussed in Chapter 2.

## 5.4 Analysis and discussion

### 5.4.1 Isotropic phase

Frequency dispersions of the spin-lattice relaxation profiles of bulk and confined liquid crystal systems above the isotropic-nematic transition $T_{NI}$ are analyzed by considering the following mechanisms: reorientations about the short axes (R), translational self-diffusion (SD), orientational order critical fluctuations near the $T_{NI}$ (CF) and reorientations mediated by translational displacements (RMRD). Therefore the total relaxation rates in bulk ($R_{1B}$) and confined systems ($R_{1C}$) in the isotropic phase are decomposed as

$$R_{1B} = R_{1SD} + R_{1R} + R_{1CF} \tag{5.1}$$

$$R_{1C} = R_{1SD} + R_{1R} + R_{1CF} + R_{IRMTD}. \quad (5.2)$$

The dispersion data at different temperatures are fit to equation (5.1) in the case of bulk sample and to equation (5.2) for confined systems. Non-linear least squares method is used to get the best fit parameters consistent with frequency and temperature dependences. To reduce the complexity in the fitting procedure we have taken diffusion data available from other experiments [24, 25] and so the diffusion coefficient $D$ was not a variable in the analysis. We find that the coupling constant $A_D$ is fairly insensitive to temperature and so we used its average value for all temperatures. The prefactor $A_R$ and the reorientational correlation time $\tau_R$ show temperature dependences as expected in bulk liquid crystals. As we approach the isotropic-nematic transition, the contribution from critical fluctuations becomes significant, and is reflected in the plots in terms of relative contributions of different mechanisms. We find that the $\tau_{CF}$ values of 8OCB (obtained from bulk sample data) are comparable to those in other LC systems, like 4-trans-4′-n-hexyl-cyclohexyl-isothiocyantobenzene (6CHBT) [26]. The fitted curves and parameters are shown in Figures 5.9 - 5.13 and in Table 5.1, respectively. In each of the figures symbols correspond to experimental data, black line represents the calculated curve. Individual contributions are shown as colored lines with appropriate legends.

While analyzing the dispersion profiles of the confined system based on equation (5.2), we take advantage of the knowledge of the dynamic behavior in the bulk sample and hence focus primarily on the RMTD mechanism. Thus the fit parameters in this case pertain to its lower and upper cutoff frequencies ($\omega_{RMTDmin}$ and $\omega_{RMTDmax}$) and the exponent $p$ in the expected power law behavior for the frequency dispersion between these two frequency limits [27]. The resulting fits and the parameters for sample A are shown in Figures 5.14 - 5.18 and in Table 5.2, and those for Sample B are shown in Figures 5.19 - 5.23 and in Table 5.3. We find that the data between the two cutoff

regimes fit to $(T_1^{-1})_{RMTD} \propto \omega^{-p}$, with $p = 0.38 \pm 0.04$, (see Figures 5.14 and 5.19, for example), and this deviates from the equipartition value of 0.5. Equitable distribution of diffusion modes over the wave vector range under consideration assumes no wave vector dependence, *i.e.*, $Q(q) = cq^{-\chi} + e$ with $\chi = 0$ [equation 2.95]. Its value in the isotropic phase in particular reflects the nature of the surface in terms of the associated structure factor. Earlier work in the isotropic phase of 8CB confined in CPG [23] for example yielded this exponent value close to the equipartition value within the experimental error. The present value, below 0.5, is clearly indicative of the 3-d random voids made up a network of silica particles of $\sim$ 7 nm size held together by appropriate hydrogen bonds. With RMTD exclusively originating from adsorption layers near the surface, the surface as a topological 2-d surface seems to be characterized by a predominance of low wave length modes (on a relative scale) yielding a negative value for $\chi$ (= - 0.24). The fact that this value remains essentially the same with Sample B as well, and also with similar experiments with another liquid crystal system (next chapter) but with the same aerosil matrix, further confirms this observation. The cutoff frequencies $\omega_{RMTDmin}$ and $\omega_{RMTDmax}$ are related to the largest and smallest molecular displacements $l_{max}$ and $l_{min}$, respectively, needed to cause appreciable loss of correlation among the orientations of molecules [23]. The estimated value of $l_{max} = 91 \pm 6$ nm does not show significant variation with the temperature, while that of $l_{min}$ shows a substantial change with temperature, increasing rapidly near the I-N transition temperature. This indicates essentially the formation of progressively correlated regions of paranematic order near the surface, as a manifestation of the pretransitional effects. The pretransitional effect on $l_{min}$ is shown in Figure 5.24, and it may be seen that its value at high temperatures (about 1.5 nm) increase to almost 8 - 9 nm very near $T_{NI}$.

The strength of the RMTD interaction $A_{RMTD}$ shows an Arrhenius behavior with temperature at both the concentrations (sample A and sample B) as depicted in Figure 5.25, and it is slightly enhanced in sample B, relative to sample A, presumably due to enhancement of the fraction of molecules in

the surface layer at its lower average void size. The corresponding activation energies at the two concentrations are: $E_a = 35$ kJ/mole for sample A and 41.5 kJ/mole for sample B. The slight increase in the activation energy at the higher concentration could be due to an increased effective polar interaction between aerosil matrix and the liquid crystal molecules at the surface on increasing the silica particle density. We did not find observable variation in the two cutoff frequencies of the two samples. It may also be noted that the $A_R$ and $\tau_R$ (related to molecular reorientation mechanism) in the two samples differ slightly, especially near the transition temperature, reflecting relative changes in the orientational surface ordering in the systems.

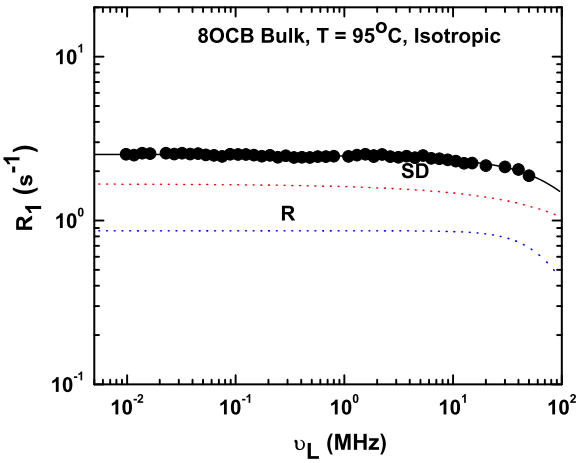


Figure 5.9: Frequency dependence of proton spin-lattice relaxation rate of bulk 8OCB at T = 95$^o$C. The black line is the calculated total relaxation rate obtained by using equation 5.1. Color lines are the corresponding relaxation rate contributions from different mechanisms as shown in the figure.

### 5.4.2 Just below $T_{NI}$

The dispersion profile of spin-lattice relaxation rate ($R_{1B}$) of bulk liquid crystal just below the $T_{NI}$ (at $T = 79^oC$) is analyzed with the following

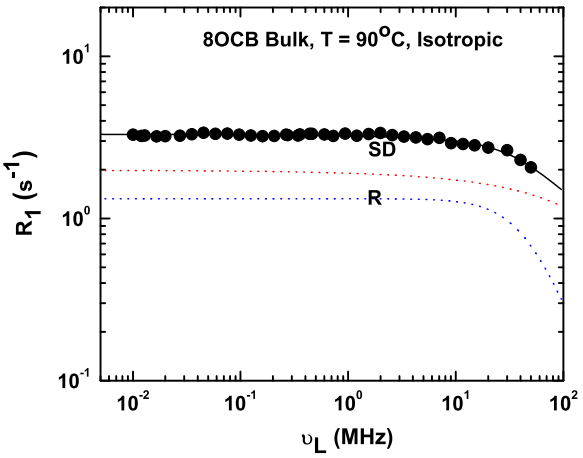


Figure 5.10: Frequency dependence of proton spin-lattice relaxation rate of bulk 8OCB at T = 90$^o$C.

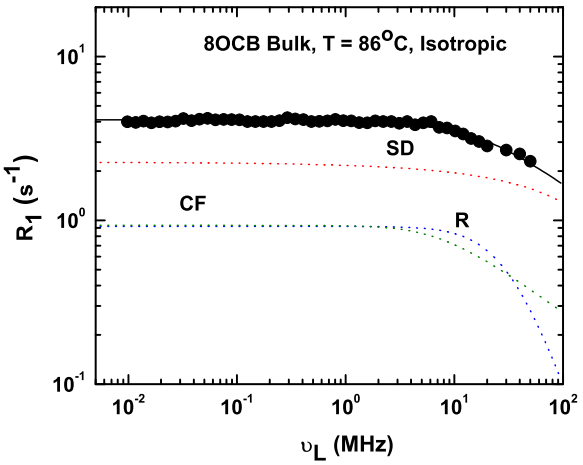


Figure 5.11: Frequency dependence of proton spin-lattice relaxation rate of bulk 8OCB at T = 86$^o$C.

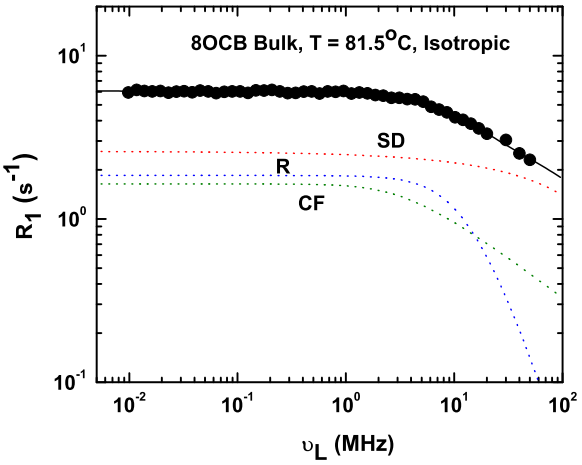


Figure 5.12: Frequency dependence of proton spin-lattice relaxation rate of bulk 8OCB at T = 81.5$^o$C.

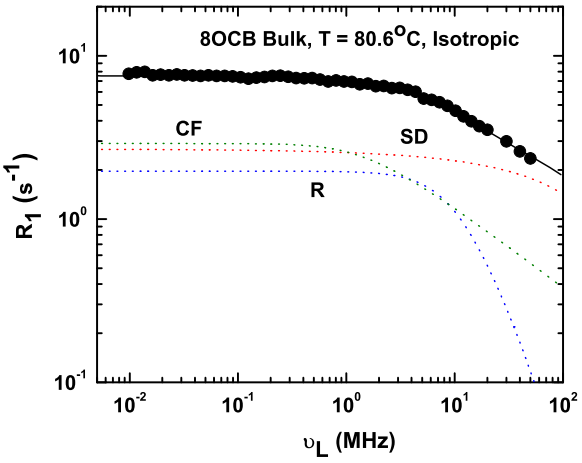


Figure 5.13: Frequency dependence of proton spin-lattice relaxation rate of bulk 8OCB at T = 80.6$^o$C.

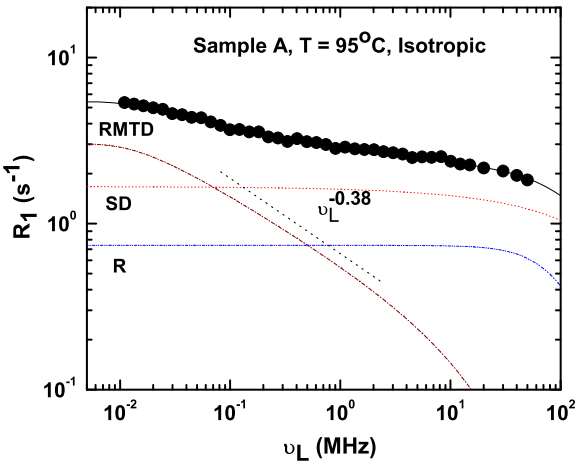


Figure 5.14: Frequency dependence of proton spin-lattice relaxation rate of Sample A at T = 95$^o$C. The black line is the calculated total relaxation rate obtained by using equation 5.2. Color lines are the corresponding relaxation rate contributions from different mechanisms as shown in the figure.

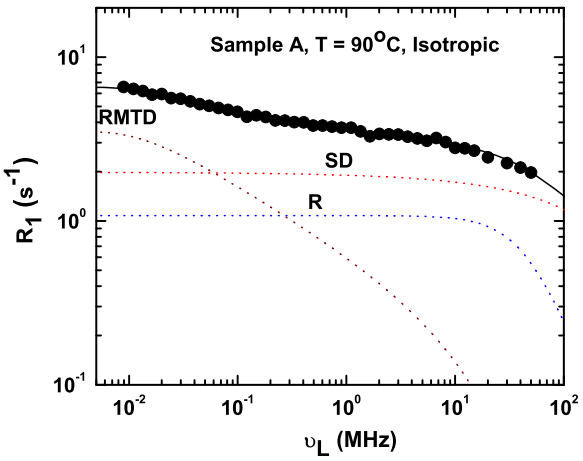


Figure 5.15: Frequency dependence of proton spin-lattice relaxation rate of Sample A at T= 90$^o$C.

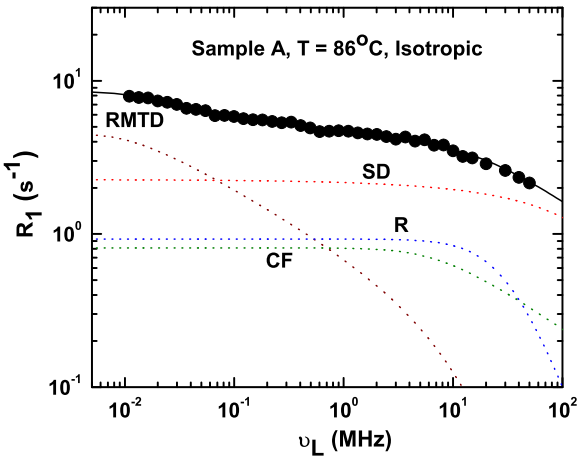


Figure 5.16: Frequency dependence of proton spin-lattice relaxation rate of Sample A at T= 86$^o$C.

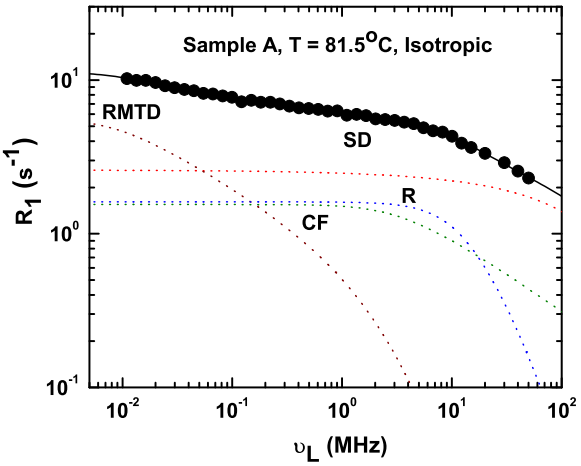


Figure 5.17: Frequency dependence of proton spin-lattice relaxation rate of Sample A at T= 81.5$^o$C.

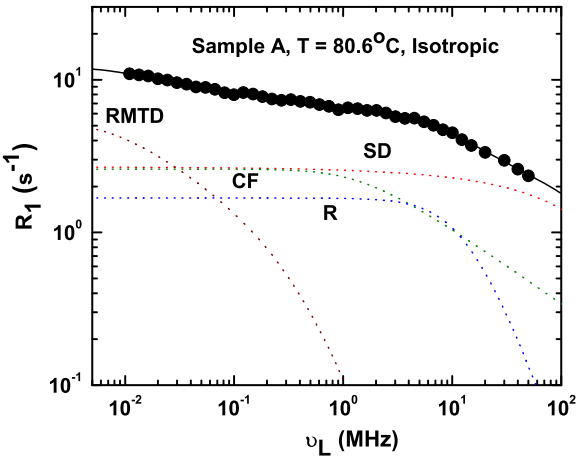


Figure 5.18: Frequency dependence of proton spin-lattice relaxation rate of Sample A at T= 80.6$^o$C.

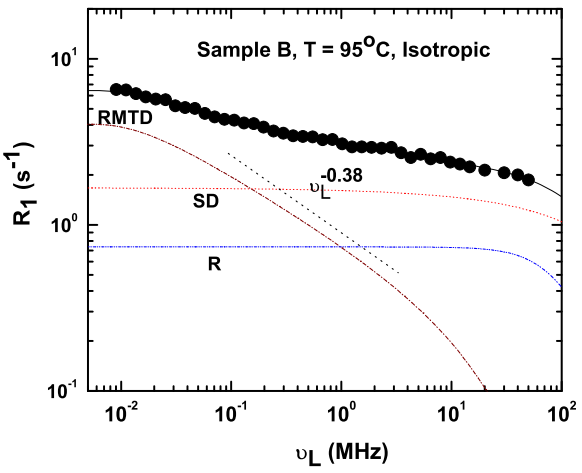


Figure 5.19: Frequency dependence of proton spin-lattice relaxation rate of Sample B at T = 95$^o$C. The black line is the calculated total relaxation rate obtained by using equation 5.2. Color lines are the corresponding relaxation rate contributions from different mechanisms as shown in the figure.

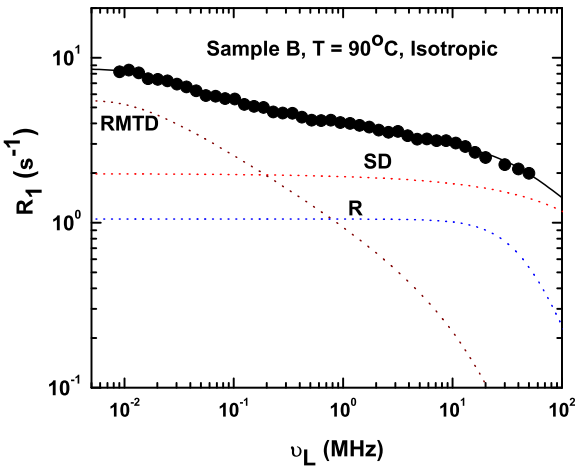


Figure 5.20: Frequency dependence of proton spin-lattice relaxation rate of Sample B at T = 90$^o$C.

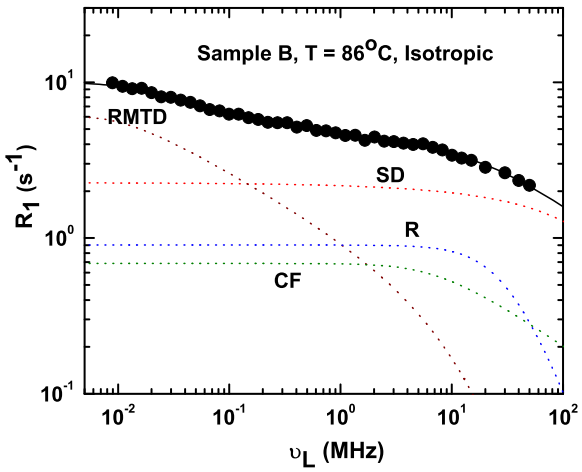


Figure 5.21: Frequency dependence of proton spin-lattice relaxation rate of Sample B at T = 86$^o$C.

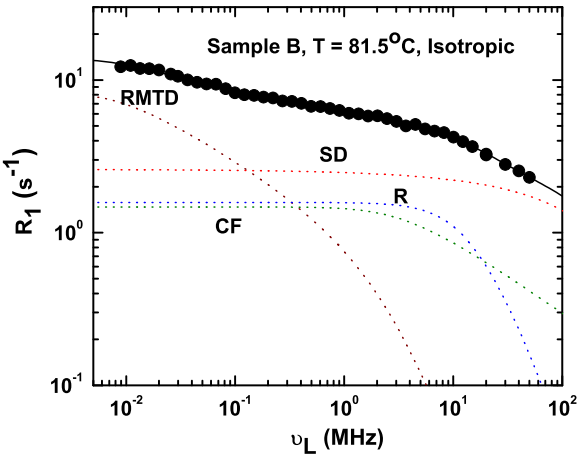


Figure 5.22: Frequency dependence of proton spin-lattice relaxation rate of Sample B at T = 81.5$^o$C.

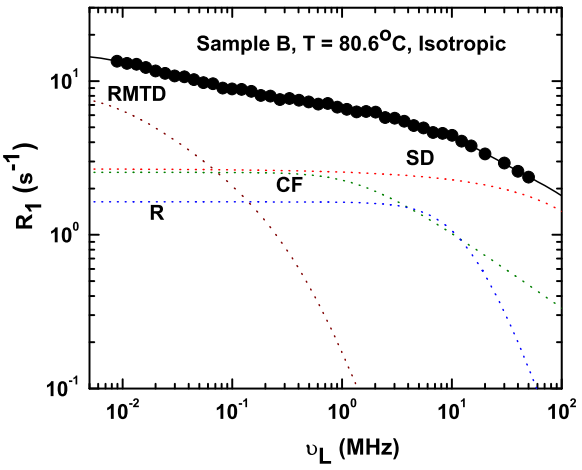


Figure 5.23: Frequency dependence of proton spin-lattice relaxation rate of Sample B at T = 80.6$^o$C.

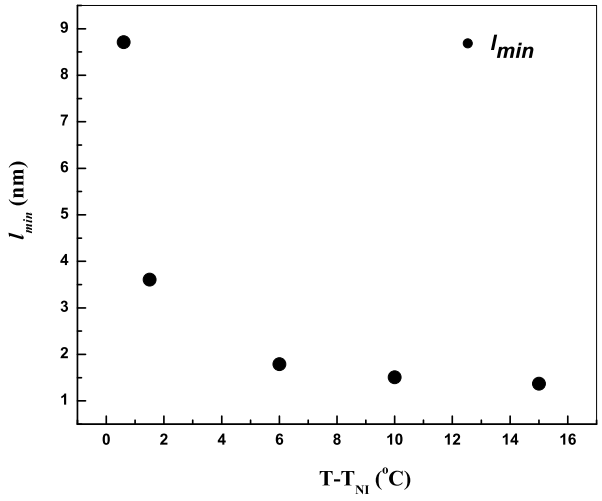


Figure 5.24: Temperature variation of $l_{min}$ above the isotropic-nematic transition.

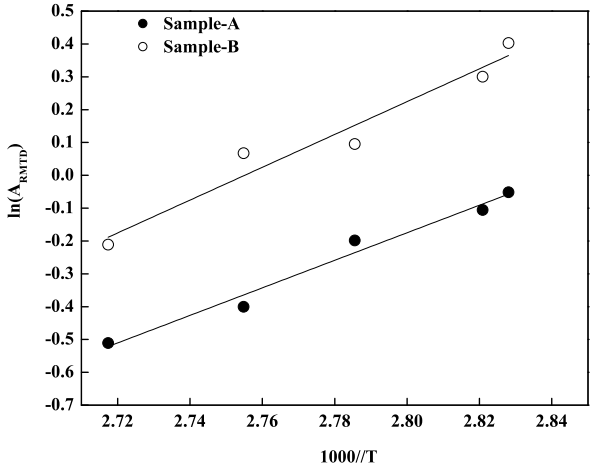


Figure 5.25: Temperature variation of $A_{RMTD}$ at different Aerosil concentrations. The solid line shows the best Arrhenius fit of the experimental data.

Table 5.1: Best fit parameters for the bulk 8OCB system in the isotropic phase.

| Sample | Bulk 8OCB Isotropic | | | | |
|---|---|---|---|---|---|
| T ($^oC$) | 95 | 90 | 86 | 81.5 | 80.6 |
| $A_D$ $10^8$ $s^{-2}$ | 25 | 25 | 25 | 25 | 25 |
| D $10^{-11}$ $m^2/s$ | 19.1 | 16.1 | 14.1 | 12.3 | 11.9 |
| $A_R$ $10^9$ $s^{-2}$ | 0.95 ± 0.05 | 0.75 ± 0.02 | 0.33 ± 0.01 | 0.27 ± 0.02 | 0.25 ± 0.01 |
| $\tau_R$ ns | 0.91 ± 0.05 | 1.77 ± 0.06 | 2.81 ± 0.21 | 6.86 ± 0.47 | 7.86 ± 0.23 |
| $A_{CF}$ $10^3$ $s^{-3/2}$ | – | – | 7 ± 0.06 | 8.34 ± 0.57 | 9.57 ± 0.15 |
| $\tau_{CF}$ ns | – | – | 35.42 ± 3.94 | 77.25 ± 10.60 | 183.77 ± 8.61 |

Table 5.2: Best fit parameters for Sample A in the isotropic phase.

| Sample | Sample A Isotropic | | | | |
|---|---|---|---|---|---|
| T ($^oC$) | 95 | 90 | 86 | 81.5 | 80.6 |
| $A_D$ $10^8$ $s^{-2}$ | 25 | 25 | 25 | 25 | 25 |
| D $10^{-11}$ $m^2/s$ | 19.1 | 16.1 | 14.1 | 12.3 | 11.9 |
| $A_R$ $10^9$ $s^{-2}$ | 0.95 | 0.75 | 0.33 | 0.27 | 0.25 |
| $\tau_R$ ns | 0.78 ± 0.01 | 1.77 ± 0.03 | 2.81 ± 0.02 | 5.97 ± 0.15 | 6.72 ± 0.19 |
| $A_{CF}$ $10^3$ $s^{-3/2}$ | – | – | 6.13 ± 0.13 | 7.89 ± 0.17 | 8.59 ± 0.16 |
| $\tau_{CF}$ ns | – | – | 35 | 77 | 183.8 |
| $\omega_{RMTDmin}$ kHz | 15 ± 1.38 | 13.8 ± 1.56 | 12 ± 1.82 | 9 ± 1.94 | 8 ± 1.99 |
| $\omega_{RMTDmax}$ MHz | 65 ± 9.56 | 45 ± 8.8 | 28 ± 4.79 | 6 ± 0.91 | 1 ± 0.04 |
| $A_{RMTD}$ $10^2$ $s^{-(1+p)}$ | 0.6 ± 0.007 | 0.67 ± 0.01 | 0.82 ± 0.01 | 0.90 ± 0.02 | 0.95 ± 0.02 |
| $p$ | 0.38 | 0.38 | 0.38 | 0.38 | 0.39 |

Table 5.3: Best fit parameters for Sample B in the isotropic phase.

| Sample | Sample B isotropic | | | | |
|---|---|---|---|---|---|
| T ($^oC$) | 95 | 90 | 86 | 81.5 | 80.6 |
| $A_D$ $10^8$ $s^{-2}$ | 25 | 25 | 25 | 25 | 25 |
| D $10^{-11}$ $m^2/s$ | 19.1 | 16.1 | 14.1 | 12.3 | 11.9 |
| $A_R$ $10^9$ $s^{-2}$ | 0.95 | 0.75 | 0.33 | 0.27 | 0.25 |
| $\tau_R$ ns | 0.78 ± 0.01 | 1.77 ± 0.03 | 2.75 ± 0.1 | 5.84 ± 0.13 | 6.55 ± 0.19 |
| $A_{CF}$ $10^3$ $s^{-3/2}$ | – | – | 5.19 ± 0.22 | 7.54 ± 0.12 | 8.4 ± 0.15 |
| $\tau_{CF}$ ns | – | – | 35 | 77 | 183.8 |
| $\omega_{RMTDmin}$ kHz | 15 ± 1.24 | 14 ± 1.28 | 12 ± 1.35 | 9 ± 1.45 | 8 ± 1.4 |
| $\omega_{RMTDmax}$ MHz | 65 ± 6.6 | 45 ± 4.5 | 28 ± 3.0 | 6 ± 0.35 | 1 ± 0.07 |
| $A_{RMTD}$ $10^2$ $s^{-(1+p)}$ | 0.81 ± 0.009 | 1.07 ± 0.01 | 1.1 ± 0.02 | 1.35 ± 0.02 | 1.5 ± 0.03 |
| $p$ | 0.38 | 0.38 | 0.38 | 0.38 | 0.39 |

relaxation mechanisms: reorientations about the short axes (R), translational self-diffusion (SD) and order parameter fluctuations (OPF). In the case of confined systems the additional RMTD mechanism also contributes to the total relaxation ($R_{1C}$). Therefore the total relaxation rates in both the cases are expressed as

$$R_{1B} = R_{1SD} + R_{1R} + R_{1OPF} \tag{5.3}$$

$$R_{1C} = R_{1SD} + R_{1R} + R_{1OPF} + R_{IRMTD}. \tag{5.4}$$

The bulk liquid crystal data at 1$^o$C below $T_{NI}$ (at 79$^o$C) is analyzed using equation (5.3). To reduce the number of fitting parameters, the diffusion coefficient was taken from the literature [24, 25]. The free parameters in the fitting procedure are the coupling constant for the diffusion process $A_D$, the prefactor describing the strength of the reorientations $A_R$, the reorientational correlation time around the short axes $\tau_R$, the contribution from order parameter fluctuations $A_{OPF}$, and their correlation time $\tau_{OPF}$. The results of this fit are shown in Table 5.4 in the column at $T = 79^oC$. Comparing the variation of parameters common to this phase and the isotropic phase (just above the transition), given in Table 5.1 under bulk sample at 80.6$^o$C, we find that coupling constant $A_D$ has decreased from 0.25 to 0.19 (in appropriate units as discussed in the Tables) across the transition, while $A_R$ (coupling to reorientations) remains essentially the same. The slight change in $\tau_R$ (from 7.86 ns to 8.15 ns) on cooling across the transition is within errors of estimation. The major change of course is in the time scale of order fluctuations as the nematic phase forms, from 183 ns in the isotropic phase to about 433 ns just below $T_{NI}$. Also coupling strength $A_{OPF}$ is now stronger in the nematic phase.

We present the results of our analysis of the two confined systems at this temperature in Figures 5.27 and 5.28. The effect of confinement is obvi-

ous by comparison of the experimental data with Figure 5.26, especially in the sub-MHz region. The various contributions making up for the observed relaxation rate are shown as usual in color with appropriate legend. The parameters extracted in these cases (at $T = 79^oC$) are given in Table 5.5 and 5.6. Comparing the values of the bulk system at this temperature (Table 5.4, at $79^oC$ ) with corresponding data on confined systems (Table 5.5 and Table 5.6, at $79^oC$), we find that $A_D$ decreases to 0.18 (as per the units of the Table) in Sample A from about 0.2 in bulk, and seems to decrease further slightly in Sample B. More prominent is the effect of confinement on the reorientational dynamics. The value of $\tau_R$ in bulk is 8 ns which decreases to 6 ns in Sample A and to 5.4 ns in Sample B, indicating increasing influence of the surface layer on the short axes reorientations. The corresponding coupling constant ($A_R$) is essentially constant within errors of estimation.

We now compare the dynamic parameters of the two confined systems as they are cooled across the transition from $80.6^oC$ to $79^oC$, as seen from Tables 5.2 and 5.3 (Sample A and Sample B at T = $80.6^oC$ and Table 5.5 and Table 5.6 at T = $79^oC$). The coupling to diffusion $A_D$, decreases from 0.25 to about 0.18 on the formation of the nematic phase, and is consistent with a similar change in the bulk sample. The decrease in $\tau_R$ in both the samples (from 6.7 ns to 6 ns in Sample A, and from 6 ns to 5.4 ns in Sample B) is outside the estimated errors, and is indicative of the manifestation of orientational order. Changes in the parameters connected with order fluctuations (*i.e.*, $A_{OPF}$ and $\tau_{OPF}$) in confined systems are consistent (and almost identical) with the corresponding bulk sample. Major impact of the onset of nematic order seems to be on the parameters connected with the RMTD mechanism. The coupling of the spin system to the lattice *via* this mechanism, quantified by $A_{RMTD}$, changes significantly across the transition from 0.95 to 2.1 in Sample A and from 1.5 to 3.1 in Sample B. Further, the exponent associated with the power law behavior of the dispersion in the intermediate frequency region changes from 0.38 to 0.45 and within estimation error approximates to equipartition value. At this stage, we need to interpret RMTD in a broader sense, meaning

that it encompasses not only the slow reorientational dynamics induced in the adsorbed layers near the surfaces, but also slow processes brought about by the bulk-like medium within the pore as well. Estimation of $\omega_{RMTD}$ cutoff frequencies in this analysis also are subjected to the same caveats entered into earlier at higher temperatures.

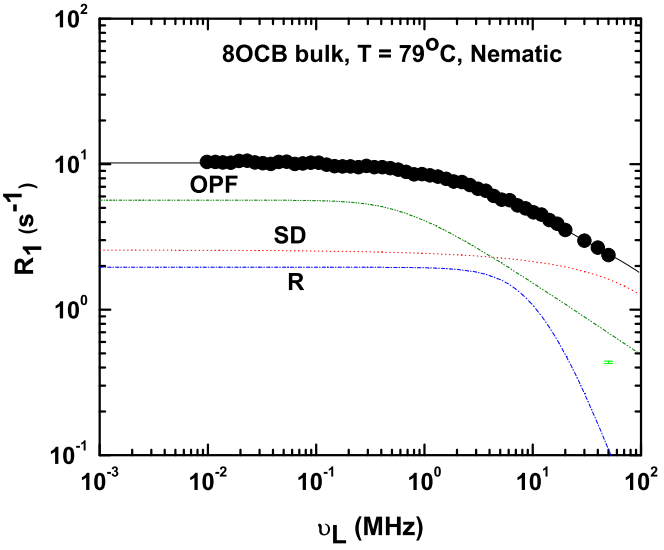


Figure 5.26: Frequency dispersion of the proton spin-lattice relaxation rate of bulk 8OCB at $T = 79^oC$

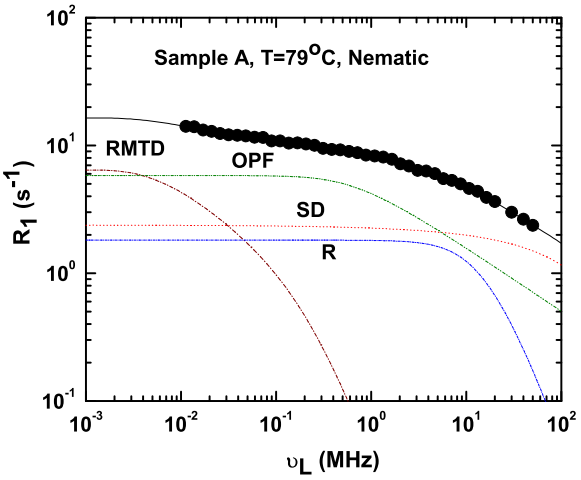


Figure 5.27: Frequency dispersion of the proton spin-lattice relaxation rate of Sample A at $T = 79^o$C.

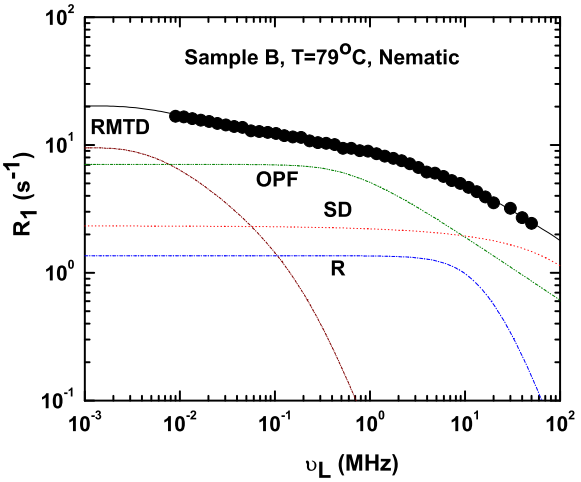


Figure 5.28: Frequency dispersion of the proton spin-lattice relaxation rate of Sample B at $T = 79^o$C

### 5.4.3 Mid nematic phase

In mid nematic phase and just above the smectic-nematic phase transition (at $T = 73^o$C and $68^o$C, respectively) the dispersion profiles were analyzed using the following mechanisms: reorientations around the short axes (R), translational displacements (SD) and order director fluctuations (ODF) in case of bulk liquid crystals ($R_{1B}$). The confined LC profiles ($R_{1C}$) are analyzed with RMTD mechanism along with other processes present in bulk system. The corresponding total relaxation rates are then expressed as

$$R_{1B} = R_{1SD} + R_{1R} + R_{1ODF} \tag{5.5}$$

$$R_{1C} = R_{1SD} + R_{1R} + R_{1X}. \tag{5.6}$$

Here $R_{1X}$ represents the combined effect of ODF and RMTD, often indistinguishable in the higher frequency range due to competing time scales [23].

The bulk LC dispersion data are analyzed based on equation 5.5 and the resulting fits are shown in Figures 5.29 and 5.30. Both show the usual $\omega^{-1/2}$ behavior of the ODF mechanism between the two cutoff frequencies. The lower cutoff frequency indicates in principle the inflection point below which the relaxation rate should become independent of frequency. In our experimental data we did not observe any distinguishable plateau at low frequencies, so the quoted value for the lower cutoff frequency is only indication that it is below the experimental value. The higher cutoff frequency was also similarly put at 100 MHz because its effect is again out of our experimental frequency range. Examples of such liquid crystal systems with essentially a power law contribution from the ODF over the range of the experiment are not uncommon [28].

Low frequency dispersion of confined nematic systems is more complex

and is in principle a result of two competing mechanisms imparting slow reorientating time correlations at molecular level. In addition to the RMTD mechanism, found important in the isotropic phase near the porous surfaces, the ODF mechanism also contributes in this frequency range. There are two ways one could account for the experimental observations [23]. One could, for example, assume ODF modes as the mediating mechanism, and any deviations of the dispersions, relative to the bulk, are to be interpreted as due to modifications of the ODF modes under confinement, *viz.* fractal nature of the collective modes on confinement. In such a case we refer to the modified ODF as X mechanism and fit the data to $R_{1X} = T_{1X}^{-1}$ extracting an effective exponent. We refer to this computation as fit-1. However it was noted [23] that such an interpretation also impacts the cutoff wavelengths of the ODF in the presence of the fractal dimensionality (deviating from the usual 3), and at least in that specific example [23], the corresponding correlation lengths were reported to be unrealistic. Another way of analyzing the data, say fit-2, could be to decompose the two mechanisms in the confined systems with seemingly competing time scales with the assumption that the coupling strength $A_{ODF}$ of the spin system to the liquid crystal medium *via* ODF mechanism be kept the same as in the bulk. In such a case the non-linear least squares fit then optimizes the cutoff frequencies (and hence appropriate cutoff length scales) of the ODF, and assigns the rest of the low frequency relaxation rate to the RMTD process.

Fit-2 perhaps imparts better physical insight. The change in the cutoff wavelengths of the ODF, in particular for the long wavelength modes, provide an evidence, and measure, of the finite and competing size of the confining pore on the ODF modes. Secondly, the parameters associated with the RMTD now tend to reflect the surface effects. Thus values of the exponent $p$ of the RMTD mediated power law, as well as of the $l_{min}$ and $l_{max}$, can be compared with the corresponding isotropic values. With this scope of analysis, we present the analysis of the data in the mid nematic region in terms of fit-1 and fit-2. Figures 5.31a - 5.31b (fit-1) show the fit of $(T_1^{-1})$

data of confined 8OCB at different concentrations at the two temperatures in the mid nematic phase to $(T_1^{-1})_x$ superimposed on the standard contributions from individual molecular processes like reorientations around short axes and self-diffusion. The magnitude of self-diffusion contribution shows changes in confined samples. The best fit value of the exponent $p$ in Sample A and Sample B is 0.52 ± 0.003 and 0.56 ± 0.004. This value could in principle be viewed as a consequence of an increase in the relaxation rate upon confinement, arising from the fractal nature of director fluctuations in the cavities as suggested by Leon et al [29]. However there were also counter arguments against this interpretation [23] as fractional dimensionality also enters into the calculation of associated length scales and correspondingly they may tend to be unrealistic. Also this has an unsatisfactory consequence of making completely the slow orientational correlations induced at the surface due to adsorption and molecular surface diffusion in the presence of local surface induced order. Thus, we prefer to analyze the data with the additional RMTD mechanism also, though fully recognizing their competing nature in the mid-frequency region (above $\omega_{ODFmin}$). Obviously analysis of the data in this range, in particular assignment of relative contributions of the two processes, can not be said to be unique. Frequency dispersion of the relaxation rate below $\omega_{ODFmin}$, if any, then can be reasonably attributed to RMTD, and the corresponding parameters can be considered for appreciating the effects of surface interactions. With this objective, we carried out the analysis (fit-2) by assigning the low frequency relaxation rate dispersions $(T_1^{-1})_{ODF}+(T_1^{-1})_{RMTD}$, obtaining quantitative contributions from both ODF and RMTD. The low frequency cutoff of ODF is left as a free parameter and $A_{ODF}$ is fixed at the bulk value as discussed before. The results of these fits are shown in Figures 5.32 - 5.35. The fitted parameters are shown in Tables 5.5 and 5.6. The lower cutoff frequencies of ODF mechanism in confined samples have now shifted to higher frequencies relative to the bulk values ($\sim$ kHz) and are of 4.7 MHz for Sample A and 5.9 MHz for Sample B, at $73^oC$. Their values further increase with decrease of temperature in the nematic phase. This is a direct evidence that confinement is severely restricting the long wavelength modes of the ODF, pushing the lower cutoff frequencies by

an order of magnitude. This also signifies that the major contribution to relaxation rate in confined systems in the sub-MHz regime is due to RMTD mechanism.

The fits also clearly show the importance of RMTD mechanism at low frequencies and the exponent values obtained with fit-2 are 0.55 ± 0.007 and 0.58 ± 0.01. These values are marginally high compared to the values obtained from fit-1. The increase in the exponent from 0.45 (Table 5.5 and 5.6, at $T = 79^{o}$C) near the transition to 0.55 in the mid nematic phase shows the enhanced relative importance of longer wavelength modes on cooling the nematic phase. The exponent value also shows marginal increase with the concentration of aerosil particles, hinting at its dependence on the void/pore size. The RMTD interaction strength $A_{RMTD}$ also increases by one order of magnitude in the nematic phase. Decrease of higher cutoff value of the $\omega_{RMTD}$ with decrease of temperature signifies the enhancement of surface-induced order in the voids. The lower cutoff frequency for RMTD could not be estimated with any confidence since the data did not taper off to a low frequency plateau within the experimental range.

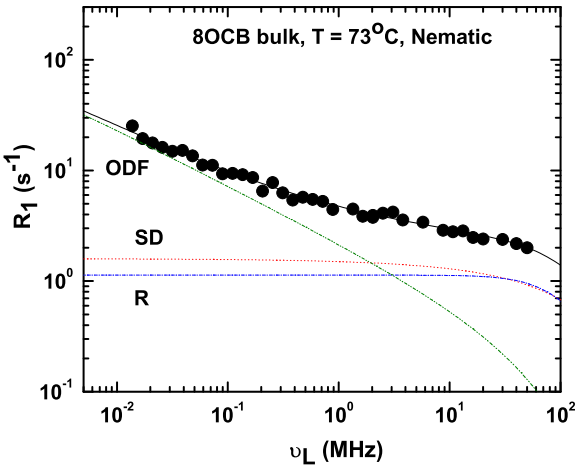


Figure 5.29: Frequency dispersion of the proton spin-lattice relaxation rate of bulk 8OCB at $T = 73^{o}$C.

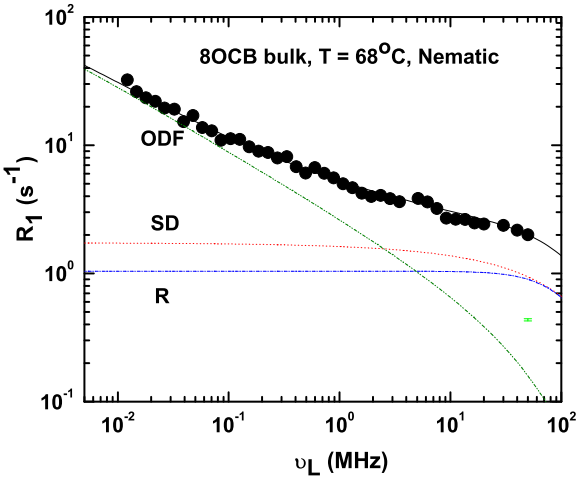


Figure 5.30: Frequency dispersion of the proton spin-lattice relaxation rate of bulk 8OCB at $T = 68^{o}$C.

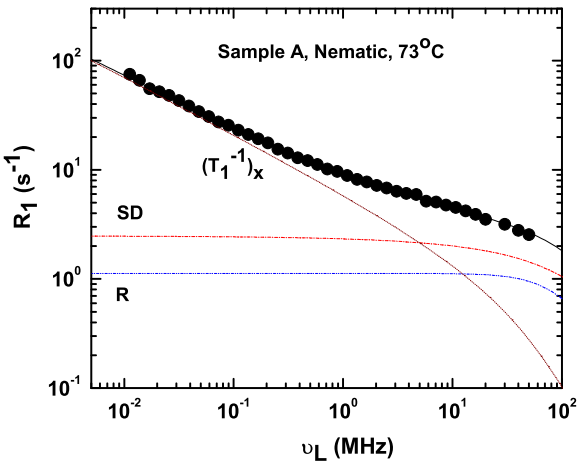


(a)

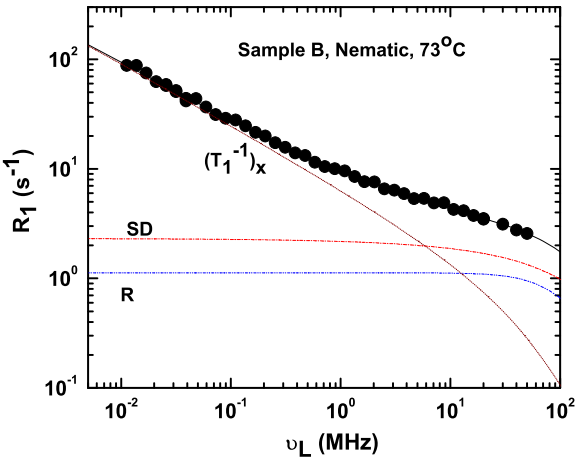


(b)

Figure 5.31: Frequency dispersion of proton spin-lattice relaxation rate at $T = 73^oC$: (a) Sample A; (b) Sample B.

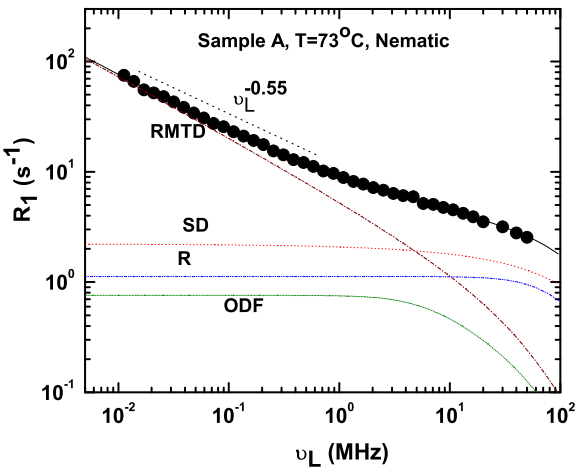


Figure 5.32: Frequency dispersion of the proton spin-lattice relaxation rate of Sample A at $T = 73^o$C.

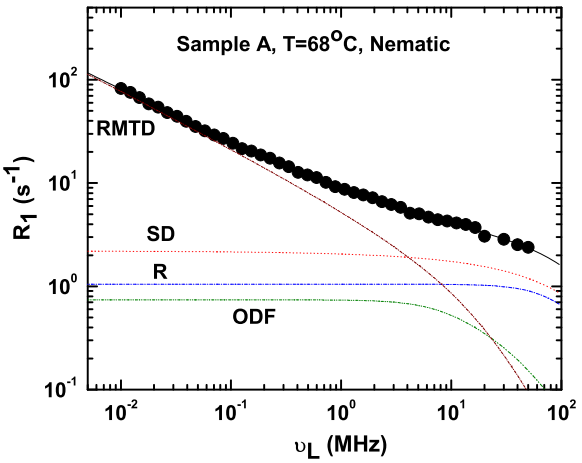


Figure 5.33: Frequency dispersion of the proton spin-lattice relaxation rate of Sample A at $T = 68^o$C.

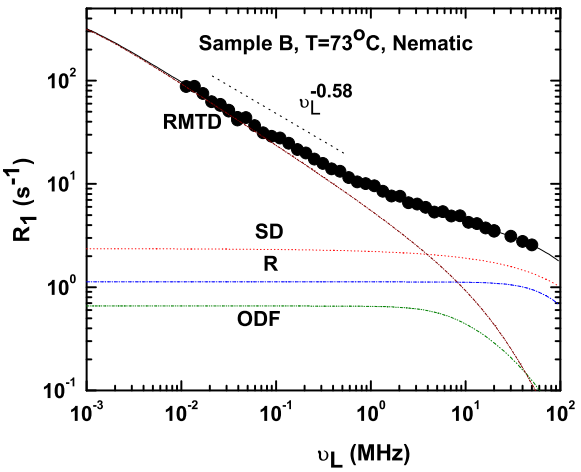


Figure 5.34: Frequency dispersion of the proton spin-lattice relaxation rate of Sample B at $T = 73^o$C.

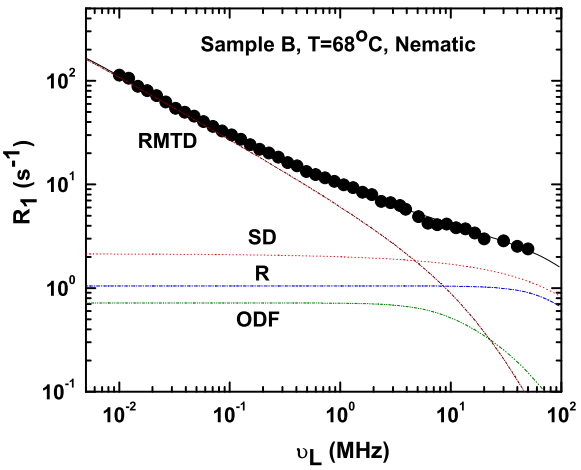


Figure 5.35: Frequency dispersion of the proton spin-lattice relaxation rate of Sample B at $T = 68^o$C.

### 5.4.4 Smectic phase

In the smectic phase of bulk system, the frequency dispersion is usually attributed to reorientations and self-diffusion process and the low frequency dispersions are expected due to slow layer undulations [LU] [21]. ODF process is not considered to be significant on general arguments, because bend and twist distortions are expected to be energetically costly due to layer formation and hence do not contribute to the ODF dynamics. It is thus plausible to attempt to fit the data with only R, SD and LU. But our analysis shows that such an attempt leads to an unrealistically low value for the diffusion coefficient (decreases by more than one order of magnitude). Instead, we prefer to include the ODF mechanism as well into our consideration, along with LU, to account for the low frequency data. Similar argument was advanced earlier also [30] to interpret data on 8CB. Thus we write the total relaxation rate in bulk smectic phase at $T = 61^oC$ ($R_{1B}$) as,

$$R_{1B} = R_{1SD} + R_{1R} + R_{1ODF} + R_{1LU}. \tag{5.7}$$

For the confined LC system in the smectic phase, we introduce the additional RMTD mechanism to account for the observed relative increase on confinement, and write the corresponding relaxation rate $R_{1C}$ as,

$$R_{1C} = R_{1SD} + R_{1R} + R_{1ODF} + R_{1LU} + R_{1RMTD}. \tag{5.8}$$

The bulk dispersion profile is analyzed using equation 5.7 and the fit is shown in Figure 5.36. The layer undulations are very effective below about 20 kHz, and ODF is seen dominant in the sub MHz regime. Individual processes are effective only at higher frequencies as expected. Dispersion data of LC confined to aerosil matrix is fitted to equation 5.8 and the fits are shown in Figures 5.37 and 5.38. In confined systems it is not possible to uniquely distinguish between the contribution of the LU and RMTD mechanisms because both of them mediate in the same frequency region. Further, in the

smectic phase, the lower frequency cutoff of the ODF is found to be small compared to its value in the nematic phase, reflecting the effect of the formation of layers. The exponent value of RMTD shows a marginal decrease to 0.5 and below, depending on the aerosil density. This suggests that the longer wavelength diffusion modes in the RMTD are less prominent in the smectic phase. This may be compared to studies on 8CB in random porous glass (CPG of diameter 15 nm) where the relaxometry studies indicate that the temperature variation of relaxation rate at different Larmor frequencies could not show the signature of the onset of phase transition from nematic to smectic phase [23]. It was also reported that the exponent value increased continuously as one cools the system from nematic to smectic phase.

In contrast, in our system we find clear signatures of this transition on the relaxation rates (Figures 5.6 to 5.8), in particular even after confinement. This clearly shows (see, for example data at 12 kHz in these figures across N-$S_A$ transition) that the onset of smectic phase leaves the system with a loss of low frequency contribution both in bulk as well as in confined systems, with the corresponding loss being progressively smaller with enhanced confinement. Thus we see that within the limits to which we could restrict the system in our experiments, smectic phase is inhibiting long wavelength modes in the system, resulting in a corresponding decrease in the exponent of the RMTD. This also seems consistent with the fact that the present arrangement pertains to a 3-d confinement (with a typical pore size of $\sim$ 100 nm), with the surface wall made up of connected silica particles of very small size ($\sim$ 7nm).

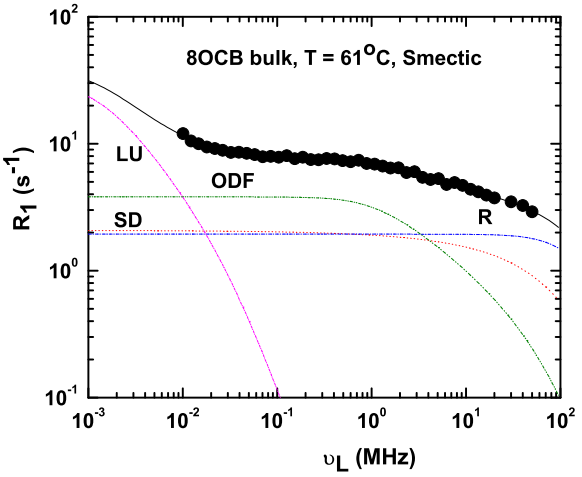


Figure 5.36: Frequency dispersion of the proton spin-lattice relaxation rate of bulk 8OCB at $T = 61^{o}$C.

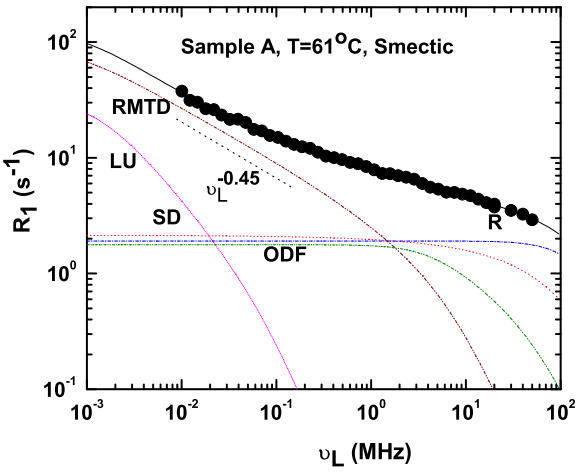


Figure 5.37: Frequency dispersion of the proton spin-lattice relaxation rate of Sample A at $T = 61^{o}$C.

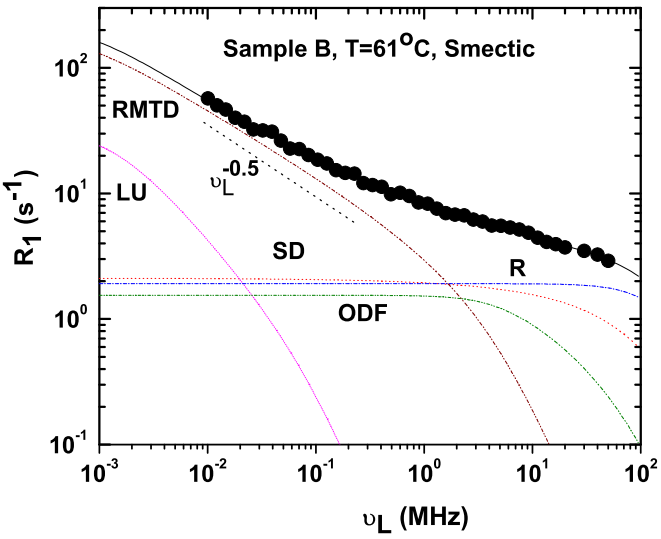


Figure 5.38: Frequency dispersion of the proton spin-lattice relaxation rate of Sample B at $T = 61^{o}$C.

Table 5.4: Best fit values of the parameters obtained in calculating the relaxation rate dispersion curves in the nematic and smectic phases of a bulk 8OCB.

| Sample | Bulk 8OCB | | | |
|---|---|---|---|---|
| T ($^o$C) | 79 | 73 | 68 | 61 |
| $A_D$ $10^8$ $s^2$ | 19.73 ± 0.88 | 9.42 ± 0.64 | 8.55 ± 0.89 | 6.5 ± 0.04 |
| D $10^{-11}$ $m^2/s$ | 9.8 | 7.5 | 6.3 | 4 |
| $A_R$ $10^9$ $s^2$ | 0.24 ± 0.02 | 1.5 | 1.5 | 3.92 ± 0.48 |
| $\tau_R$ ns | 8.15 ± 0.62 | 0.75 ± 0.06 | 0.7 ± 0.1 | 0.49 ± 0.07 |
| $A_{OPF}$ $10^3$ $s^{-3/2}$ | 12.31 ± 1.07 | – | – | – |
| $\tau_{OPF}$ ns | 422.9 ± 35.9 | – | – | – |
| $A_{ODF}$ $10^3$ $s^{-3/2}$ | – | 5.84 ± 0.07 | 7.20 ± 0.07 | 11.11 ± 0.32 |
| $\omega_{ODFmin}/2\pi$ kHZ | – | 1 | 1 | 1 |
| $\omega_{ODFmax}/2\pi$ MHz | – | 100 | 100 | 100 |
| $A_{LU}$ $10^3$ $s^{-3/2}$ | – | – | – | 609.78 ± 35.86 |
| $\omega_{LUmin}/2\pi$ kHZ | – | – | – | 1 |
| $\omega_{LUmax}/2\pi$ kHZ | – | – | – | 0.04 ± 0.0088 |

Table 5.5: Best fit values of the parameters obtained in calculating the relaxation rate dispersion curves in the nematic and smectic phases of Sample A.

| Sample | Sample A | | | |
|---|---|---|---|---|
| T ($^o$C) | 79 | 73 | 68 | 61 |
| $A_D$ $10^8$ $s^2$ | 18.27 ± 0.54 | 13.0 ± 0.19 | 10.85 ± 0.36 | 6.71 ± 0.07 |
| D $10^{-11}$ $m^2/s$ | 9.8 | 7.5 | 6.3 | 4 |
| $A_R$ $10^9$ $s^2$ | 0.3 ± 0.02 | 1.5 | 1.5 | 3.92 |
| $\tau_R$ ns | 6.04 ± 0.44 | 0.75 | 0.7 | 0.49 |
| $A_{OPF}$ $10^3$ $s^{-3/2}$ | 12.65 ± 0.41 | – | – | – |
| $\tau_{OPF}$ ns | 423 | – | – | – |
| $A_{ODF}$ $10^3$ $s^{-3/2}$ | – | 5.84 | 7.20 | 11.11 |
| $\omega_{ODFmin}/2\pi$ kHZ | – | 4695.2 ± 1115.8 | 6702.8 ± 1376.7 | 3374.2 ± 417.6 |
| $\omega_{ODFmax}/2\pi$ MHz | – | 100 | 100 | 100 |
| $A_{LU}$ $10^3$ $s^{-3/2}$ | – | – | – | 609.78 ± 35.86 |
| $\omega_{LUmin}/2\pi$ kHZ | – | – | – | 1 |
| $\omega_{LUmax}/2\pi$ kHZ | – | – | – | 0.1 |
| $\omega_{RMTDmin}/2\pi$ kHZ | 6.5 | 1 | 1 | 1 |
| $\omega_{RMTDmax}/2\pi$ MHZ | 0.5 | 150 | 50.5 ± 11.6 | 16.9 ± 3.2 |
| $A_{RMTD}$ $10^2$ $s^{-(1+p)}$ | 2.08 ± 0.1 | 88.8 ± 7.74 | 93.8 ± 4.4 | 10.17 ± 0.16 |
| $p$ | 0.45 ± 0.05 | 0.55 ± 0.007 | 0.55 ± 0.004 | 0.45 ±0.03 |

Table 5.6: Best fit values of the parameters obtained in calculating the relaxation rate dispersion curves in the nematic and smectic phases of Sample B.

| Sample | Sample B | | | |
|---|---|---|---|---|
| T ($^o$C) | 79 | 73 | 68 | 61 |
| $A_D$ $10^8$ $s^2$ | 17.88 ± 0.35 | 13.86 ± 0.41 | 10.59 ± 0.25 | 6.62 ± 0.07 |
| D $10^{-11}$ $m^2/s$ | 9.8 | 7.5 | 6.3 | 4 |
| $A_R$ $10^9$ $s^2$ | 0.25 ± 0.02 | 1.5 | 1.5 | 3.92 |
| $\tau_R$ ns | 5.44 ± 0.3 | 0.75 | 0.7 | 0.49 |
| $A_{OPF}$ $10^3$ $s^{-3/2}$ | 15.33 ± 0.38 | – | – | – |
| $\tau_{OPF}$ ns | 423 | – | – | – |
| $A_{ODF}$ $10^3$ $s^{-3/2}$ | – | 5.84 | 7.20 | 11.11 |
| $\omega_{ODFmin}/2\pi$ kHZ | – | 5912.1 ± 2742.2 | 7000.8 ± 1700 | 4205.4 ± 789.4 |
| $\omega_{ODFmax}/2\pi$ MHz | – | 100 | 100 | 100 |
| $A_{LU}$ $10^3$ $s^{-3/2}$ | – | – | – | 609.78 ± 35.86 |
| $\omega_{LUmin}/2\pi$ kHZ | – | – | – | 1 |
| $\omega_{LUmax}/2\pi$ kHZ | – | – | – | 0.1 |
| $\omega_{RMTDmin}/2\pi$ kHZ | 6.5 | 1 | 1 | 1 |
| $\omega_{RMTDmax}/2\pi$ MHZ | 0.5 | 65.1 ± 16.8 | 46.2 ± 5.87 | 10 ± 1.2 |
| $A_{RMTD}$ $10^2$ $s^{-(1+p)}$ | 3.07 ± 0.1 | 161.58 ± 22.27 | 204.71 ± 1 | 32.52 ± 6.38 |
| $p$ | 0.45 ± 0.05 | 0.58 ± 0.01 | 0.59 ± 0.004 | 0.5 ±0.02 |

## 5.5 Conclusions

We measured the proton spin-lattice relaxation rate dispersions of bulk 8OCB and 8OCB embedded in random porous network formed by aerosil nano particles at different concentrations. We observed a relaxation rate increase in the spin relaxation profiles in all the phases upon confinement. This observed significant increase is quantitatively explained in terms of an additional slow relaxation mechanism of molecular reorientations mediated by translational displacements (RMTD), and it is characterized by power-law dispersion in the frequency range between low and high frequency cutoff values. The analysis of the experimental data shows that the major increase in the relaxation rate is due to this process. The low and high frequency cutoff values of the RMTD mechanism provide some insight into how the molecules are reorienting at the surface. The exponent value in the isotropic phase is found to be 0.38 indicating that the relative importance of low wavelength modes has increased compared to expectations from equipartition distribution, and it is different from the other confined systems studied in the isotropic phase. The exponent varies with temperature from 0.45 to 0.55 in case of Sample A and 0.45 to 0.6 in case of Sample B from just below the isotropic-nematic transition to just above the smectic-nematic transition. In the smectic phase its value dips again to 0.45 ($\pm$0.05) because the layer formation seems to restrict the longer wavelength modes. An increase of low frequency cutoff of ODF clearly indicates the effect of confinement on the collective modes of the system. In this process, it offers an opportunity to explore the exclusive effects of RMTD in this otherwise dispersion-free low frequency regime. The strength of the RMTD mechanism in the nematic phase has increased by an order of magnitude compared to the isotropic phase. As a general rule, the strength of RMTD has increased in all the phases with increase of concentration of aerosil particles. This is a direct reflection of the surface effects on the spin-lattice relaxation mechanisms. The other dynamic processes do not seem to have been affected much upon confinement, except the reorientational correlation time near the isotropic-nematic transition.

# References

[1] G. P. Crawford and S. Zumer, *Liquid crystals in complex geometries*, Taylor and Francis, London (1996).

[2] G. S. Iannacchione, C. W. Garland, J. T. Mang, T. P. Rieker, Phys. Rev. E **58**, 5966 (1998).

[3] A. Roshi, S. Barjami, G. S. Iannacchione, D. Paterson, I. Mcnulty, Phys. Rev. E **74**, 031404 (2006).

[4] A. Hourri, T. K. Bose, and J. Theon, Phys. Rev. E **63**, 051702 (2001).

[5] Jan Leys, Christ Glorieux and Jan Theon, J. Phys: Condens. Matter **20**, 244111 (2008).

[6] E. Anoardo, F. Grinberg, M. Vilfan, and R. Kimmich, Chem. Phys. **297**, 99 (2004).

[7] M. Rajeswari, S. Dhara, K. Venu, V. S. S. Sastry, R. Dabrowski (to appear in Mol. Cryst. Liq. Cryst, 2011).

[8] T. Jin, D. Finotello, Phys. Rev. Lett. **86**, 818 (2001).

[9] T. Jin, D. Finotello, Phys. Rev. E **69**, 041704 (2004).

[10] T. Bellini, M. Buscaglia, C. Chiccoli, F. Mantegazza, P. Pasini, C. Zannoni, Phys. Rev. Lett. **85**, 1008 (2000).

[11] Noel A. Clark, Tommaso Bellini, Rainer M. Malzbender, Britt N. Thomas, Aqron G.Rappaport, Chris D. Muzny, Dale W. Schaefer, and Larry Hrubesh, Phys. Rev. Lett. **71**, 3505 (1993).

[12] S. Kralj, A. Zidansek, G. Lahajnar, I. Musevic, S. Zumer, R. Blinc, and M. M. Pintar, Phys. Rev. E **53**, 3629 (1996).

[13] M. D. Dadmun and M. Muthukumar, J. Chem. Phys. **98**, 4850 (1993).

[14] G. S. Iannacchione, Fluid Phase Equilibria. **222-223**, 177 (2004).

[15] G. S. Iannacchione and D. Finotello, Phys. Rev. Lett. **69**, 2094 (1992).

[16] P. S. Clegg, C. Stock, R. J. Birgeneau, C. W. Garland, A. Roshi, and G. S. Iannacchione, Phys. Rev. E **67**, 021703 (2003).

[17] A. Roshi, G. S. Iannacchione, P. S. Clegg, R. J. Birgeneau, Phys. Rev. E **69**, 031703 (2004).

[18] R. Kimmich, E. Anoardo, Prog. Nucl. Magn. Reson. Spectrosc. **44**, 257 (2004).

[19] F. Noack, Prog. Nucl. Magn. Reson. Spectrosc. **18**, 171 (1986).

[20] A. Abragam, *The Principles of Nuclear Magnetism,* Clarendon Press, Oxford (1961).

[21] R. Y. Dong, *Nuclear Magnetic Resonance of Liquid Crystals*, Springer-Verlag (1997).

[22] Rainer Kimmich and Hans Werner Weber, Phys. Rev. B **47**, 11788 (1993).

[23] M. Vilfan, T. Apih, P. J. Sebastiao,G. Lahajnar, and S. Zumer, Phys. Rev. E **76**, 051708 (2007).

[24] J. O. Mager, Ph.D. Thesis, University of Stuttgart (1993).

[25] M. Cifelli, P. J. McDonald, C. A. Veracini, Phys. Chem. Chem. Phys, **6**, 4701, (2004).

[26] B. V. N. Phanikumar, V. Satheesh, K. Venu, V. S. S. Sastry, and R. Dabrowski, Phase Transitions. **82**, 131 (2009).

[27] P. J. Sebastiao, D. Sousa, A. C. Ribeiro, M. Vilfan, G. Lahajnar, J. Seliger, and S. Zumer, Phys. Rev. E **72**, 061702 (2005).

[28] A. Carvalho, P. J. Sebastiao, A. C. Ribeiro, H. T. Nguyen, and M. Vilfan, J. Chem. Phys. **115**, 10484 (2001).

[29] N. Leon, J. P. Korb, I. Bonalde, and P. Levitz, Phys. Rev. Lett. **92**, 195504 (2004).

[30] R. H. Acosta and D. J. Pusiol, Phys. Rev. E **60**, 1808 (1999).

# 6

# Slow molecular dynamic processes in a nematic liquid crystal embedded in aerosil matrix: Nuclear magnetic relaxometric study

## 6.1 Introduction

The previous chapter summarizes the effect of nano confinement effected by 3-d random network of aerosil particles on a prototype liquid crystal, 8OCB, in its isotropic phase, as well as in the underlying nematic and smectic-A phases. The effect of the surface of the porous matrix is transmitted to the liquid crystal medium via polar interactions, and is known to play a significant role [1–10]. In the earlier example the electric dipole is approximately along the long axis of the molecule, and the homeotropic alignment direction of molecules within the adsorption layer is coincident with the dipole orientation. As was indicated before, this chapter summarizes very similar spin-lattice relaxation dispersion studies carried out on a different liquid crystal system 4-propyl-4′-pentylazoxybenzene (PPA). These molecules have their dipole moments in the lateral direction (Figure 6.1), and consequently the

surface dynamics of these molecules could in principle differ from the case of 8OCB. Another contrast is its phase sequence: PPA has no underlying layered mesophases, and form a crystal directly from its nematic phase (Figure 6.1). To facilitate a fair comparison of dynamics in these two systems, the confining conditions are kept the same as before.

After providing the experimental details in Section 6.2, appropriate relaxation models are indicated in Section 6.3, followed by analysis of data in different phases (Section 6.4). The results are summarized, and compared with those of 8OCB in the final section. It may be noted that the relaxation models needed to analyze the present data in the isotropic and nematic phases as well as certain details of analysis are already discussed earlier (in the previous chapter), and consequently some parts of the presentation may look somewhat brief.

## 6.2 Experimental details

The liquid crystal used in this study was synthesized in the laboratory of Prof. R. Dabrowski in Warsaw, Poland. The molecular structure and its phase sequence are shown in Figure 6.1. The preparation of LC-Aerosil mixtures were explained in detail in Chapter 3 and 5. The density of silica particles in our samples was 0.05 (Sample A) and 0.07 (Sample B) g/cm$^3$. The shift of the transition temperatures is within $\pm$1K at both the aerosil concentrations. Proton spin-lattice relaxation times were measured at different Larmor frequencies using the field-cycling NMR relaxometry (Stelar Spinmaster FFC 2000) from 10 kHz to 10 MHz and a pulsed field variable spectrometer is used at 20 MHz. The decay of magnetization was exponential in this sample indicating the single relaxation time constant. The errors in the $T_1$ measurements were within 3% and the temperature of the sample was controlled to within $\pm$0.1K.

## 6.2 Experimental details

The frequency dependences of relaxation rates of bulk PPA in the isotropic and nematic phases are shown in Figures 6.2a - 6.2b. Figures 6.3a - 6.3b and 6.4a - 6.4b show its frequency dispersion when confined to aerosil matrix at the two different concentrations mentioned. The temperature dependence of relaxation rates at different Larmor frequencies of bulk and confined samples are shown in Figures 6.5 - 6.7. These show the pretransitional behavior near the isotropic-nematic transition and significant frequency dispersion introduced in the nematic phase, in the bulk and confined systems.

4-propyl-4'-pentylazoxybenzene (PPA)

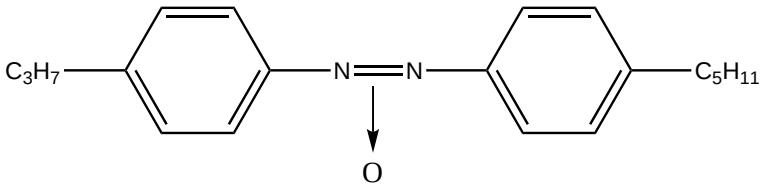


Cr 0°C N 61.8°C I

Figure 6.1: Molecular structure and phase sequence of the liquid crystal PPA.

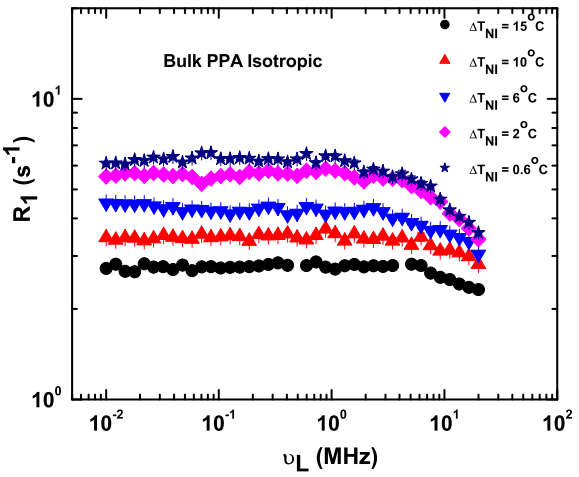


(a)

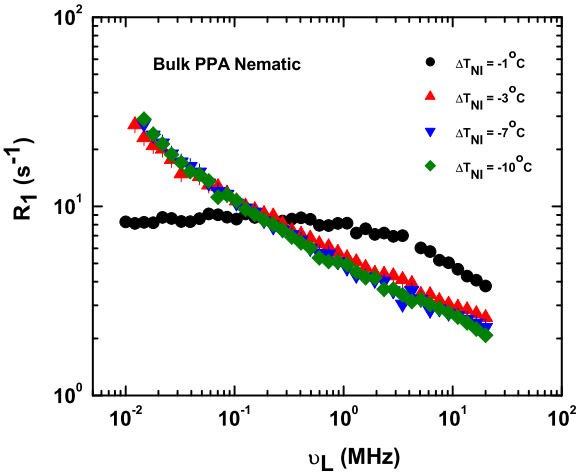


(b)

Figure 6.2: Frequency dispersion of the proton spin-lattice relaxation rate profiles of bulk PPA in different phases: (a) Isotropic; (b) Nematic.

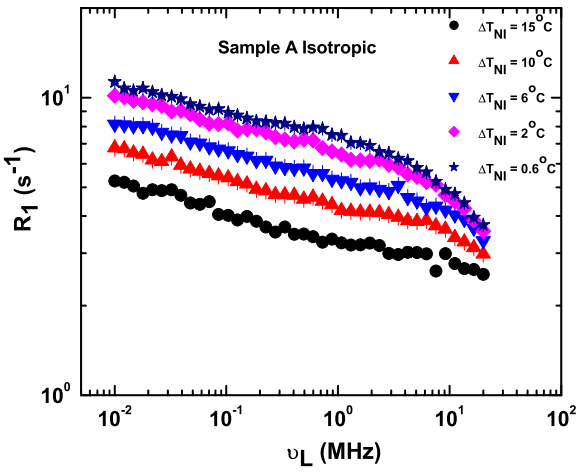


(a)

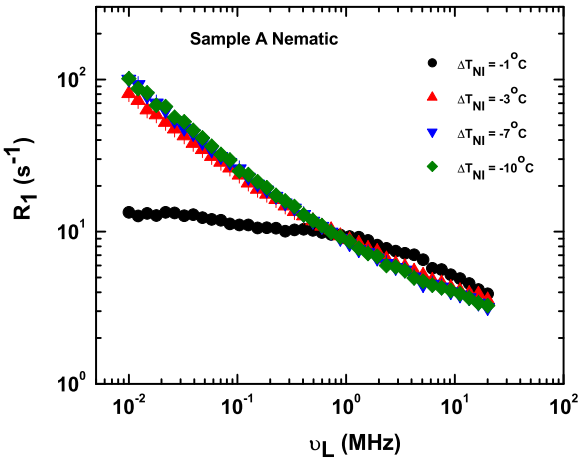


(b)

Figure 6.3: Frequency dispersion of the proton spin-lattice relaxation rate profiles of Sample A in different phases: (a) Isotropic; (b) Nematic.

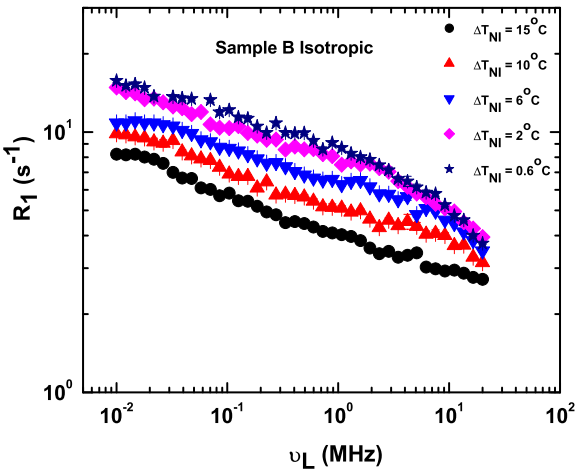


(a)

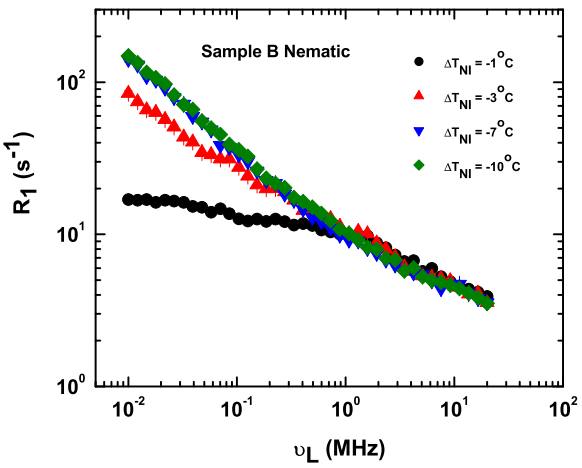


(b)

Figure 6.4: Frequency dispersion of the proton spin-lattice relaxation rate profiles of Sample B in different phases: (a) Isotropic; (b) Nematic.

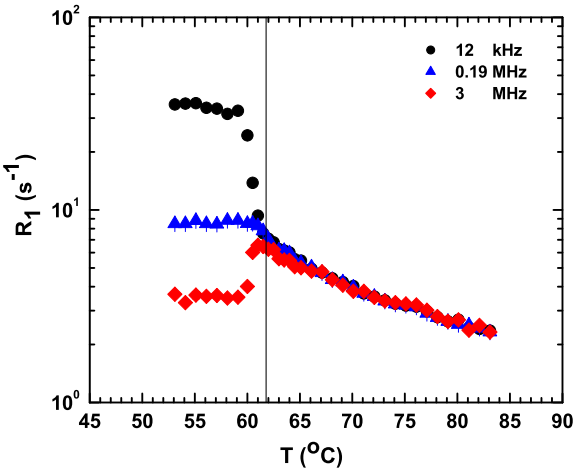


Figure 6.5: Temperature dependence of the proton spin-lattice relaxation rate at three Larmor frequencies in bulk PPA.

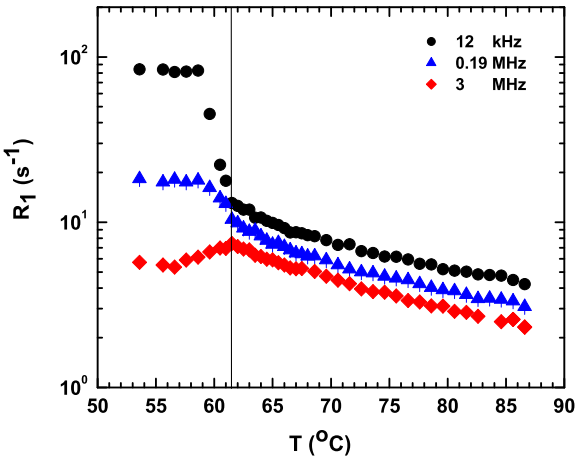


Figure 6.6: Temperature dependence of the proton spin-lattice relaxation rate at three Larmor frequencies in Sample A.

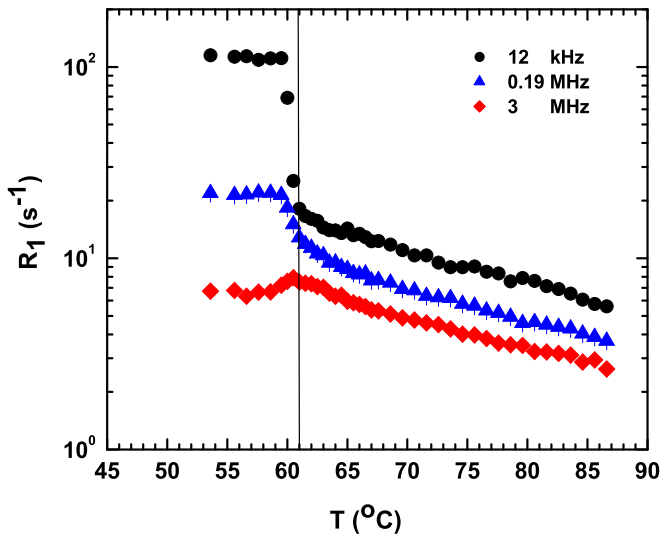


Figure 6.7: Temperature dependence of the proton spin-lattice relaxation rate at three Larmor frequencies in Sample B.

## 6.3 Relaxation mechanisms

The proton spin-lattice relaxation is mediated by the time modulation of dipole-dipole interactions between the neighboring spins [11, 12]. The time variation of spin interactions occurs either due to individual processes such as reorientations around the short axes (R) and translational self-diffusion (SD) modulating inter-molecular interaction and collective processes like critical fluctuations (CF) and order parameter fluctuations (OPF) near the transition point, order director fluctuations (ODF) in the nematic phase for bulk systems [11]. In the case of confined systems, the confinement induces additional relaxation mechanism *i.e.*, molecular reorientations mediated by translational displacements (RMTD) [13–15]. The theoretical expressions for these relaxation mechanisms are given in Chapter 2 and are used to interpret data in the previous chapter. The total relaxation rate is the sum of the contribution of different dynamic processes:

$$R_1 = R_{1R} + R_{1SD} + R_{(1CF/OPF/ODF)} + R_{1RMTD}. \tag{6.1}$$

Except for the RMTD mechanism, which enters only in the nano-confined samples, the other relaxation mechanisms are present in the bulk as well as in the confined samples though their contribution could be slightly modified by the confinement.

## 6.4 Data analysis and discussion

### 6.4.1 Isotropic phase

The relaxation rate dispersions of the bulk PPA at 10 and 15$^o$C away from $T_{NI}$ are well described by a superposition of the two relevant relaxation mechanisms: molecular reorientations around short axes (R) and translational self-diffusion (SD). Here we obtained the values of the diffusion constant $D$

from other azoxybenzene compounds [16] and assigned the same to PPA to reduce the number of fit parameters. The coupling constant $A_D$ has not varied significantly over the temperature range in the isotropic phase, so its average value was used at all temperatures. The reorientational correlation time $\tau_R$ has increased with the decrease of temperature, while its strength $A_R$ has decreased. Close to the phase transition *i.e.*, at $\Delta T_{NI} = 0.6$, 2 and 6$^o$C, a better fit to the experimental data is obtained with an additional mechanism taking into account the orientational order critical fluctuations (CF) in addition to the R and SD. The correlation time $\tau_{CF}$ and the strength of the interaction $A_{CF}$ has increased on approaching the transition from above. The behavior of all these parameters with frequency and temperature are similar to the case of 8OCB (Chapter 5), and are commonly observed in bulk nematic liquid crystals. The fitted experimental data and the associated parameters at different temperatures are shown in Figures 6.8 - 6.12 and in Table 6.1.

Comparing the molecular parameters in the isotropic phase of bulk samples of 8OCB (Table 5.1) and PPA (Table 6.1), one observes that $\tau_R$ in 8OCB changes significantly from about 8 ns near the $T_{NI}$ to about 1 ns at 15$^o$C away into the isotropic phase. The corresponding change in PPA is more modest, from 3.5 ns to 1.7 ns, pointing out to relative differences in the activation energies. Both the samples do not exhibit discernible effects of order fluctuations beyond 6 - 7$^o$C from $T_{NI}$, and their critical dynamics is slow in 8OCB ($\tau_{CF} = 184$ ns near $T_{NI}$) relative to PPA ($\tau_{CF} = 75$ ns near respective $T_{NI}$). It must be stated that the experiments on PPA were restricted to 20 MHz on the high frequency side (unlike the case of 8OCB where data extend upto 50 MHz). This does put inherently less reliability on the absolute values of parameters derived from dispersion behavior at the high frequency end (like $A_R$ and $\tau_R$ values). The effect of such experimental limitation on estimations of slow dynamic phenomena is however marginal, and hence a comparison can be made with 8OCB data as far as confinement effects are concerned.

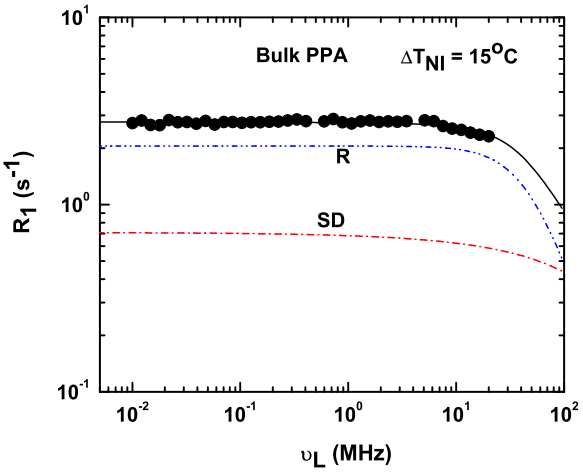


Figure 6.8: Frequency dependence of proton spin-lattice relaxation rate of bulk PPA at $\Delta T_{NI} = 15^{o}$C. The black line represents the calculated total relaxation rate and color lines are the corresponding relaxation rate contributions from different mechanisms.

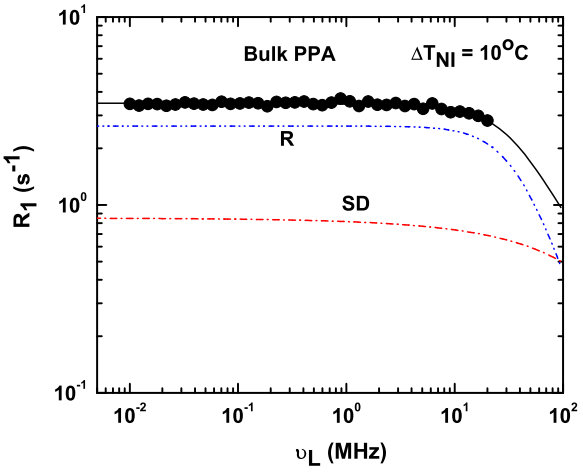


Figure 6.9: Frequency dependence of proton spin-lattice relaxation rate of bulk PPA at $\Delta T_{NI} = 10^{o}$C.

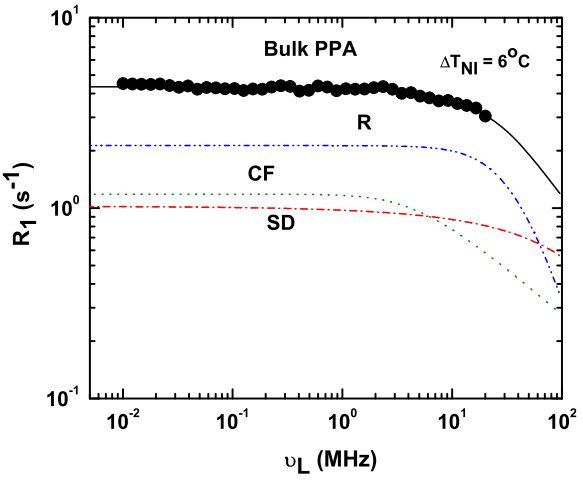


Figure 6.10: Frequency dependence of proton spin-lattice relaxation rate of bulk PPA at $\Delta T_{NI} = 6^o$C.

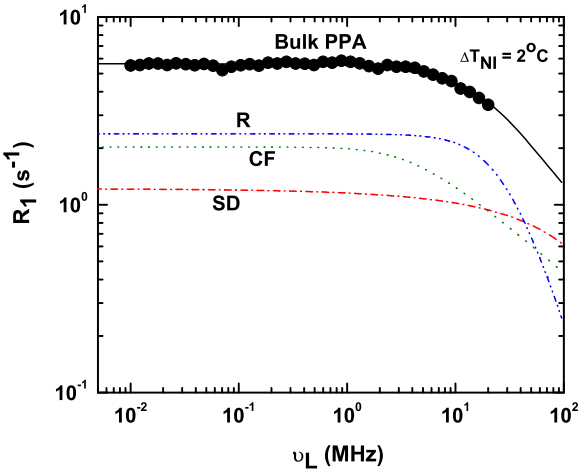


Figure 6.11: Frequency dependence of proton spin-lattice relaxation rate of bulk PPA at $\Delta T_{NI} = 2^o$C.

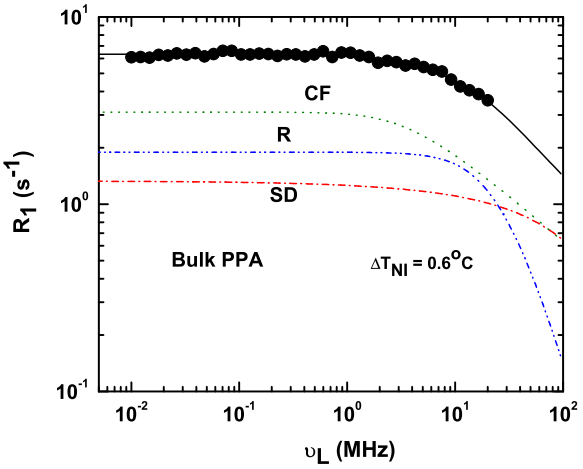


Figure 6.12: Frequency dependence of proton spin-lattice relaxation rate of bulk PPA at $\Delta T_{NI} = 0.6^{o}$C.

Table 6.1: Best fit values of parameters used in calculating the dispersion curves presented in Figures 6.8 - 6.12.

| Sample | Bulk PPA Isotropic | | | | |
|---|---|---|---|---|---|
| $\Delta T_{NI}$ ($^{o}$C) | 15 | 10 | 6 | 2 | 0.6 |
| $A_D$ $10^8$ s$^{-2}$ | 10 | 10 | 10 | 10 | 10 |
| D $10^{-11}$ m$^2$/s | 18 | 15 | 12.5 | 10.5 | 9.6 |
| $A_R$ $10^9$ s$^{-2}$ | 1.2 ± 0.02 | 1.22 ± 0.03 | 0.94 ± 0.04 | 0.8 ± 0.008 | 0.54 ± 0.02 |
| $\tau_R$ ns | 1.71 ± 0.006 | 2.16 ± 0.06 | 2.27 ± 0.14 | 3 ± 0.1 | 3.49 ± 0.23 |
| $A_{CF}$ $10^3$ s$^{-3/2}$ | – | – | 7 ± 0.08 | 11 ± 0.47 | 16 ± 0.75 |
| $\tau_{CF}$ ns | – | – | 57.21 ± 4.41 | 68.14 ± 1.82 | 75.26 ± 3.37 |

The relative relaxation rate increase in the confined samples is consistently explained by a sum of RMTD-induced relaxation rate and the bulk-like contributions of other mechanisms. The best fit contributions to the experimental data and the associated parameters are shown in Figures 6.13-6.17 and in Table 6.2 for Sample A and in Figures 6.18 - 6.22 and in Table 6.3, respectively. Clearly, RMTD is dominant below 1 MHz. It exhibits the characteristic power law frequency dependence between the two cutoff regimes, $R_{1RMTD} \propto \omega^{-p}$, here p = 0.34 $\pm$ 0.05. This value is of course is differing from the equipartition value of 0.5, and the discussion on this is presented in the earlier chapter in the context of 8OCB is appropriate and valid in this case also. More interesting is the fact that for the same dynamic confining environment obtained from identical (within the experimental errors) concentrations of the aerosil particles, the distribution of the diffusion modes (in the $q$-space) as reported by the liquid crystal systems is very much comparable. This provides further confirmation of the nature of the porous surface provided by this arrangement. Changes in the cutoff frequencies of the RMTD mechanism with decrease of temperature (Table 6.2 and Table 6.3) are associated with the decrease of the diffusion coefficient on cooling, and these are in turn connected with the largest and smallest molecular displacements that could cause significant loss in the molecular orientational correlation ($l_{max}$ and $l_{min}$). Of particular interest for purpose of comparison with 8OCB is the variation of $l_{min}$ value on cooling towards $T_{NI}$. One sees from Figure 6.23 that PPA reports rather a nominal change in $l_{min}$, steadily increasing from about 1.5 nm to 2 nm over 15$^o$C. In the case of 8OCB, for a similar variation of temperature above its $T_{NI}$ value, it is observed (Chapter 5, Figure 5.24) that $l_{min}$ is comparable ($\sim$ 1.5nm) at $\Delta T_{NI}$ = 15$^o$C, but increases to about 9 nm very close to $T_{NI}$. Further, its variation in 8OCB appears to approximate to a power law behavior, unlike the present system PPA (which is more like linear with the onset of CF mechanism at $\Delta T_{NI}$ = 6$^o$C). This contrasting variation of $l_{min}$, with a confining matrix having very similar structure factor (*i.e.*, very close $p$ values) brings about an interesting point for discussion. The variation of $D$ over this temperature region in 8OCB is from 19.1 to 11.9 ( $10^{-11}$ m$^2$/s), while in PPA it varies from 18 to 9.6 ( $10^{-11}$

$m^2/s$). Thus, change in $D$ value in both the liquid crystals are comparable, while change in fitted values of $\omega_{RMTDmax}$ differ significantly: from 65 MHz to 1 MHz in 8OCB (Table 5.3, Chapter 5) and from about 50 MHz to 17 MHz in PPA. The values of $l_{min}$ is related to these parameters via the relation $\omega_{RMTDmax} = Dq_{max}^2$. Thus, for a fixed geometry (structure factor) and comparable dynamics (diffusion coefficient and hence its associated modes under Gaussian approximation), such differences can come about if there is significant difference in the local ordering of the molecules at the respective surfaces. The larger value of $l_{min}$ near the transition, and its apparent pretransitional behavior in the case of 8OCB are indicative of the presence of significant ordering near the surface, in comparison with PPA. And this property in PPA is fairly insensitive to temperature. Taking due account of the fact that both the systems seen to need RMTD mechanism for interpretation of their data in the isotropic phase (thus confining observable adsorption effects in both the cases), we attribute this differential behavior with respect to $l_{min}$ to the difference in the orientations of the dipoles on the two molecules vis-a-vis the aligning direction preferred by the local structure due to anchoring interaction. The analysis also indicates that corresponding changes in $\omega_{RMTDmin}$ at both the concentrations in this system over similar temperature range are marginal and comparable. The strength of this interaction $A_{RMTD}$ shows an Arrehenius behavior with the temperature and the activation energy associated with this being about 35 kJ/mole for both the samples. This seems to provide another pointer to the difference in the surface interactions of the two liquid crystal systems. While this value of activation energy is comparable with Sample A of 8OCB, it is insensitive to the changes in the pore size, unlike 8OCB where further confinement increased the activation energy perceptibly (Chapter 5). As probably to be expected, the reorientational correlation time has decreased in the confined system indicating that the orientational order is extending into the cavities. However the relative changes in $\tau_R$ of this system is much smaller than the case with 8OCB (Tables 5.2 and 5.3, Chapter 5 and Tables 6.2 and 6.3, Chapter 6).

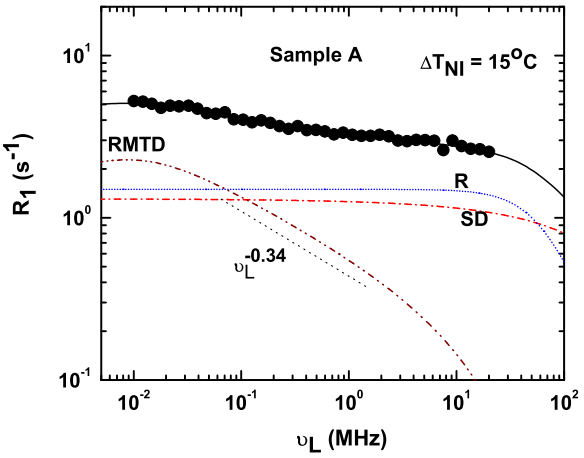


Figure 6.13: Frequency dependence of proton spin-lattice relaxation rate of Sample A at $\Delta T_{NI} = 15^o$C. The black line is the calculated total relaxation rate and color lines are the corresponding relaxation rate contributions from different mechanisms.

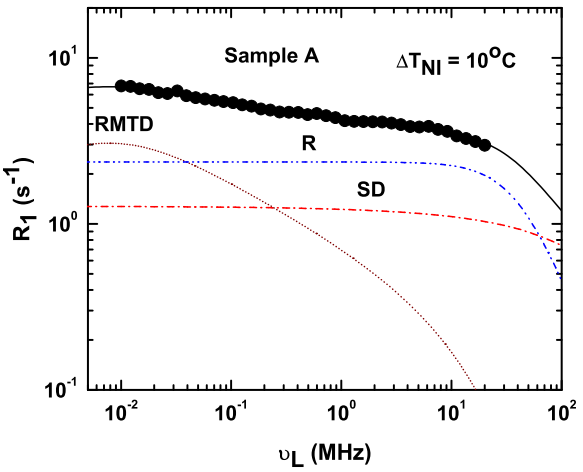


Figure 6.14: Frequency dependence of proton spin-lattice relaxation rate of Sample A at $\Delta T_{NI} = 10^o$C.

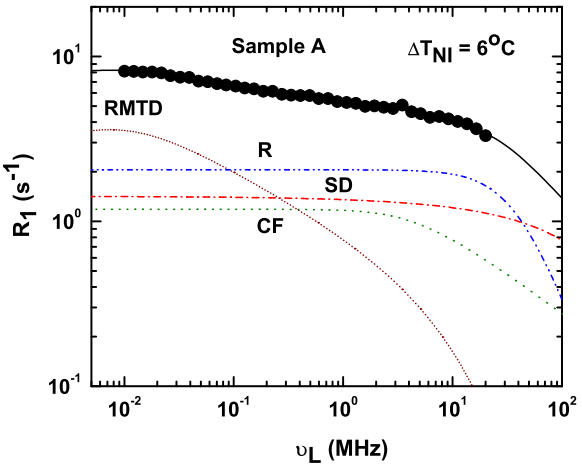


Figure 6.15: Frequency dependence of proton spin-lattice relaxation rate of Sample A at $\Delta T_{NI} = 6^o$C.

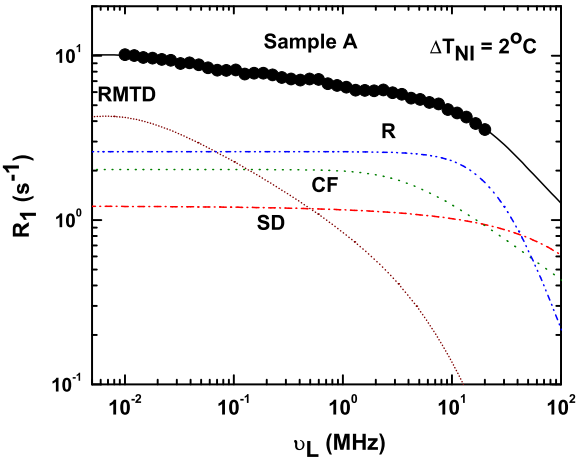


Figure 6.16: Frequency dependence of proton spin-lattice relaxation rate of Sample A at $\Delta T_{NI} = 2^o$C.

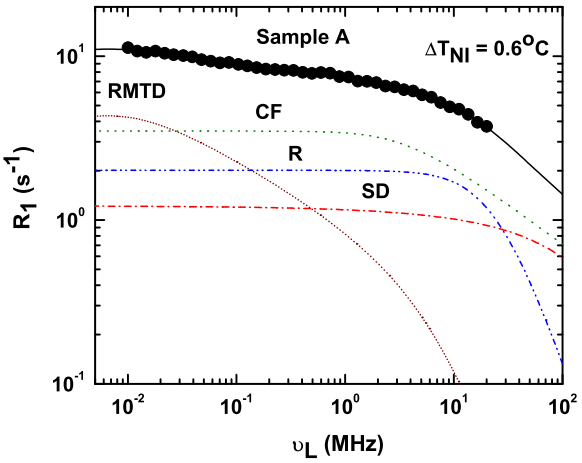


Figure 6.17: Frequency dependence of proton spin-lattice relaxation rate of Sample A at $\Delta T_{NI} = 0.6^{o}$C.

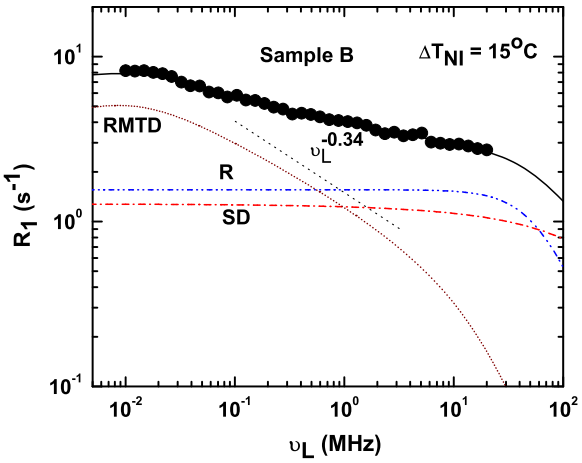


Figure 6.18: Frequency dependence of proton spin-lattice relaxation rate of Sample B at $\Delta T_{NI} = 15^{o}$C. The black line is the calculated total relaxation rate and color lines are the corresponding relaxation rate contributions from different mechanisms.

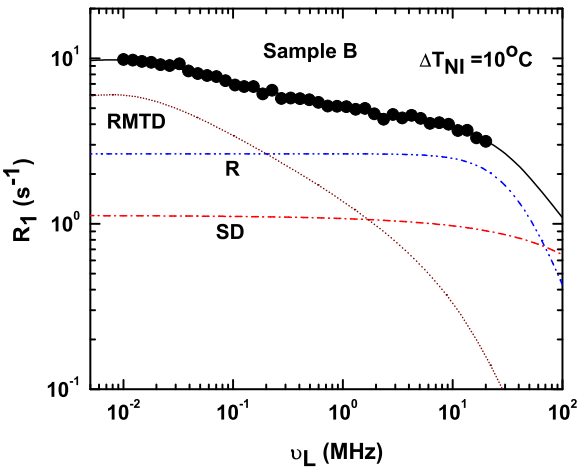


Figure 6.19: Frequency dependence of proton spin-lattice relaxation rate of Sample B at $\Delta T_{NI} = 10^{o}$C.

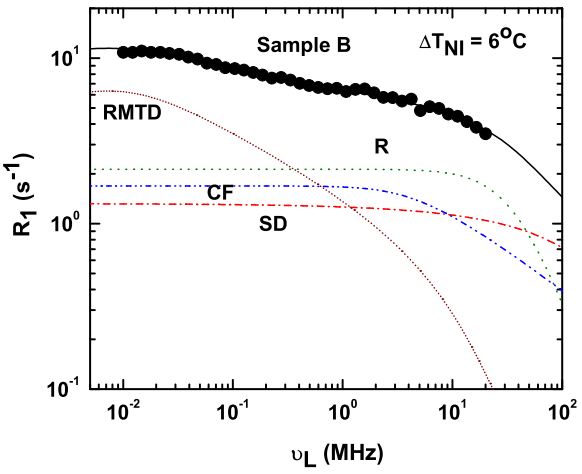


Figure 6.20: Frequency dependence of proton spin-lattice relaxation rate of Sample B at $\Delta T_{NI} = 6^{o}$C.

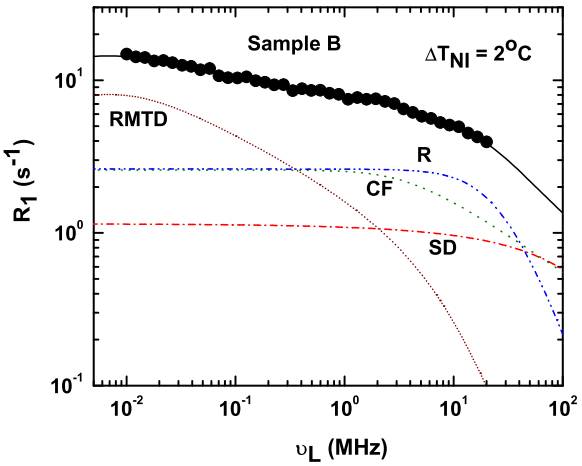


Figure 6.21: Frequency dependence of proton spin-lattice relaxation rate of Sample B at $\Delta T_{NI} = 2^o$C.

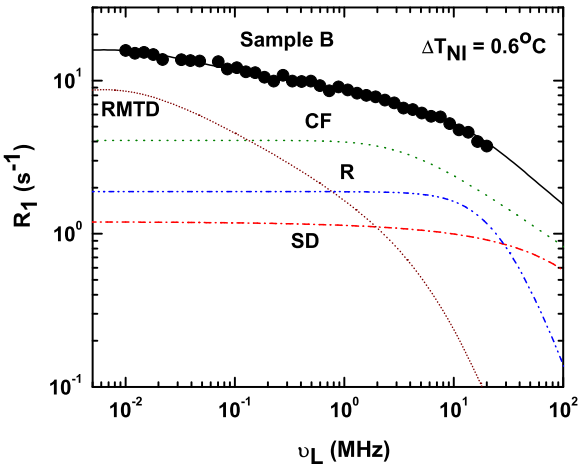


Figure 6.22: Frequency dependence of proton spin-lattice relaxation rate of Sample B at $\Delta T_{NI} = 0.6^o$C.

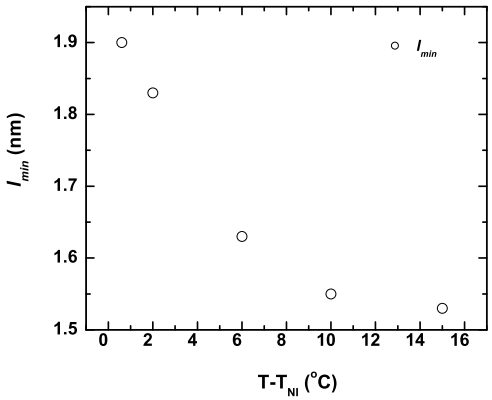


Figure 6.23: Variation of $l_{min}$ with temperature in the isotropic phase.

Table 6.2: Best fit values of parameters used in calculating the dispersion curves presented in Figures 6.13 - 6.17.

| Sample | Sample A Isotropic | | | | |
|---|---|---|---|---|---|
| $\Delta T_{NI}$ ($^o$C) | 15 | 10 | 6 | 2 | 0.6 |
| $A_D$ $10^8$ s$^{-2}$ | 18.5 ±3.8 | 15 ± 2.9 | 13.9± 1 | 10 ± 0.78 | 9.2 ± 0.3 |
| D $10^{-11}$ m$^2$/s | 18 | 15 | 12.5 | 10.5 | 9.6 |
| $A_R$ $10^9$ s$^{-2}$ | 1.2 | 1.22 | 0.94 | 0.8 | 0.54 |
| $\tau_R$ ns | 1.24 ± 0.22 | 1.97 ± 0.01 | 2.19 ± 0.11 | 3.26 ± 0.03 | 3.72 ± 0.09 |
| $A_{CF}$ $10^3$ s$^{-3/2}$ | – | – | 7 | 11 | 18 |
| $\tau_{CF}$ ns | – | – | 57.2 | 68.1 | 75.2 |
| $\omega_{RMTDmin}$ kHz | 20 ± 1.19 | 18.1 ± 1.37 | 16.91 ± 1.28 | 15.46 ± 1.46 | 15.24 ± 1.58 |
| $\omega_{RMTDmax}$ MHz | 49 ± 5.6 | 40 ± 4.8 | 30 ± 3.79 | 20 ± 3.1 | 17 ± 2.89 |
| $A_{RMTD}$ $10^2$ s$^{-(1+p)}$ | 0.32 ± 0.005 | 0.42 ± 0.006 | 0.49 ± 0.006 | 0.56 ± 0.01 | 0.57 ± 0.01 |
| $p$ | 0.34 | 0.34 | 0.34 | 0.34 | 0.34 |

Table 6.3: Best fit values of parameters used in calculating the dispersion curves presented in Figures 6.18 - 6.22.

| Sample | Sample B Isotropic | | | | |
|---|---|---|---|---|---|
| $\Delta T_{NI}$ ($^o$C) | 15 | 10 | 6 | 2 | 0.6 |
| $A_D$ $10^8$ s$^{-2}$ | 18 $\pm$2 | 13.2 $\pm$ 1.1 | 12.9$\pm$ 0.2 | 9.4 $\pm$ 0.5 | 9 $\pm$ 0.3 |
| D $10^{-11}$ m$^2$/s | 18 | 15 | 12.5 | 10.5 | 9.6 |
| $A_R$ $10^9$ s$^{-2}$ | 1.2 | 1.22 | 0.94 | 0.8 | 0.54 |
| $\tau_R$ ns | 1.29 $\pm$ 0.01 | 2.2 $\pm$ 0.09 | 2.27 $\pm$ 0.06 | 3.27 $\pm$ 0.1 | 3.49 $\pm$ 0.09 |
| A$_{CF}$ $10^3$ s$^{-3/2}$ | – | – | 7 | 11 | 18 |
| $\tau_{CF}$ ns | – | – | 57.2 | 68.1 | 75.2 |
| $\omega_{RMTDmin}$ kHz | 20 $\pm$ 1.19 | 18 $\pm$ 1.37 | 17 $\pm$ 1.28 | 16 $\pm$ 1.46 | 15.24 $\pm$ 1.58 |
| $\omega_{RMTDmax}$ MHz | 49 $\pm$ 5.6 | 40 $\pm$ 4.8 | 30 $\pm$ 3.79 | 20 $\pm$ 3.1 | 17 $\pm$ 2.89 |
| A$_{RMTD}$ $10^2$ s$^{-(1+p)}$ | 0.72 $\pm$ 0.01 | 0.83 $\pm$ 0.01 | 0.86 $\pm$ 0.01 | 1.07 $\pm$ 0.01 | 1.13 $\pm$ 0.01 |
| $p$ | 0.34 | 0.34 | 0.34 | 0.34 | 0.34 |

### 6.4.2 Nematic phase

Results of our measurements in nematic phase of PPA in bulk as well as in confined samples are presented in this section. Figures 6.24 - 6.27 show the dispersion profiles fitted to appropriate models (as discussed in Chapter 5) at various temperatures below $T_{NI}$ in the bulk sample (at $\Delta T_{NI}$ = -1, -3, -7 and -10$^o$C; $T_{NI}$ = 61.8$^o$C). The molecular parameters derived from the data are summarized in Table 6.4. The experimental data at corresponding temperatures in Sample A and Sample B of PPA are shown, along with their best fit curves, in Figures 6.28 - 6.35, while Tables 6.5 and 6.6 indicate the outcome of fitting these data to the models, as indicated earlier.

We first focus on the nematic phase very near the transition temperature ($\Delta T_{NI}$ = -1$^o$C). At this temperature order parameter fluctuations provide a dominant mechanism for relaxation, and in the bulk sample it is the only slow process effecting the dispersion (Figure 6.24). The characteristic time associated with these fluctuations $\tau_{OPF}$ is about 134 ns. Comparing this with the corresponding value in bulk 8OCB sample (422 ns), it appears that time scales of critical fluctuations in PPA are uniformly shorter than in 8OCB. In both the liquid crystals $\tau_R$ remains essentially the same across the transition within the estimated errors.

Next we examine the effect of confinement on PPA, relative to the bulk sample at $\Delta T_{NI}$ = -1$^o$C. There is practically no change in $\tau_R$ due to confinement in PPA (Tables 6.4 - 6.6) and $\tau_R$ remains at about 3 ns. The effect of confinement on $\tau_R$ in 8OCB is however significant: it changes from 8.15 ns in bulk sample to 6 ns in Sample A and to 5.4 ns in Sample B. This observation can be interestingly correlated to the exponent $p$ in the power law governing the frequency dependence between the corresponding $\omega_{RMTDmin}$ and $\omega_{RMTDmax}$. The exponent remains the same (at 0.34) as in the isotropic phase for PPA, while it shows slight increase in confined 8OCB on the onset of nematic phase (0.39 in the isotropic phase to 0.45) just below the transition.

Common to 8OCB and PPA is the observation that progressive confinement (Sample A and Sample B) leads in both the systems an increased coupling to the lattice *via* RMTD mechanism (*i.e.*, changes in the$A_{RMTD}$ in these samples).

We now discuss the results of our analysis at three temperatures deep in the nematic phase ($\Delta T_{NI}$ = -3, -7 and - 10$^o$C). In the bulk sample (Table 6.4), $\tau_R$ decreases progressively on cooling due to the gradual increase in the orientational order in the sample. Within the frequency range of the experiment, no leveling of the relaxation rate at low frequency end could be observed, indicating that $\omega_{ODFmin}$ should be significantly below the lowest frequency studied. $A_{ODF}$ represents the coupling of the spin system to the lattice *via* ODF marginally increases initially on cooling and saturates at $\Delta T_{NI}$ = -10$^o$C (Table 6.4). In the bulk sample of 8OCB, $A_{ODF}$ steadily and significantly increases over a similar temperature range (Table 5.4).

Effect of confinement on PPA sample at different temperatures in the nematic phase are presented in the Tables 6.5 and 6.6, and we take a specific case of $\Delta T_{NI}$ = -7$^o$C for discussion, because of convenience for comparison with the nematic phase results of 8OCB in its mid-nematic range (8OCB has an underlying smectic phase). Based on the discussion regarding fit-1 (interms of $R_{1X}$) and fit-2 (in terms of $R_{1ODF} + R_{1RMTD}$) presented in Chapter 5, we restrict our analysis of PPA sample to fit-2. Thus, referring to Tables 6.4 (bulk), 6.5 (Sample A) and 6.6 (Sample B), at $\Delta T_{NI}$ = -7$^o$C, we see one immediately discernible effect of confinement is the significant increase of $\omega_{ODFmin}$ to the range of MHz (much like the case of 8OCB). Thus the confinement with aerosil 3-d network is placing a severe restriction on the long wavelength ODF modes, pushing the value of the corresponding cutoff frequency by an order of magnitude. This circumstance leaves room for other slow mechanisms, like RMTD, to play their visible role at much lower frequencies. An interesting consequence of confinement on PPA system is that the exponent $p$ changes from 0.34 (within the vicinity of the transition

$\Delta T_{NI}$ = -1$^o$C) to 0.63. This of course is an indication of the qualitative changes in the effective structure factor probed by the diffusing molecules. This corresponds to a change to a regime, on cooling, where long wavelength diffusive modes are more probable. A similar change was observed in the case of 8OCB also on confinement ($p$ = 0.58). Finally, the progressive onset of orientational order on cooling deep into the nematic phase has profound effect in the confined samples. The effect for example on $\omega_{ODFmin}$ and $A_{RMTD}$ is seen in both the Samples (A and B), correspondingly more in Sample B. The exponent $p$ is marginally sensitive, if at all, to the degree of confinement (0.63 in Sample A and 0.66 in Sample B).

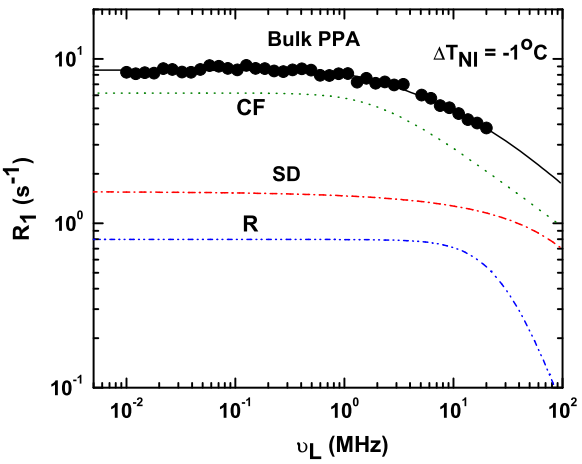


Figure 6.24: Frequency dependence of proton spin-lattice relaxation rate of bulk PPA at $\Delta T_{NI} = -1^o$C. The black line represents the calculated total relaxation rate and color lines are the corresponding relaxation rate contributions from different mechanisms.

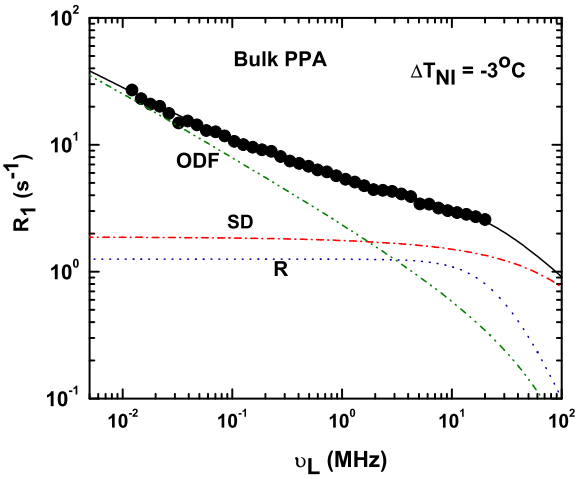


Figure 6.25: Frequency dependence of proton spin-lattice relaxation rate of bulk PPA at $\Delta T_{NI} = -3^{o}$C.

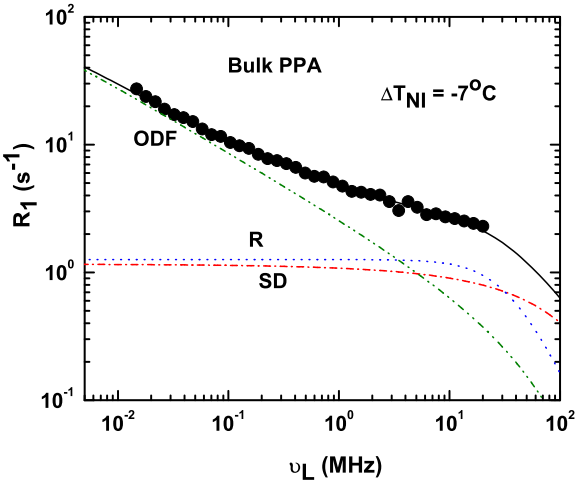


Figure 6.26: Frequency dependence of proton spin-lattice relaxation rate of bulk PPA at $\Delta T_{NI} = -7^{o}$C.

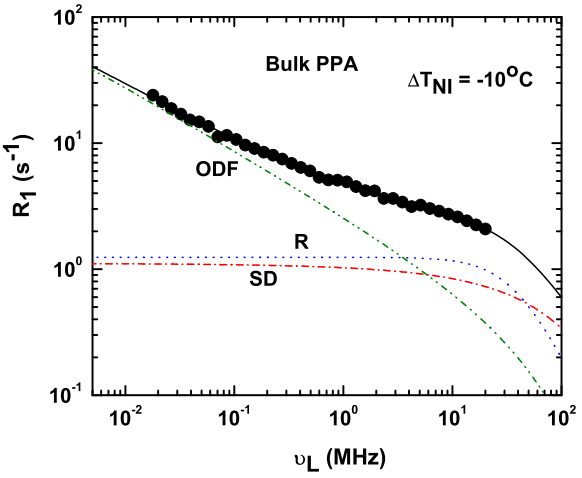


Figure 6.27: Frequency dependence of proton spin-lattice relaxation rate of bulk PPA at $\Delta T_{NI} = -10^{o}$C.

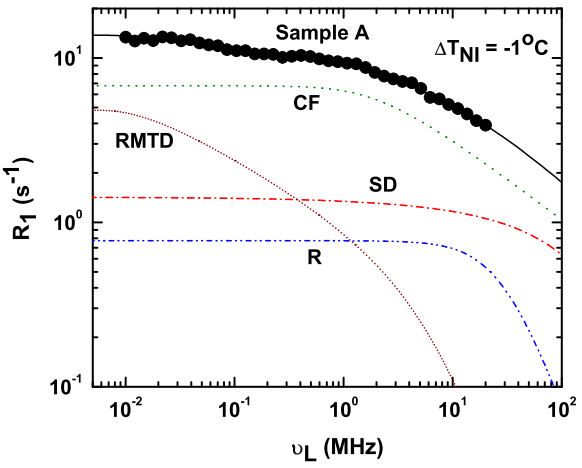


Figure 6.28: Frequency dependence of proton spin-lattice relaxation rate of Sample A at $\Delta T_{NI} = -1^{o}$C. The black line represents the calculated total relaxation rate and color lines are the corresponding relaxation rate contributions from different mechanisms.

Table 6.4: Best fit values of parameters used in calculating the dispersion curves presented in Figures 6.24 - 6.27.

| Sample | Bulk PPA Nematic | | | |
|---|---|---|---|---|
| $\Delta T_{NI}$ ($^o$C) | -1 | -3 | -7 | -10 |
| $A_D$ $10^8$ $s^2$ | 10 | 10 | 5 | 4 |
| D $10^{-11}$ $m^2/s$ | 8.2 | 6.8 | 5.5 | 4.6 |
| $A_R$ $10^9$ $s^2$ | 0.26 ± 0.07 | 0.38 ± 0.01 | 0.5 ± 0.04 | 0.56 ± 0.03 |
| $\tau_R$ ns | 3.03 ± 0.59 | 3.23 ± 0.16 | 2.52 ± 0.04 | 2.23 ± 0.16 |
| $A_{OPF}$ $10^3$ $s^{-3/2}$ | 23.94 ± 2.11 | – | – | – |
| $\tau_{OPF}$ ns | 134.11 ± 11.22 | – | – | – |
| $A_{ODF}$ $10^3$ $s^{-3/2}$ | – | 6.49 ± 0.04 | 6.98 ± 0.03 | 6.98 ± 0.04 |
| $\omega_{ODFmin}/2\pi$ kHZ | – | 1 | 1 | 1 |
| $\omega_{ODFmax}/2\pi$ MHz | – | 100 | 100 | 100 |

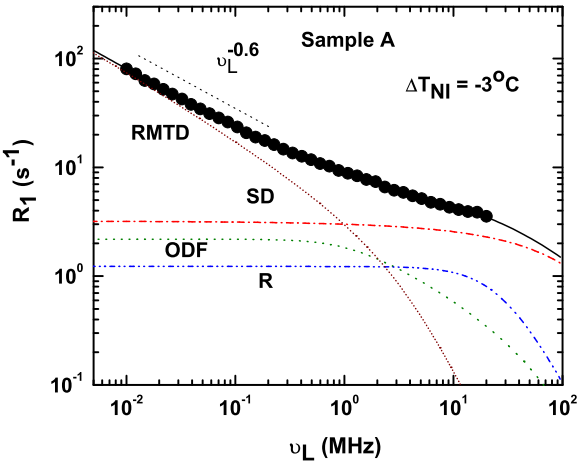


Figure 6.29: Frequency dependence of proton spin-lattice relaxation rate of Sample A at $\Delta T_{NI} = -3^o$C.

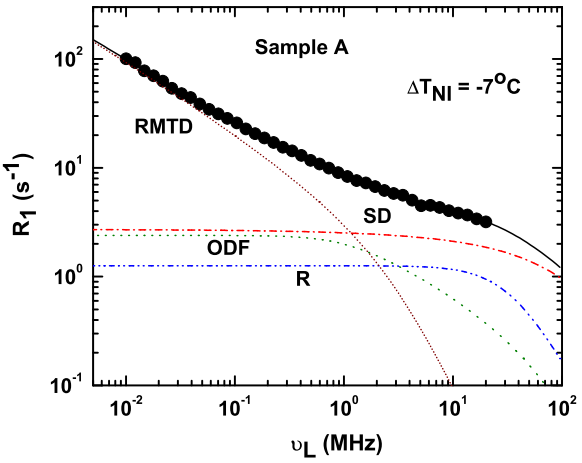


Figure 6.30: Frequency dependence of proton spin-lattice relaxation rate of Sample A at $\Delta T_{NI} = -7^o$C.

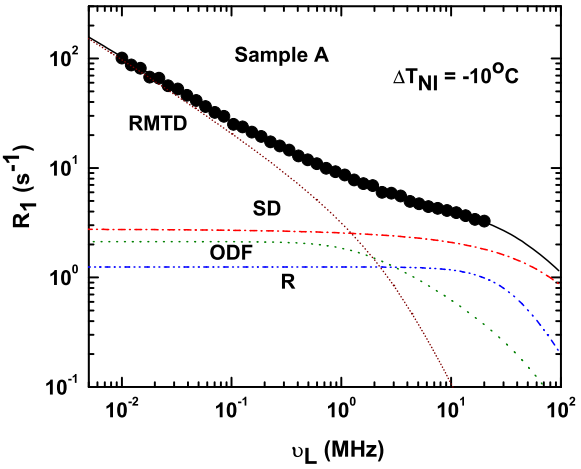


Figure 6.31: Frequency dependence of proton spin-lattice relaxation rate of Sample A at $\Delta T_{NI} = -10^{o}$C.

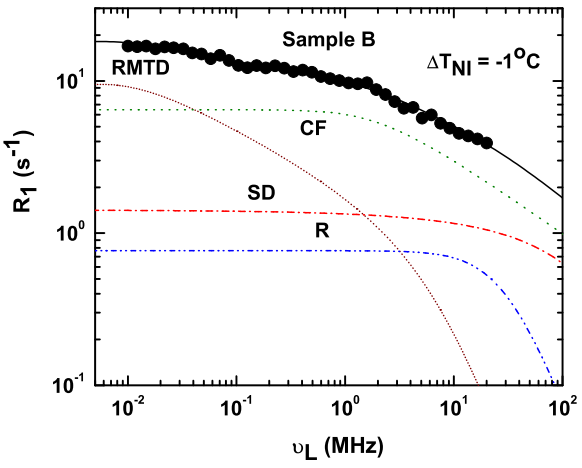


Figure 6.32: Frequency dependence of proton spin-lattice relaxation rate of Sample B at $\Delta T_{NI} = -1^{o}$C. The black line represents the calculated total relaxation rate and color lines are the corresponding relaxation rate contributions from different mechanisms.

Table 6.5: Best fit values of parameters used in calculating the dispersion curves presented in Figures 6.28 - 6.31.

| Sample | Sample A Nematic | | | |
|---|---|---|---|---|
| $\Delta T_{NI}$ ($^o$C) | -1 | -3 | -7 | -10 |
| $A_D$ $10^8$ $s^2$ | 9.1 ± 0.4 | 17.1 ± 0.1 | 11.7 ± 0.08 | 9.9 ± 0.1 |
| D $10^{-11}$ $m^2/s$ | 8.2 | 6.8 | 5.5 | 4.6 |
| $A_R$ $10^9$ $s^2$ | 0.26 | 0.38 | 0.5 | 0.56 |
| $\tau_R$ ns | 2.98 ± 0.47 | 3.23 | 2.52 | 2.23 |
| $A_{OPF}$ $10^3$ $s^{-3/2}$ | 26.17 ± 0.59 | – | – | – |
| $\tau_{OPF}$ ns | 134.1 | – | – | – |
| $A_{ODF}$ $10^3$ $s^{-3/2}$ | – | 6.49 | 6.98 | 6.98 |
| $\omega_{ODFmin}/2\pi$ kHZ | – | 913.68 ± 200.24 | 900 ± 183.21 | 1114 ± 116.85 |
| $\omega_{ODFmax}/2\pi$ MHz | – | 100 | 100 | 100 |
| $\omega_{RMTDmin}/2\pi$ kHZ | 13 ± 1.09 | 1 | 1 | 1 |
| $\omega_{RMTDmax}/2\pi$ MHZ | 15 | 8.43 ± 0.69 | 6.35 ± 0.46 | 6.82 ± 0.31 |
| $A_{RMTD}$ $10^2$ $s^{-(1+p)}$ | 0.6 ± 0.01 | 159.12 ± 21.77 | 284.61 ± 21.11 | 300.99 ± 1.77 |
| $p$ | 0.34 ± 0.05 | 0.6 ± 0.01 | 0.63 ± 0.006 | 0.63 ±0.01 |

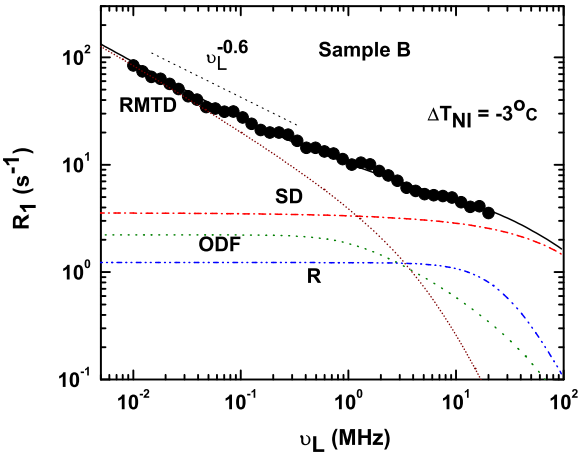


Figure 6.33: Frequency dependence of proton spin-lattice relaxation rate of Sample B at $\Delta T_{NI} = -3^o$C.

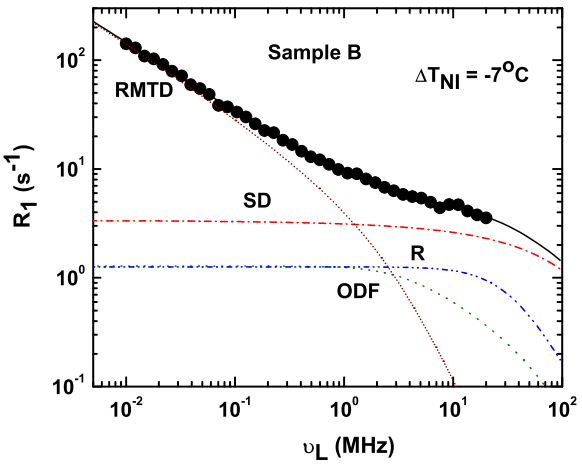


Figure 6.34: Frequency dependence of proton spin-lattice relaxation rate of Sample B at $\Delta T_{NI} = -7^o$C.

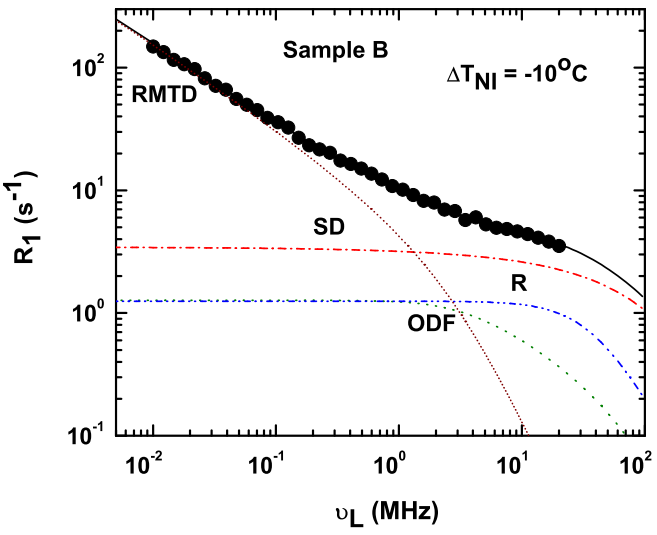


Figure 6.35: Frequency dependence of proton spin-lattice relaxation rate of Sample B at $\Delta T_{NI} = -10^{o}$C.

Table 6.6: Best fit values of parameters used in calculating the dispersion curves presented in Figures 6.32 - 6.35.

| Sample | Sample B Nematic | | | |
|---|---|---|---|---|
| $\Delta T_{NI}$ ($^o$C) | -1 | -3 | -7 | -10 |
| $A_D$ $10^8$ $s^2$ | 9.1 ± 0.4 | 19 ± 0.1 | 14.5 ± 0.02 | 12.4 ± 0.1 |
| D $10^{-11}$ $m^2/s$ | 8.2 | 6.8 | 5.5 | 4.6 |
| $A_R$ $10^9$ $s^2$ | 0.26 | 0.38 | 0.5 | 0.56 |
| $\tau_R$ ns | 2.95 | 3.23 | 2.52 | 2.23 |
| $A_{OPF}$ $10^3$ $s^{-3/2}$ | 24.98 ± 0.17 | – | – | – |
| $\tau_{OPF}$ ns | 134.1 | – | – | – |
| $A_{ODF}$ $10^3$ $s^{-3/2}$ | – | 6.49 | 6.98 | 6.98 |
| $\omega_{ODFmin}/2\pi$ kHZ | – | 900 ± 203.5 | 2676.13 ± 314.6 | 2714 ± 224.12 |
| $\omega_{ODFmax}/2\pi$ MHz | – | 100 | 100 | 100 |
| $\omega_{RMTDmin}/2\pi$ kHZ | 13 ± 1.09 | 1 | 1 | 1 |
| $\omega_{RMTDmax}/2\pi$ MHZ | 15 | 13± 1.2 | 6 ± 0.6 | 6.5 ± 0.51 |
| $A_{RMTD}$ $10^2$ $s^{-(1+p)}$ | 1.18 ± 0.02 | 160.99 ± 0.89 | 548.04 ± 3.72 | 669.82 ± 3.99 |
| $p$ | 0.34 ± 0.05 | 0.59 ± 0.01 | 0.65 ± 0.01 | 0.66 ±0.02 |

## 6.5 Conclusions

We present results of analysis of the dispersions of spin-lattice relaxation rates at various temperatures covering the isotropic and nematic phases of liquid crystal PPA. We compare the results obtained for bulk sample with two confined systems with different average pore sizes. The discussion focuses on a comparison of PPA bulk data with its confined counterparts, as well as a comparison of dynamical organization in PPA and 8OCB under very comparable confinement effects. In the isotropic phase PPA exhibits pretransitional effects on the relaxation profiles within a range of about 6 - 7$^o$C above $T_{NI}$, much like 8OCB. The time scales of the nematic clusters $\tau_{CF}$ however differ by a factor of 2; 8OCB bulk medium supports relatively long lived clusters at comparable temperature deviations from the respective $T_{NI}$. Surface interactions with a liquid crystal medium as a result of confinement introduce RMTD mechanism which provides an insight into the surface topology (in terms of its structure factor) and adsorption kinetics ($\omega_{RMTD}$ cutoff values). We find that the exponent $p$ obtained from confined PPA samples is lower than the equipartition value (0.5), and is essentially the same as reported by 8OCB. The observed value (0.34 - 0.38) is indicative of relative abundance of low wavelength modes and truly reflects the nature of the surface formed by the 3-d network of chosen aerosil particles. The qualitative difference in the temperature variation of $l_{min}$ in the isotropic phase of PPA and 8OCB are discussed, recognizing the fact that $l_{min}$ represents the smallest relevant length scale (at the surface) to induce observable decoherence of the orientational correlations. It is argued that this difference is likely to be related to the difference in the direction of the dipoles located in the two molecules (relative to the respective long axis). The effect of increasing orientational order on cooling the nematic PPA, and confinement related effects at each of the temperature in this phase are qualitatively similar to those observed in 8OCB, except for minor variations in magnitudes of certain parameters. There are however two differences. The value of $\tau_R$ in the bulk PPA varies from about 3 ns to 2.2 ns on cooling into the nematic phase by 10$^o$C, while

its value in bulk 8OCB changes from 8 ns to 0.5 ns over a comparable temperature range. This difference seems to be correlated with the presence of a layered phase (Smectic-A) in the case of 8OCB. Secondly, the value of the exponent $p$ slightly differs in two cases, being 0.65 in mod-nematic region of PPA and 0.55 in 8OCB. This positive deviation from the equipartition value indicates favorable conditions for long wavelength diffusive modes (at the surface) in the nematic phase of both the systems, more so in the case of PPA.

# References

[1] G. P. Crawford and S. Zumer, *Liquid crystals in complex geometries*, Taylor and Francis, London (1996).

[2] G. A. Puchkovskaya, Yu.A. Reznikov, A.A. Yakubov, O.V. Yaroshchuk, A.V. Glushchenko, J. Mol. Struc. **381**, 133 (1996).

[3] T. Bellini, L. Radzihovsky, J. Toner, and N. A. Clark, Science **294**, 1074 (2001).

[4] T. Jin, D. Finotello, Phys. Rev. E **69**, 041704 (2004).

[5] A. Roshi, G. S. Iannacchione, P. S. Clegg, R. J. Birgeneau, Phys. Rev. E **69**, 031703 (2004).

[6] M. Caggioni, A. Roshi, S. Barjami, F. Mantegazza, G. S. Iannacchione, and T. Bellini, Phy. Rev. Lett. **93**, 127801 (2004).

[7] A. Roshi, S. Barjami, G. S. Iannacchione, D. Paterson, I. Mcnulty, Phys. Rev. E **74**, 031404 (2006).

[8] E. Anoardo, F. Grinberg, M. Vilfan, and R. Kimmich, Chem. Phys. **297**, 99 (2004).

[9] M. Rajeswari, S. Dhara, K. Venu, V. S. S. Sastry, R. Dabrowski (to appear in Mol. Cryst. Liq. Cryst, 2011).

[10] G. S. Iannacchione, Fluid Phase Equilibria. **222-223**, 177 (2004).

[11] R. Y. Dong, *Nuclear Magnetic Resonance of Liquid Crystals*, Springer-Verlag (1997).

[12] A. Abragam, *The Principles of Nuclear Magnetism*, Clarendon Press, Oxford (1961).

[13] Rainer Kimmich and Hans Werner Weber, Phys. Rev. B **47**, 11788 (1993).

[14] R.Kimmich, E. Anoardo, Prog. Nucl. Magn. Reson. Spectrosc. **44**, 257 (2004).

[15] M. Vilfan,T. Apih, P. J. Sebastiao,G. Lahajnar, and S. Zumer, Phys. Rev. E **76**, 051708 (2007).

[16] Mario Cifelli, Giorgio Cinacchi, and Luca De Gaetani, J. Chem. Phys. **125**, 164912 (2006).

# 7

# Conclusions

The work presented in this thesis is directed towards the application of a very interesting variation of wide-line NMR spectroscopy, *viz.* measurement of spin-relaxation rates of chosen nuclei in a soft material over a wide frequency range ($10^4$ to $\sim 10^8$ Hz). By virtue of the coupling of the participating nuclei to the lattice modes only under resonant conditions, this methodology focuses specifically on lattice modes in a given frequency region consistent with the resonance frequency. Thus such dispersion experiments exploit this potential to, essentially, map the spectral power of molecular level time fluctuations via the measurable relaxation rates. Such relaxation profiles, collected as a function of other complementary external control parameters, like temperature, will on one hand provide a convenient handle to track certain of the dynamic processes accessed by the microscopic probe in the system. On the other hand, availability of such data also is needed to provide a check on the consistency of the underlying molecular dynamic models proposed for interpretation.

The use of such methods is evident more recently with the advent of field-cycling methods which circumvent the instrument-related difficulties in accessing the relaxation processes at very low operating frequencies. The convenience lies in preparing and detecting the spin polarizations at comfortably high enough fields, while allowing the spin system to sample the lattice modes,

and relax, at the desired low frequencies by making a rapid enough transit to such fields during the process of spin relaxation. This experimental work is carried out on such an instrument, supplemented with a home-built high-end variable frequency pulsed NMR spectrometer. Thus a dynamic range of $10^4$ to $0.5\times10^8$ Hz could be achieved. Liquid crystals are chosen for such dispersion experiments which are suited to cover very large time scale phenomena, for many reasons, including: they have many intermediate thermodynamically stable phases with differing orientational and positional ordering leading to rich (collective) dynamic molecular organizations spanning to larger time scales of correlations; discernible pretransitional effects near respective phase transitions due to critical slowing down of order fluctuations; liquid crystals are soft materials very easily susceptible to external perturbations including surface interactions and consequent preferential anchoring; and finally surface induced diffusion in the presence of possible adsorption results in slow reorientational correlations.

The first problem discussed in the thesis is concerned with a contrasting study on the dynamics of the same molecules in a liquid crystal system, but as probed by two different species of nuclei (both are spin-1/2 for convenience and have very comparable gyromagnetic ratios, $^1H$ and $^{19}F$). We have chosen two members of the tolane family (4OFTOL and 4OTOLFo), for which one proton on the aromatic ring is replaced by fluorine (singly fluorinated tolane). Usually the spin-lattice relaxation of such spin-1/2 nuclei in the wide-line NMR regime, particularly at low frequencies, are primarily mediated by reorientational dynamics modulating the inter- or intra-nuclear dipolar interactions. In the case of protons with a relatively very low spin-rotation coupling, dipolar interaction is the primary mechanism for explaining the relaxation data in liquid crystals, as is well established. Introduction of lone fluorine differs qualitatively in this respect: it can in principle relax *via* hetero-nuclear coupling with protons in the same molecule, or homo-nuclear coupling with fluorines on the other molecules, anisotropic interactions arising from chemical shift (which is field dependent), and finally

through spin-rotation coupling with the molecular angular momentum components. Under the conditions of the present experiments, it is argued that the last mechanism is the dominant one for fluorine and thus differs in its sensitivity to the molecular processes, being influenced by time correlations of molecular angular fluctuations rather than of molecular reorientations.

The experiments on these two systems provided a very interesting contrast. To start with, the results on proton are conforming to the established models and are interpreted accordingly. The slowest components detected by protons, say in the isotropic phase, are due to pre-transitional critical fluctuations and in the range of 363 ns in 4OFTOL, and 49.5 ns in 4OTOLFo very near the transition ($\Delta T_{NI} = 0.5^o$C in the case of 4OFTOL and $1^o$C in the case of 4OTOLFo). These collective fluctuations are seen to persist into the isotropic phase over a range of about $\Delta T_{NI} = 11^o$C in 4OFTOL and $4^o$C. The difference in the pretransitional behavior of the two systems, as reported by these studies, seem to be correlated to the location of the fluorine on the molecule, as has been also observed by earlier dielectric measurements. Coming to the fluorine experiments, it is immediately seen that there has been a very significant difference in the dispersion of the relaxation rates in the sub-MHz regime, differing by at least an order of magnitude. Keeping in view that the fluorine could not have an effective dipolar coupling under the circumstances of the experiment, and also its relatively higher spin-rotation coupling, the relaxation is attributed to the strong fluctuations at the appropriate frequencies in the local fields at the site of the fluorine nuclei arising from the molecular rotations, quantified by the angular momentum time fluctuations. It is observed that the slow critical dynamic processes reported by the protons are not adequate to account for the enhanced relaxation rate in the lower frequency region ($< 10^6$ Hz), and required invoking additional slow modes which are accessed selectively by the angular momentum components. In this context, earlier ESR studies on liquid crystals are found helpful in attempting a resolution of the problem. The detailed ESR line width measurements, as well as subsequent 2-d ESR experiments, indicated

the presence of slowly relaxing local structures (SRLS), referred to as cages, which summarize the effect of all the slow processes due to local structures on the individual molecular rotational dynamic process. It is known from the ESR studies on different probes that the coupling of the probing molecule to these modes is stronger, the bigger the molecule is (relative to the surrounding liquid crystal molecules). In the present case the probing molecule is that of the liquid crystal itself, and hence the sensitivity of this interaction to the slow modes is expected to be the maximum. The interpretation of the data on the two systems yielded reasonable estimates of time scales of such modes, and provide a very interesting contrast with respect to the conclusions from the proton data. A preliminary account of such a study on another related system was reported from this laboratory recently. This is probably for the first time that the SRLS mechanism is being directly accessed by the FCNMR technique with this specific choice of samples.

Another curious phenomenon, of specific interest to the NMR spectroscopy, is the regime of low applied fields when the proton and fluorine resonance lines start overlapping despite their differences in the gyromagnetic ratios, commonly referred to as the strong coupling limit (in terms of the corresponding spin Hamiltonian). In this regime, the flip-flop terms in the hetero-nuclear dipolar interaction terms assist in transferring some of the fluorine magnetization to the proton reservoir via the so-called *like* spin coupling, and are seen as irreversible losses to the lattice as far as fluorine spin-lattice relaxation is concerned, particularly when the detection is made at high enough frequencies when the two species are again *unlike*. We invoked this cross-relaxation mechanism to explain the anomalous increase in the fluorine relaxation rates at the very low frequency end. The fitting of this contribution *via* overlap integrals of the lines yielded reasonable estimates of the resonance line widths of the two nuclei, as a function of temperature in the isotropic phase.

The second part of the work deals with the effect on the spin relaxation of

surface induced slow reorientational dynamics arising from adsorption. Confinement of soft systems like liquid crystals in small enough (nano meter size) pores makes this effect discernible in an experiment. For example even in an isotropic phase of the system, surface diffusion within an adsorption layer under strong polar interactions could lead to appreciable long-time tails in the reorientational correlations, leading the RMTD process. Such contributions are of course governed by, apart from the diffusion coefficients, the roughness of the surface characterized by its wave vector dependent structure factor with cutoff values dependent on the surface topology. Backed up by details of molecular dynamics obtained from similar studies in bulk samples, and under the assumption that at least some of these are not affected by confinement, experiments on confined systems can thus be used to extract information on the nature of the surface of the pores and possibly its effect on the individual molecular dynamic processes.

With this objective, we report results of experiments on two liquid crystal systems under identical confinement conditions, obtained by introducing suitably treated aerosil particles at chosen concentrations, so as to provide a random 3-d network with an average pore size ranging between 90 - 133 nm. The individual aerosil particles have an average diameter of 7 nm. Thus the porous medium presents a very corrugated topological 2-d surface, with the size of the individual nano size particles playing a role in defining the structure factor. The liquid crystals are chosen such that one has an electric dipole approximately along the long axis of the molecule (8OCB) and the other perpendicular to it (PPA). For comparison purposes detailed relaxation dispersion measurements were initially carried out in the isotropic as well as the other mesophases of the respective systems in bulk samples, and the underlying molecular processes are characterized. The relaxation rates in confined systems show perceptible enhancement in the low frequency region due to surface effects, compared to the respective bulk results. Analysis of this data provided information on the coupling of the spin system to the RMTD process, which is a measure of the induction of slow processes due

to adsorption. It also yielded estimates of lower and upper cutoff RMTD frequencies, reflecting the upper and lower bounds on the displacements near surfaces to produce significant decoherence of the orientations of the molecules. Differences in these values, observed for example in the isotropic phase, seem to be correlated with the placement of the dipole on the molecule. The frequency dispersion of the relaxation rate within these cutoff frequencies is expected to follow a power law and the associated exponent is connected with the wave-vector dependence of the structure factor. Assumption of equitable distribution of these modes over the wave-vector range of interest yields a value of 0.5, and deviations toward low or high values are indicative of the predominance of low or high wavelength diffusive modes, respectively. Both the liquid crystal molecules report identical characteristics of the surface in the isotropic phase (an exponent in the range of 0.34 to 0.38) indicating deviation from the equipartition of modes favoring low wavelength diffusive excursions, perhaps consistent with the type of the porous confinement of this specific confinement provides. The higher values observed for this exponent in the nematic (for 8OCB and PPA) and smectic (for 8OCB) phases (ranging from 0.55 to 0.66) are indicative of the presence of long wavelength diffusive modes due to the surface ordering in the medium.

This discussion on the interpretation of RMTD effects is incumbent on the fact that this contribution can be and uniquely separated with reasonable reliability from the others (in particular in the mesophases, which include for example the dominant order director fluctuations in the bulk medium as well), while analyzing the experimental data. This work attempts to do this exercise by making use of the information on the ODF modes obtained from experiments on the bulk, backed up by appropriate curve fitting procedures. It should thus be emphasized that these two mechanisms have certain common regions in the low frequency regime of the experiment where their time scales do compete, and hence the RMTD characterization in such cases is to be interpreted keeping this limitation in mind. Taking the data from the respective mesophases of the two systems together into consideration, the res-

ults do indicate perceptible effect of surface adsorption on the wave-vector dependence of the structure factor. And these conclusions qualitatively differ from the analysis of respective isotropic phase data, indicating subtle changes in the adsorption layers due to the onset of orientational order in the medium.

The thesis thus makes a modest attempt to study two different types of slow phenomena as probed by NMR relaxation mechanisms, making use of a recently developed experimental methodology extending significantly the dynamic range of the study. The interpretation of the data, based on some very interesting contemporary stochastic models, yielded hopefully new results. In particular, use of multi-nuclear spin-lattice relaxation dispersion studies on liquid crystals, tailored to have qualitatively differing relaxation mechanisms, seems to have a promising potential to investigate different dynamic aspects of the same molecule.